This is to certify that the
dissertation entitled

NEW METHOD FOR DETECTING DOMAIN WALL TRAPPING AND MOTION AT A CONSTRICTION IN NARROW FERROMAGNETIC WIRES USING PERPENDICULAR-CURRENT GIANT MAGNETORESISTANCE

presented by

Antonio Javier Zambano

has been accepted towards fulfillment
of the requirements for the

Ph.D. degree in Physics

William P. Pratt

Major Professor's Signature

July 14, 2004

Date

NEW METHOD FOR DETECTING DOMAIN WALL TRAPPING AND MOTION AT A CONSTRICTION IN NARROW FERROMAGNETIC WIRES USING PERPENDICULAR-CURRENT GIANT MAGNETORESISTANCE

By

Antonio Javier Zambano

A DISSERTATION

Submitted to Michigan State University
in partial fulfillment of the requirements
for the degree of

DOCTOR OF PHILOSOPHY

Department of Physics and Astronomy

2004

ABSTRACT

NEW METHOD FOR DETECTING DOMAIN WALL TRAPPING AND MOTION AT A CONSTRICTION IN NARROW FERROMAGNETIC WIRES USING PERPENDICULAR-CURRENT GIANT MAGNETORESISTANCE

By

Antonio Javier Zambano

We present a versatile, new method for detecting the presence and small motions of a trapped domain wall in a narrow ferromagnetic wire using current-perpendicular-to-plane, CPP, giant magnetoresistance, GMR. We have adapted the Ono *et al.* [1-2] method for trapping domain walls to CPP GMR measurements. We shaped a spin valve multilayer Cu(10nm)/Py(20nm)/Cu(10nm)/Py(5nm)/Cu(5nm)/Au(15nm), where Py = $Ni_{84}Fe_{16}$, into a long ~ 500-nm-wide wire with a U-shaped or V-shaped constriction (notch) near its middle that acts as a trapping site for a head-to-head (or tail-to-tail) domain wall. A sweeping external magnetic field, H, is applied along the wire axis. The magnetization is restricted to be parallel to the wire axis due to the shape anisotropy. Magnetization reversal in the wire takes place by propagation of a magnetic domain wall, which initially nucleates in a diamond-shaped reservoir and is injected from there into the nanowire at a particular value of H. As a wall in either Py layer moves past the measuring contact, the CPP GMR detects the change of the relative magnetizations of the two Py layers, from parallel to antiparallel. The CPP GMR response to small motions of the trapped domain wall is enhanced because the CPP current is restricted to the region of wall trapping; but

---

[1] T. Ono , H. Miyajima, K.Shigeto and T. Shinjo, *Appl. Phy. Lett.* **72**, 1116 (1998).

[2] T. Ono, Y. Ooka, S. Kasai, H. Miyajima, N, Nakatani, N. Hayashi, K. Shigeto, K. Mibu and T. Shinjo, *Mater. Sci. Eng.* B **84**, 126 (2001).

in addition, the CPP current can be also localized to a measuring region outside the constriction. Superconducting 150-nm-thick (top) and 100-nm-thick (bottom) Nb contacts are used to obtain a uniform CPP current density in the wall trapping region at 4.2 K; but measurements at 295K, including 200-nm-Au top contacts, have also been successful with non-uniform CPP currents. Data for the two different types of constrictions show that for U-shape notches, several pinning sites were seen as the wall in the thinner Py layer remained trapped in the constriction, while in V-shaped notches one trapping site occurred. Successful pinning of a wall at the constriction in the thicker Py layer was more improbable. With this technique, the position of the wall inside the notch region can be precisely determined. While H is swept, a wall trapped in a constriction moves between different points in the notch seeking a lower energy state, and it does not have to leave the constriction when the system is relaxed by sweeping the field to 0 Oe. When H is kept fixed, time dependence of wall position inside a U-shaped constriction in the thinner Py layer appears to be thermally activated at 4.2 K. No wall motion was observed in a V-shaped notch under the same circumstances. Along with these results, data from other studies, such as domain wall stability and effects of a high-density CPP current, are presented in this thesis to confirm the success and effectiveness of our technique.

FOR MY FATHER

ACKNOWLEDGEMENTS

I am professionally indebted to many people who have helped me in the course of my work. I am most grateful to Dr. William P. Pratt Jr., for his assistance and invaluable teaching in the field of experimental physics. My gratitude to him is for being not only an excellent adviser but also a patient and supportive person. I am also enormously thankful to Dr. Jack Bass for his guidance during the first stage of my research in this group, and for his exemplary professionalism.

I would like to thank Dr. Reza Loloee for his assistance and technical support. His knowledge and "consistently positive attitude", greatly contributed to make our work be efficient and pleasant. My deep thanks go to my co-workers and friends: Mustafa Al-haj Darwish, Huseyin Kurt, Ion Muraru, and Mike Crosser for their inestimable suggestions and constructive criticism during the development of this thesis. Each of them made our laboratory a great and friendly environment to work.

I also acknowledge the preliminary work by Robert Slater, the useful advice of Sergei Urahzdin, the assistance of Dr. Baokang Bi, the support by the Keck Microfabrication Facility and NSF grant DMR-02-02476.

Finally, I would like to express gratitude for their patience and support to my family: my mother Nené, my brother Luis, my sister Liliana, and my niece Lucia; also to my friends: Guillermo Quinteiro, Julian Mickelson, Severine Collignon, and especially Bryan Fink.

TABLE OF CONTENT

LIST OF TABLES

LIST OF FIGURES

CHAPTER 1

Theory

Current Perpendicular to the Plane Giant Magneto-resistance, Magnetic Domain Structures and Domain Walls

1.1 Introduction

In ordinary ferromagnets, F, the parallel alignment of their magnetic moments due to their strong interaction produces a large local magnetization within the F, even in absence of an external applied magnetic field, H. Yet, a F sample of macroscopic extent can exhibit zero average magnetization. Such a demagnetized state is due to the presence of *magnetic domains* with randomly oriented close-to-uniform magnetizations. When exposed to a varying H, the magnetic domain structure will change so that the sample becomes magnetized. This redistribution of the magnetic domains is established by the reduction of the overall energy of the sample. In general the minimum-energy structure of a *bulk ferromagnet* is a three-dimensional multi-domain state, within each of which the magnetic moments are aligned. For *thin films* of large lateral extent, such multi-domain states can exist, but with the constraint that the domain magnetizations are usually

parallel to the surface of the film. It is energetically more favorable for the magnetic moments to change their direction gradually rather than abruptly at the interface between adjacent domains. Between any two domains, this means there is always a transition region of finite extent within which the magnetic moments vary in direction. These regions are called domain walls, DW, whose widths and magnetic moment configurations are determined by the relative magnetic moment orientation of the adjacent domains, the anisotropies, and the exchange stiffness constant, A_{ex}, as well as local imperfections and the geometry of the ferromagnet. There are two main processes by which domains change their structure under an applied H: one is the coherent rotation of the magnetic moments of an entire domain to a more favorable orientation; the other one is the growth of favorably oriented domains, during which DWs move to incorporate more moments that have switched to a favorable orientation. DW propagation is strongly influenced by the sample shape and anisotropies[1-2].

Control and detection of geometrically confined DWs are of intense interest both for physics and device applications. One of the most important areas of magnetic technology nowadays is the study of small features where the size of the F thin-film elements used in a device is comparable to the domain size. As the size of those elements gets smaller, DW propagation mechanisms are strongly affected, and the physics involved in that process is of great interest. In this work we present an alternative scheme for detecting the presence and motion of trapped DWs that also provides enhanced sensitivity to small wall motions.

Among the different techniques that are utilized to characterize DW motions, we focus on magnetoresistance, MR, which is historically associated with the fractional

change in resistance of a sample upon the application of H. We use the giant magnetoresistance, GMR, of a magnetic multilayer, consisting of alternating thin films of F metals and non-ferromagnetic metals, N. Until now, most of the GMR studies of DW motions have used the so called current-in-plane geometry, CIP, in which the measuring current is along the plane of the multilayer. Unfortunately, in the CIP geometry, there is no control over the region of the current flow and the sample geometry independently. Thus, the sensitivity of the method is significantly reduced because there is a CIP MR contribution from regions that are not of interest. What is needed is a way to localized the measuring current to a region of interest that is somewhat independent of the sample geometry which is controlling the domain structure. We utilized a current-perpendicular-to-plane geometry, CPP, to obtain this highly-localized measuring current. Since CPP GMR is sensitive to the relative orientation of the magnetization in adjacent F layers, this GMR can, in principle, be used to provide localized information about the domain state in the F layers. Continuing with the work by Slater[3], we have adapted one of the Ono *et al.* CIP GMR methods for trapping domain walls[4-5] to CPP GMR measurements. Ono *et al.* used a $F(t_1)/N(t_N)/F(t_2)$ spin valve, SV, to trap a domain wall in a specific place and detect the wall's presence, where t means layer thickness with $t_1 \neq t_2$. The dissimilar thicknesses of the F layers make them have different switching fields. The SV was in the shape of a long wire, and a constriction situated near its center acted as a trapping site for a domain wall, see Fig.1.1 (a). In our work, a similar $F(t_1)/N(t_N)/F(t_2)$ structure was used with $t_1 < t_2$ and t_N thick enough to minimize magnetic coupling between F layers. At 4.2 K two superconducting contacts, S, guarantee a uniform CPP current flow that is confined to the region of the wall trapping in the constriction, but measurements at 295K using N

top contacts can also be done with non-uniform CPP currents. Away from the constriction, the shape anisotropy of the wire constrains the magnetizations of each F layer to be parallel to the wire axis and in a single-domain state. After application of a strong H along the +x direction, H is then increased along −x, causing the DW to propagate in the thin F layer until the wall becomes trapped in the notch as the magnetization is reversed on one side of the notch.

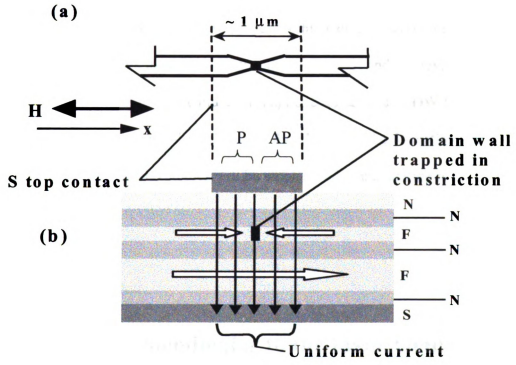

Fig. 1. 1. Domain walls move in both ferromagnetic layers at different times because of the different switching fields. As the wall moves in the thin F layer, past the top measuring contact, the resistance changes in proportion to the location of the wall. Antiparallel magnetizations of the F layers give higher value of resistance, and parallel magnetizations give a lower resistance. Superconducting contacts guarantee uniform CPP current.

The magnetization of the thick F layer remained fixed along +x. As stated before, the GMR depends on the relative orientation of the magnetization in the two F layers: when the magnetic moments of the F layers are aligned parallel, P, the resistance is lower, and

when they are aligned antiparallel, AP, the resistance is higher. The presence of a trapped wall could be detected because the CPP resistance is between the limits of both magnetizations being P or AP as the domain wall moves between the measuring contacts, as shown in Fig. 1.1 (b). As H continues increasing along –x, the DW leaves the notch causing the thinner F layer to switch completely. Further increases in H along -x causes a DW to move through the thicker F layer.

In this chapter a phenomenological review of the sources of GMR and a CPP GMR outline, which are of direct relevance to this work, are given in Sect. 1.2. A more detailed analysis of this theory can be found in Refs. 6-9, and in previous dissertations[10-11]. This chapter will also concentrate on magnetic domains and DW theory in Sect 1.3, giving a review of the central mechanisms that dominate the formation and propagation of domain walls. Thin film studies will be emphasized which are the main interest of this project.

1.2 Current Perpendicular to the Plane Giant Magneto-resistance

Magnetoresistance, MR, is the change in electrical resistance, R, of a conducting material in response to a field H. In the case of a single F layer, the ordinary MR consists mainly of two components: (1) a contribution from the bulk, part of which is anisotropic MR, AMR, and Lorentz MR, LMR, and (2) a small contribution from the domain walls,

DWR. AMR has its origin in the spin-orbit coupling, and its main characteristic is that R is different for current flowing parallel or perpendicular to H. LMR comes from the Lorentz force that the magnetic field, even in the absence of an externally applied field, exerts on the moving electrons. DWR arises from the electron scattering in the domain walls[12-14].

GMR refers to the MR of F/N multilayers, and it is much larger than the MR of each constituent bulk material. Only in certain special cases is the GMR comparable or smaller than the combination of AMR, LMR, and DWR[7]. GMR also arises in a variety of magnetic systems including multilayers, spin valves, and granular materials. Their common property is that they consist of separated regions of magnetic material capable of adopting independent magnetization orientations in response to H. Viewed differently, GMR arises from the transfer of magnetic information by the carriers from one magnetic region to another across the intermediate non magnetic spacer metal, and the information is coded in the chemical potentials of up and down electrons and also depends on the decay of coding in transit.

The discovery of GMR effect in Fe/Cr magnetic multilayers in 1998 has initiated a tremendous research effort on layered magnetic systems[6-8, 15-17]. GMR stimulated interest in understanding the physical processes involved and accelerated the emergence of new technology, now called *spintronics*[18-19], which has the potential to replace much of the traditional electronic technology based only on the charge of electrons. GMR is also used as a sensor for probing other phenomena such as the coupling between F layers when separated by N layers[20-24] and the generation of magnons and magnetization switching by a high-intensity spin-polarized electric current[25-32].

Since the earliest times, almost all of the MR experiments have been carried out in the CIP geometry. The reason is simple; it is very easy to measure the fairly large resistance of a thin film or multilayer when the current flows in plane because the sample length is typically orders of magnitude larger than its thickness. However, for CPP GMR, the geometry is the opposite: the main length of the sample is just its thickness, while the lateral dimensions of the sample are usually much larger than the thickness. Therefore the resulting very low resistance can be measured reliably only by extremely sensitive techniques. In order to increase the CPP R to easily observable values, microfabrication or even nanofabrication technologies can be used to reduce the cross section of the samples. The first CPP GMR measurements were reported by W. Pratt and collaborators at Michigan State University in 1991, and they showed that CPP GMR could be several times larger than CIP GMR[33]. Because of its high symmetry, only simple equations are necessary to describe CPP GMR theoretically[7-8, 34-35]; and in contrast to CIP GMR theory, this allows a straightforward analysis of multilayers. CPP transport analysis in F/N multilayers began with a phenomenological two current model[35-36], and later on, more rigorous theories were developed[6-8]. For convenience they can be divided into two categories: *Free Electron Based Models,* semiclassical models neglecting quantum effects, and *Fermi Surface Models*, inherent to quantum mechanics, and whose main issue is the coherence of the electron scattering from adjacent interfaces.

Semiclassical models are appropriate instruments to analyze and explain the results in this thesis. Thus, it is not necessary go deeper into quantum mechanic models; further information on *Fermi Surface Models* can be found elsewhere[36-37].

The development of *semiclassical models* started with Zhang and Levy[34], who pointed out that the free-electronic transport can be described in terms of two independent parallel channels (spin-up and spin-down) in the diffusive regime. Here the thicknesses involved in the system must be longer than the elastic mean free path of the electrons, λ, (in contrast to the ballistic regime); and also weak spin-flip scattering is assumed, in which the electron spin-flip scattering processes occur on a much longer time scale than the elastic electron scattering events. It was Lee *et al.* who first wrote down the equations to describe a two parallel-channel model[35]. The scattering of the electrons carried by each channel is spin dependant with different scattering rates and can be described phenomenologically in terms of different resistivities for majority and minority electrons, i.e. electrons with their magnetic moment pointing parallel or antiparallel to the local magnetization, respectively. Later, Valet and Fert, VF, used the Boltzmann formalism, to extend this model to include *spin memory loss* due to spin flipping in the bulk of the metals; this mechanism is measured by a quantity called the *spin diffusion length* [38-41], l^F_{SF} and l^N_{SF} for F and N metals, respectively. Finally, one of the last steps in the development of the semiclassical models was the inclusion of spin-flip scattering at the interface by Fert and Lee[42], who generalized VF model by adding spin memory loss at the interfaces through a modification of the boundary conditions.

For samples in which no spin-flipping occurs anywhere in the multilayer, the Michigan State University group has demonstrated[43-44] that a two-channel-series-resistor-model (two spin channels carrying currents independently), 2CSR, accurately described the experimental data. This 2CSR model comes out as a particular case of the VF model when $l_{SF} >> t$ in the F layer and N layers.

1.2.1 Giant Magneto-resistance. Semiclassic Analysis

GMR arises from spin dependent scattering in F metals and at F/N interfaces[16]. Such scattering depends on impurities and crystal defects present in both F and N metals, thermal vibrations of the lattice, mixing of the F and N metals at the interfaces, and the band structures of the F and N metals. The band structure of a F material is magnetic moment dependent. That is, the energy, ε, of d bands with one moment direction are shifted relative to the ε of d bands with the opposite moment direction. At the Fermi surface, this shifting leads to a difference in the density of states, $\mathcal{D}(\varepsilon)$, for each d band. This situation is represented in Fig 1.2, where a simple sketch of s energy bands and d energy bands of a N metal and a F metal is shown. Transport is carried by s electrons because their effective mass is much lower than that of d electrons. If electrons do not flip their magnetic moments during scattering, the majority s electrons, moment up, would scatter mostly into other majority s electron states, because there are few majority d electron states available close to the Fermi energy. Minority electrons, moment down, in contrast, can scatter more often into the larger number of minority d states at the Fermi energy. These different scattering processes generate a different scattering probability for electrons with magnetic moments parallel and antiparallel to the local magnetization. This difference is called *spin anisotropy*.

To describe how GMR comes from the spin dependent scattering, consider a F/N/F trilayer. The system is shown in Fig. 1.3, for two relative states of magnetization of adjacent F layers: AP or P with respect to a fixed direction in space. Electrons entering the trilayer are divided into two groups: majority and minority electrons. If no spin and

momentum are transferred between these groups, they can be treated as two separate *spin channels* of conduction. This channel separation requires low temperature where electron-magnon and electron-phonon scatterings are negligible. Then, the total R can be calculated from the contribution of two different resistances in parallel for majority and minority electrons. Usually the minority electrons are more strongly scattered in F metals and at F/N interfaces, than majority ones.

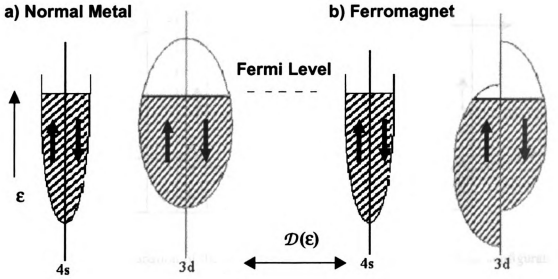

Fig. 1. 2. Simplified diagram of the 4s and 3d energy, ε, bands vs. density of states, $\mathcal{D}(\varepsilon)$, of: a) a normal metal, no net magnetic moment, and b) a ferromagnetic metal, there is a net magnetic moment.

When the magnetizations are in the AP state, see Fig.1.3, one electron group will scatter strongly in the first F layer and weakly in the second F layer, and vice versa for the other group, contributing equally to the total resistance, R_{AP}. When the magnetizations are in the P state, the up electrons will be scattered weakly in both F layers, shorting out the total resistance, while the down electrons will be scattered

strongly in both layers. Consequently, the net resistance, R_P, will be smaller than that in the AP state, $R_P < R_{AP}$. GMR is usually computed as:

$$GMR = \frac{A\Delta R}{AR_P} \tag{1.1}$$

where $A\Delta R = A \times \Delta R = A \times (R_{AP}-R_P)$ is the difference of specific resistances for AP and P states, and A is the area of the CPP current flow.

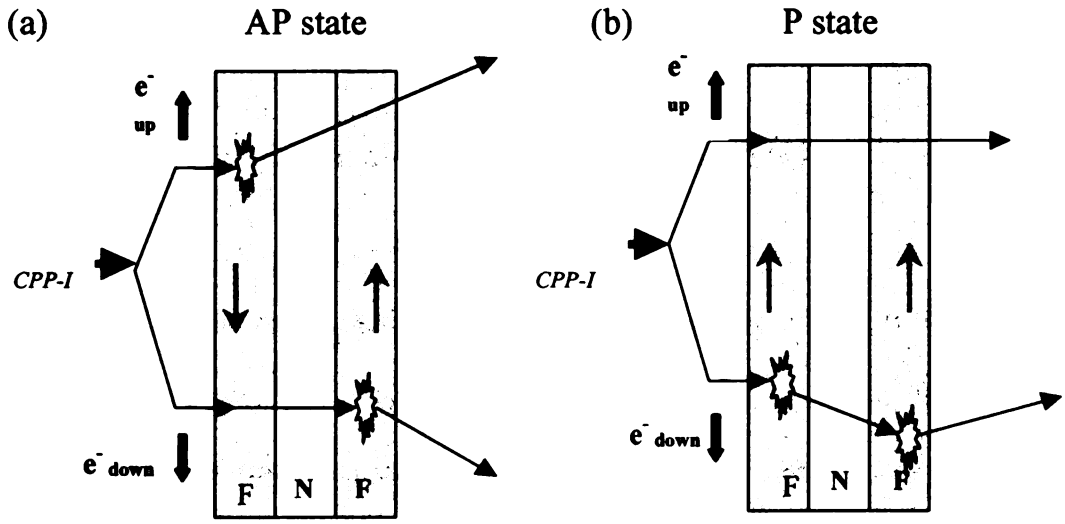

Fig. 1.3. Schematic explanation of the basic GMR effect for a particular magnetic configuration. a) When the magnetizations (arrows) of the magnetic layers are antiparallel, both moment-up and moment-down electrons have equal resistance path. b) When the magnetizations of the F layers are parallel, the moment-up electrons have a lower resistance path compared with moment-down electrons, leading to a lower overall resistance

To produce P states, it is necessary to apply an external magnetic field strong enough to align the moments of the F layers along the field. Because the AP state is more elusive, there are typically three ways to produce it: i) Using an exchange-biased spin valve, EBSV, consisting of two F layers separated by a N layer thick enough to prevent coupling. The magnetic moment of a free F layer can be switched while the magnetic moment of a F pinned layer is fixed due to contact to an antiferromagnetic layer. [45-46] ii)

Using antiferromagnetic exchange coupling between two adjacent F layers separated by a N layer.[15-16, 20-24] iii) Using a hybrid spin valve, SV. It is composed of two F layers of different switching fields, separated by a sufficient thick N layer to prevent coupling. Studies using such an asymmetric hybrid SV are part of this dissertation, and a more detailed description of our system can be found in Chap. 2.

1.2.2 Total Resistance of an asymmetric F/N/F Trilayer using the Two-current Series-resistor Model (2CSR)

In this simple model, the electrons travel through each layer and the interfaces, sampling the magnetic order, regardless of the mean free path. The different scattering rates make the bulk resistivity of the majority electrons, $\rho^{\uparrow}$, and minority electrons, $\rho^{\downarrow}$, distinct. Similarly, the interfaces also have spin-dependent scattering, characterized by specific resistances, for majority electrons, $AR^{\uparrow}$, and for minority electrons, $AR^{\downarrow}$. Lee et al.[35] elaborated the first equations of the 2CSR introducing parameters to describe what happens in the bulk of N and F and at their interfaces. The most relevant ones are the following two dimensionless parameters: bulk spin asymmetry β, and interfacial spin asymmetry γ:

$$\beta = \frac{\rho^{\downarrow} - \rho^{\uparrow}}{\rho^{\downarrow} + \rho^{\uparrow}} \qquad \text{and} \qquad \gamma = \frac{AR^{\downarrow} - AR^{\uparrow}}{AR^{\downarrow} + AR^{\uparrow}} \tag{1.2}$$

In addition to β and γ, the measured bulk resistivities of the metals, ρ, the interfacial specific resistances, AR, and layer thicknesses, t, are enough parameters to

describe CPP GMR. The thicknesses of the layers are the only lengths taken into account; the rest of the parameters are independent of t. Recall that spin-flip scattering is assumed to be negligible in the 2CSR model.

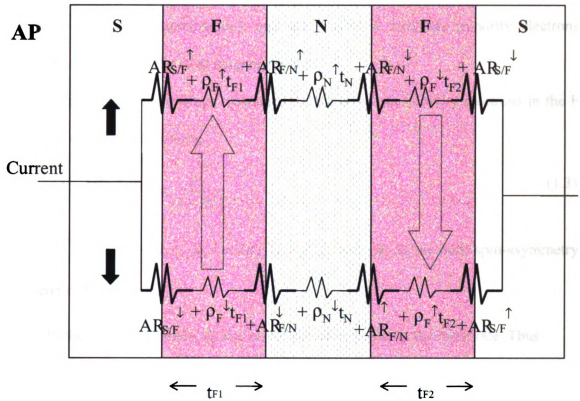

Fig. 1. 4. Diagram of the 2CSR model for the AP state of an asymmetric F/N/F trilayer with superconducting contacts. Big arrows indicate orientation of local magnetization. F layers have different thicknesses. The current is divided into two channels: moment up channel and moment down channel. There is one resistance per channel that is the sum of each resistance in series. The total resistance is the combination of the resistance of each channel in parallel.

Consider a relatively simple case that can be studied with the 2CSR model: two F layers of different thicknesses, separated by a N layer, see Fig. 1.4. Two S contacts at the ends guarantee uniform CPP current flow through area A for $T < T_C$, where T_C is the critical temperature of S. The dissimilar thicknesses of the F layers produces switching fields different enough to allow AP alignment under field reversal. The different F layer

thicknesses makes this F/N/F trilayer asymmetric, producing somewhat more complex algebraic final results for the CPP resistance.

We use the following notation: subscript N always refers to N metals and subscript F always refers to F metals. The symbol ↑ indicates majority electrons (moment parallel to the local magnetization), and the symbol ↓ indicates minority electrons (moment antiparallel to the local magnetization).

A measure of the average resistance for majority and minority electrons in the F layers is given by the following:

$$\rho_F^* = \frac{(\rho_F^{\uparrow} + \rho_F^{\downarrow})}{4} = \frac{\rho_F}{(1-\beta_F^2)} \tag{1.3}$$

where $\rho_F{}^{\uparrow} = 2\rho_F{}^*(1-\beta_F)$, $\rho_F{}^{\downarrow} = 2\rho_F{}^*(1+\beta_F)$, and β_F is the bulk spin-asymmetry parameter of the F metal.

In the case of N metals, up and down electrons scatter at the same rate. Thus:

$$\rho_N^* = \frac{(\rho_N^{\uparrow} + \rho_N^{\downarrow})}{4} = \frac{\rho_N}{(1-\beta_N^2)} = \rho_N \tag{1.4}$$

where $\beta_N = 0$, and $\rho_N^{\uparrow} = \rho_N^{\downarrow} = 2\rho_N$.

An equivalent analysis for the F/N interfaces defines the average interfacial specific resistance for majority and minority electrons:

$$AR_{F/N}^* = \frac{AR_{F/N}^{\uparrow} + AR_{F/N}^{\downarrow}}{4} = \frac{AR_{F/N}}{(1-\gamma_{F/N}^2)} \tag{1.5}$$

where $A_{F/N}^{\uparrow} = 2AR^*(1-\gamma_{F/N})$, $A_{F/N}^{\downarrow} = 2AR^*(1+\gamma_{F/N})$, and $\gamma_{F/N}$ is the interface spin asymmetry parameter.

It is assumed that the S/F interface resistance is spin-independent, and thus $\gamma_{S/F} = 0$. This gives:

$$AR^{\uparrow}_{S/F} = AR^{\downarrow}_{S/F} = 2\,AR^{*}_{S/F} \tag{1.6}$$

where $AR^{*}_{S/F} = AR_{S/F}$.

The specific resistance of each channel is the series sum of resistivities of individual layers times their thickness, plus the interfacial specific resistances. Thus, the total CPP AR is equal to the parallel addition of the sum of specific resistances of the two spin channels as described in Fig. 1.4.

In case of the *AP state*, ARs for spin-up and spin-down electrons can be written as:

$$AR_{AP}(up) = 2AR^{\uparrow}_{S/F} + \rho^{\uparrow}_{N} t_{N} + \rho^{\uparrow}_{F} t_{F_1} + \rho^{\downarrow}_{F} t_{F_2} + AR^{\uparrow}_{F/N} + AR^{\downarrow}_{F/N} \tag{1.7.a}$$

$$AR_{AP}(down) = 2AR^{\downarrow}_{S/F} + \rho^{\downarrow}_{N} t_{N} + \rho^{\downarrow}_{F} t_{F_1} + \rho^{\uparrow}_{F} t_{F_2} + AR^{\downarrow}_{F/N} + AR^{\uparrow}_{F/N} \tag{1.7.b}$$

Further steps can be taken by placing Eqs. 1.3 to 1.6 into Eqs. 1.7 to get the specific resistance of each channel in term of the average specific interface resistances, average bulk resistivities, thicknesses, and spin asymmetry parameters of the multilayer:

$$AR_{AP}(up) = 4AR_{S/F} + 2\rho_{N} t_{N} + 2\rho^{*}_{F} t_{F_1}(1-\beta) + 2\rho^{*}_{F} t_{F_2}(1+\beta) + 4AR^{*}_{F/N} \tag{1.8.a}$$

$$AR_{AP}(down) = 4AR_{S/F} + 2\rho_{N} t_{N} + 2\rho^{*}_{F} t_{F_1}(1+\beta) + 2\rho^{*}_{F} t_{F_2}(1-\beta) + 4AR^{*}_{F/N} \tag{1.8.b}$$

Since the two channels resistances are in parallel, the total specific resistance of the system in the AP state is given by:

$$\frac{1}{AR_{AP}} = \frac{1}{AR_{AP}(up)} + \frac{1}{AR_{AP}(down)} \tag{1.9}$$

Combining Eqs. 1.8 and 1.9, AR_{AP} comes out as:

$$AR_{AP} = 2AR_{S/F} + \rho_N t_N + \rho_F^{\bullet}(t_{F_1} + t_{F_2}) + 2AR_{F/N}^{\bullet} - \frac{(\rho_F^{\bullet}(t_{F_1} - t_{F_2})\beta)^2}{(2AR_{S/F} + \rho_N t_N + \rho_F^{\bullet}(t_{F_1} + t_{F_2}) + 2AR_{F/N}^{\bullet})} \tag{1.10}$$

Analogous treatment can be done to obtain AR for the *P state*. Combining the specific resistivities and interfacial specific resistances of each channel, ARs for spin-up and spin-down electrons become:

$$AR_P(up) = 2AR_{S/F}^{\uparrow} + \rho_N^{\uparrow} t_N + \rho_F^{\uparrow} t_{F_1} + \rho_F^{\uparrow} t_{F_2} + 2AR_{F/N}^{\uparrow} \tag{1.11.a}$$

$$AR_P(down) = 2AR_{S/F}^{\downarrow} + \rho_N^{\downarrow} t_N + \rho_F^{\downarrow} t_{F_1} + \rho_F^{\downarrow} t_{F_2} + 2AR_{F/N}^{\downarrow} \tag{1.11.b}$$

Placing Eqs. 1.3 to 1.6 into Eqs. 1.11, ARs can be obtained as function of the average specific resistivities, average specific interface resistances, thicknesses, and spin asymmetry parameters:

$$AR_P(up) = 4AR_{S/F} + 2\rho_N t_N + 2\rho_F^{\bullet} t_{F_1}(1-\beta) + 2\rho_F^{\bullet} t_{F_2}(1-\beta) + 4AR_{F/N}^{\bullet}(1-\gamma) \tag{1.12.a}$$

$$AR_P(down) = 4AR_{S/F} + 2\rho_N t_N + 2\rho_F^{\bullet} t_{F_1}(1+\beta) + 2\rho_F^{\bullet} t_{F_2}(1+\beta) + 4AR_{F/N}^{\bullet}(1+\gamma) \tag{1.12.b}$$

Then the total AR_P is given by the sum in parallel of the resistances in Eqs. 1.12:

$$\frac{1}{AR_P} = \frac{1}{AR_P(up)} + \frac{1}{AR_P(down)} \tag{1.13}$$

$$AR_P = 2AR_{S/F} + \rho_N t_N + \rho_F^*(t_{F_1} + t_{F_2}) + 2AR_{F/N}^* - \frac{(\rho_F^*(t_{F_1} + t_{F_2})\beta + 2AR_{F/N}^*\gamma)^2}{(2AR_{S/F} + \rho_N t_N + \rho_F^*(t_{F_1} + t_{F_2}) + 2AR_{F/N}^*)} \tag{1.14}$$

The difference between AR_P and AR_{AP} can be easily derived from Eqs. 1.10 and 1.14, giving $A\Delta R$ which is one of the most useful quantities to characterize a multilayer system and determine its GMR.

$$A\Delta R = AR_{AP} - AR_P = \frac{4(\rho_F^* t_{F_1}\beta + AR_{F/N}^*\gamma)(\rho_F^* t_{F_2}\beta + AR_{F/N}^*\gamma)}{(2AR_{S/F} + \rho_N t_N + \rho_F^*(t_{F_1} + t_{F_2}) + 2AR_{F/N}^*)} \tag{1.15}$$

1.2.3 Inclusion of Spin Diffusion Length in a F/N/F Trilayer Resistance Calculation

As we will show in Sect. 2.2, our actual trilayer system has $t_{F1} >> l^F_{SF}$ and $t_{F2} \cong l^F_{SF}$. Thus, to compute AR_{AP}, AR_P, and $A\Delta R$, it is necessary to utilize models which include spin diffusion lengths, such as the VF model[38], which can describe accurately our system. The VF model assumes that spin-flipping occurs in the bulk of the F and N layers and calculates AR for l^F_{SF} and l^N_{SF} of any size with respect to t_F and t_N. In the limit that $l^F_{SF} >> t_{F1}$ and $l^N_{SF} >> t_N$, the VF model agrees with the 2CSR model.

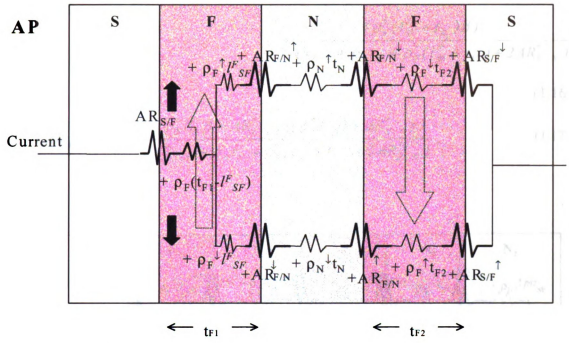

Fig. 1. 5. Diagram of the 2CSR model for the AP state of a tri-layer F/N/F with superconducting contacts. F layers have different thicknesses. The inclusion of the spin diffusion length in the first F layer, $t_{F1} >> l^F_{SF}$, shortens the two channels. The current is divided into two channels: moment up channel and moment down channels. There is one resistance per channel that is the sum of each resistances in series. The total resistance is the combination of the resistance of each channel in parallel plus the contributions of that part of F_1 not in the two-channel region and the S/F boundary resistance on the left.

Without going through the VF formalism strictly with its complicated calculations, a simple modification of the 2CSR model is adequate to estimate the value of the total AR_P and AR_{AP}, which agrees with those values given by the VF model. Since $t_{F1} >> l^F_{SF}$, only a thin region of thicknesess l^F_{SF}, next to the F/N interface, participates in the two spin-channel conduction. The rest of the F_1 layer just looks like a single resistor as illustrated in Fig. 1.5. Since $t_{F2} \approx l^F_{SF}$ we ignore spin-memory loss and apply the usual 2CSR model to the F_2 layer.

Under these conditions and following similar calculations to the ones described in Sect. 1.2.2, AR_{AP} and $A\Delta R$ come out as:

$$AR_{AP} = 2AR_{S/F} + \rho_F(t_{F_1} - l^F_{SF}) + \rho_N t_N + \rho^*_F(l^F_{SF} + t_{F_2}) + 2AR^*_{F/N} - \frac{(\rho^*_F(l^F_{SF} - t_{F_2})\beta)^2}{(AR_{S/F} + \rho_N t_N + \rho^*_F(l^F_{SF} + t_{F_2}) + 2AR^*_{F/N})} \quad (1.16)$$

$$A\Delta R = AR_{AP} - AR_P = \frac{4(\rho^*_F l^F_{SF}\beta + AR^*_{F/N}\gamma)(\rho^*_F t_{F_2}\beta + AR^*_{F/N}\gamma)}{(AR_{S/F} + \rho_N t_N + \rho^*_F(l^F_{SF} + t_{F_2}) + 2AR^*_{F/N})} \quad (1.17)$$

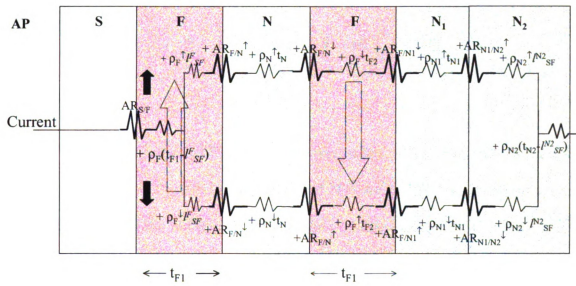

Fig. 1.6. Diagram of the 2CSR model for the AP state of N_2 right contact. The right Nb layer in Fig. 1.5 is replaced by a N_1+ N_2 layer. The inclusion of the spin diffusion length in the N_2 layer, $t_{N2} >> l^{N2}_{SF}$, shortens the two channels.

Another system which is of interest for this work is shown in Fig. 1.6, which is the result of modifying the system presented in Fig.1.5, where the right superconducting layer is replaced by a N_1+N_2 bilayer. In this case, $t_{N2} >> l^{N2}_{SF}$, and similarly to what happens in the F_1 layer, only a thin region of thickneseess l^{N2}_{SF}, next to the N_1/N_2 interface, participates in the two spin-channel conduction. The rest of this N_2 layer just

looks like a single resistor as illustrated in Fig. 1.6. For the N_1 layer, one assumes $t_{N1} << l^{N1}_{SF}$. The values of AR_{AP} and $A\Delta R$ can be calculated with Eqs. 1.18.

$$AR_{AP} = AR_{S/F} + \rho_F(t_{F_1} - l^F_{SF}) + \rho_N t_N + \rho^*_F(l^F_{SF} + t_{F_2}) + \rho_{N_1} t_{N_1} + \rho_{N_2} t_{N_2} +$$

$$+2AR^*_{F/N} + AR^*_{F/N_1} + AR^*_{N_1/N_2} \frac{(\rho^*_F(l^F_{SF} - t_{F_2})\beta - AR^*_{F/N_1}\gamma_{F/N_1})^2}{(2AR^*_{F/N} + \rho^*_F(l^F_{SF} + t_{F_2}) + \rho_N t_N + AR^*_{F/N_1} + \rho_{N_1} t_{N_1} + \rho_{N_2} l^{N_2}_{SF} + AR^*_{N_1/N_2})} \tag{1.18}$$

$$A\Delta R = AR_{AP} - AR_P =$$

$$= \frac{4(\rho^*_F l^F_{SF}\beta + AR^*_{F/N}\gamma)(\rho^*_F t_{F_2}\beta + AR^*_{F/N}\gamma + AR^*_{F/N_1}\gamma)}{(\rho_N t_N + \rho_{N_1} t_{N_1} + \rho_{N_2} l^{N_2}_{SF} + \rho^*_F(l^F_{SF} + t_{F_2}) + 2AR^*_{F/N} + AR^*_{F/N_1} + AR^*_{N_1/N_2})} \tag{1.19}$$

Now if we assume that S = Nb, F = Py (permalloy = $Ni_{84}Fe_{16}$), and N= Cu in Fig 1.5 and S = Nb, F = Py, N= Cu, N_1= Cu, and N_2= Au in Fig 1.6, these two systems represent, as we will see in Chap. 2, our two types of actual samples with Nb-top contact and Au-top contact, respectively, both with Nb bottom contacts. Calculations of AR_{AP}s and $A\Delta$Rs of these systems using Eqs. 1.16, 1.17, 1.18 and 1.19, see Table 1.2, are very useful to predict and analyze our experimental data. As mentioned before, these equations are valid only for low temperature. At this point, we have to mention that our actual samples have a 10nm-thin-Cu layer inserted between the multilayer and the bottom superconducting Nb contact, and a 5nm-thick-Cu + 15nm-thick-Au layer next to the top contact. We assume that the proximity effect, to superconducting Nb, allows Cooper pairs to pass through the N metals, so that we only need to consider an effective Nb/Py interface[47]. The values of AR*, ρ*, t, and l_{SF} used in these calculations are shown in Table 1.1. The spin asymmetry parameters are $\beta = 0.73$ and $\gamma = 0.7$.[48]

F_1	ρ^*_{Py}=	0.263	μΩ m	t_{py}=	20 nm	$AR^*_{Py/Cu}$=	0.51 fΩ m^2	l^{Py}_{SF}= 5.5 nm
F_2	ρ^*_{Py}=	0.263	μΩ m	t_{py}=	5 nm			
N	ρ_{Cu}=	0.006	μΩ m	t_{Cu}=	10 nm	$AR_{Nb/Py}$=	3.00 fΩ m^2	l^{Cu}_{SF}= 450 nm
N_1	ρ_{Cu}=	0.006	μΩ m	t_{Cu}=	5 m			
N_2	ρ_{Au}=	0.02	μΩ m	t_{Au}=	107nm	$AR_{Au/Cu}$=	0.175 fΩ m^2	l^{Au}_{SF}= 35 nm

Table 1.1. Values of average bulk resistivities, ρ*, thicknesses, t, average specific interface resistances, AR* and spin diffusion lengths l_{SF}. Values obtained from Refs. 48, 49 and 50.

Other helpful quantities to be considered in our calculations are R_{AP} and AR_{AP}, also included in Table 1.2. They were obtained by dividing the calculated values of AR_{AP} and AΔR by an estimation of the CPP current flow area. As we will see in Chap. 2, basically two types of constrictions were built in our nanowires. For the purpose of our calculations, they have different effective current areas. These two kinds of constrictions are: U-shaped notches of current flow area A ~ 1.5 x 10^{-13} m^2 and V-shaped notches of current flow area A ~ 2.2 x 10^{-13} m^2. These areas were estimated by averaging over the measured areas (using a scanning electron microscope) of 3 typical U-shaped-notch samples, and 5 typical V-shaped-notch samples (considering the actual dimensions of the samples after SiO deposition, see Sect 2.2.4). Table 1.2 also contains the results of the calculation of GMR percentages utilizing Eq. 1.1.

Contact	AR_{AP} (f Ωm^2)	AΔR (fΩm^2)	R_{AP} (mΩ)	ΔR (mΩ)	GMR (%)
Nb-U	~11.6	~1.1	~ 77	~ 7.2	~ 10
Au-U	~11.2	~1.6	~ 75	~ 11	~17
Nb-V	~11.6	~1.1	~ 55	~ 5.2	~10
Au-V	~11.2	~1.6	~ 53	~ 7.9	~17

Table 1.2. Low temperature values of AR_{AP} and AΔR calculated with Eqs. 1.17 and 1.18, for S = Nb, F = Py, and N= Cu in Fig 1.5, Nb top contact; and S = Nb, F = Py, N= Cu, N_1= Cu and N_2= Au in Fig 1.6, Au top contact. R_{AP} and AR_{AP}, for the same systems with estimated area of A~ 1.5 x 10^{-13} m^2 for U notches and A~ 2.2 x 10^{-13} m^2 for V notches. GMR percentage obtained with Eq.1.1.

1.3 Magnetic Domain Structures and Domain Walls

1.3.1 Magnetic Domain Structures - Total Free Energy

In a F material the redistribution of the magnetic domains is established by the reduction of the overall total free energy of the sample, based on several competing energies. In a perfect single crystal, the energy minimization calculations can be strictly carried out. However, the presence of imperfections, such as strains, inhomogeneous internal fields, grain boundaries in polycrystalline samples, etc., can radically change the details of the domain configuration, and thus complicate those calculations. Based on the energy density's dependence on the local value of the magnetization, $\vec{J}$, direction, $\vec{m} = \frac{\vec{J}}{|\vec{J}|}$, the competing energies can be divided into two groups: *local contribution* terms, which depend solely on $\vec{m}$, and *non local contributions* terms, which do not depend on $\vec{m}$ exclusively. Summing up those main contributions, the total free energy can be written as an integral over the sample volume, V:

$$E_{total} \cong \int [\, A_{ex}(\nabla \vec{m})^2 + F_{an}(\vec{m}) - \vec{H}\,.\vec{J} - \frac{1}{2}\vec{H}_d\,.\vec{J} - \overleftrightarrow{\sigma}_{ex}\,.\overleftrightarrow{\varepsilon}^{o}\,]\,dV$$

$$\text{Total energy} \cong E_{ex}\ (\text{exchange}) + E_a(\text{anisotropy}) + E_z\ (\text{ext. field}) + E_d\ (\text{stray field}) + E_s\ (\text{ext. stress})$$

(1.20)

F_{an} is a function which collects all contributions from crystal and structural magnetic anisotropies, and $\vec{H}$ and $\vec{H}_d$ are the external and the stray (or demagnetizing)

fields, respectively. The symmetric tensor $\bar{\sigma}_\alpha$ collects all stresses of non-magnetic origin, $\varepsilon^e(\vec{m})$ is the free magneto-elastic deformation at any given point[51].

The first *local* energy contribution is the *exchange energy*, E_{ex}, which causes a preference for a constant direction of the magnetization. Changes from this equilibrium invoke an energy penalty which can be described by the stiffness expression:

$$E_{ex} = A_{ex} \int (\nabla \vec{m})^2 \, dV \tag{1.21}$$

where A_{ex} is the stiffness constant, which depends upon the material, giving a measure of the strength of the coupling between the spins in the material.

The second *local* contribution is the *anisotropy energy*, E_a. This energy depends on the direction of magnetization relative to the structural axes of the material. F crystals have preferred axes of magnetization, easy axes, which arise from the band structure of the material and the spin orbit interaction. This tendency of the F magnetization to align along these easy axes is named anisotropy. The most relevant one is the crystal anisotropy, but there are other types such as the surface anisotropy, and interface anisotropy, etc. These various anisotropy effects can be characterized with a constant K. In this work, all of them are ignored because of their small contribution to the total free energy. As we will see later when analyzing the magnetostatic energy (or stray field energy), one of the reasons to neglect E_a is that stray-field effects are much stronger than those of the various anisotropies. Another important reason arises from the structural features of our samples. The sputtered Py (used to make our actual sample) grows in randomly-orientated fcc-structured-columns which have in-plane grain sizes of ~ 5-15 nm[52-54]. Columns grow with (111) texture[55] with their magnetization easy axes along the

⟨110⟩ "in-film-plane" directions. Since these grains are arbitrarily-orientated and also smaller than the shortest lateral dimension of our samples ("the notch width"~ 100 nm), the anisotropy effects are considerably reduced.

The third *local* energy contribution is the *external field or Zeeman energy*, E_z; it comes from the interaction of $\vec{H}$ and the magnetization:

$$E_z = -J_s \int \vec{H} \cdot \vec{m} \; dV \tag{1.22}$$

where J_s is the magnitude of the saturation magnetization. For uniform H, this energy depends on the average magnetization only.

There are three *non local* magnetic energy contributions: The largest is variously called *the magnetostatic energy, demagnetizing field energy, stray field energy*, or *dipole energy*, E_d, and comes from the energy of the magnetic field created by the magnetization. The usual form of this term is:

$$E_d = \frac{1}{2}\mu_0 \int_{all-space} H_d^2 dV = -\frac{1}{2} \int_{sample} \vec{H}_d \cdot \vec{J} dV \tag{1.23}$$

where μ_o is the permeability constant. The mechanism relating the preferred magnetization direction with the external sample shape is called shape anisotropy, and it is quantified through the magnetostatic energy. For example, consider the extreme case where an infinite plate of thickness t is uniformly magnetized perpendicular to its plane, as shown in Fig.1.7. The resulting energy density for this uniaxial-like shape anisotropy, can be quantified by:

$$e_d = -\frac{1}{2} H_d \cdot \vec{J} = \frac{J_s^2}{2\mu_o} \tag{1.24}$$

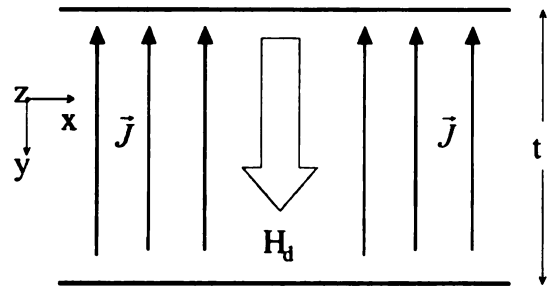

Fig. 1.7. Sketch of the demagnetization field for an uniaxial-like shape anisotropy in a plate of thickness t and infinite extension in x-z plane that is uniformly magnetized perpendicular to its plane.

This maximum energy density is given by $K_d = \frac{J_s^2}{2\mu_0}$. $Q = K/K_d$, measures the competition between various anisotropies, K, and this maximal shape anisotropy. When Q is small, the maximal shape effects are stronger than the other anisotropy effects.

When there are *stresses of non magnetic origin* present, the last term in Eq. 1.20 describes the interaction of magnetization with *external stresses*, or non-magnetic internal stresses resulting from dislocations, inhomogeneities in temperature, structure or composition. For an isotropic material and uniaxial stress along the axis of unit vector $\vec{a}$, the magneto elastic coupling energy can be expressed by:

$$E_s = \int -\frac{3}{2}\zeta_s \sigma \left[(\vec{m} \cdot \vec{a})^2 - \frac{1}{3} \right] dV \qquad (1.25)$$

which describes a uniaxial anisotropy along the stress axis with an anisotropy constant of $K_u = 3/2\ \zeta_s \sigma$; where ζ_s is a dimensionless material parameter indicating the strength of the elastic interaction.

The weakest contribution, which is not included in Eq. 1.20, is the energy associated with the elastic interactions between regions magnetized along different axes, the so called *magnetostrictive energy*; it is neglected in this work due to its minor contribution to the total balance of free energy.

As we stated before, the balance of the mentioned energies determines the domain structure in F films. For a very thin magnetic film, unless there is a magneto-crystalline easy axis perpendicular to the plane of the film, the magnetization will lie in the plane of the film due to the large shape anisotropy. For polycrystalline films, there is no preferred in-plane direction, since all orientations of the magnetization in the plane are equally probable. For very thin films, demagnetization effects over most of the plane of the film proper can be ignored. However, the edge of the film may still show demagnetization effects in order to minimize the energy, for example, 90^{o} domains of closure. The best way to understand this is through a simple example for a single-crystal film. Consider a rectangular thin-film crystal magnetized entirely along the easy axis, as shown in Fig 1.8 (a). The magnetostatic energy of the sample is reduced by approximately a factor of two if the configuration is divided into two separate oppositely magnetized domains, see Fig. 1.8 (b). By adding more oppositely magnetized domains (Fig. 1.8 (c)), the magnetostatic energy would reduce until the energy necessary to produce a new boundary between domains is greater than the energy reduction. This is because the addition of a new domain also creates a "domain wall", which is the transition region of finite extent between the two magnetization domains, where the magnetic moments vary in direction. The creation of a domain wall requires an increase of the exchange energy and anisotropy energy of the system. In this simple example, we are ignoring possible magnetostatic energy contribution to the domain-wall itself. Thus, at this point, the combination of the exchange and anisotropy energies mainly rule the production of new boundaries and adding opposite domains along the easy axis is not enough to reduce the total energy. Formation of triangular closure domains at the edges of the rectangle with magnetization

at 90° to the original domains (Fig. 1.8 (d)) makes it possible to drastically reduce the stray magnetic field and thus the magnetostatic energy. However, those closure domains are magnetized in the hard direction, introducing anisotropy energy to the system. Along with the emergence of closure domains, new domain walls appear, whose formation adds more exchange and anisotropy energy to the total free energy. Thus, the creation of closure domains helps decrease the total energy until the magnetostatic energy reduction is equal to the increase of exchange energy and anisotropy energy of the system. In the ideal case, poles of magnetization disappear from the surface, making the magnetostatic energy equal to zero. In a more realistic case, the magnetostatic energy is diminished but residual poles remain on the surface.

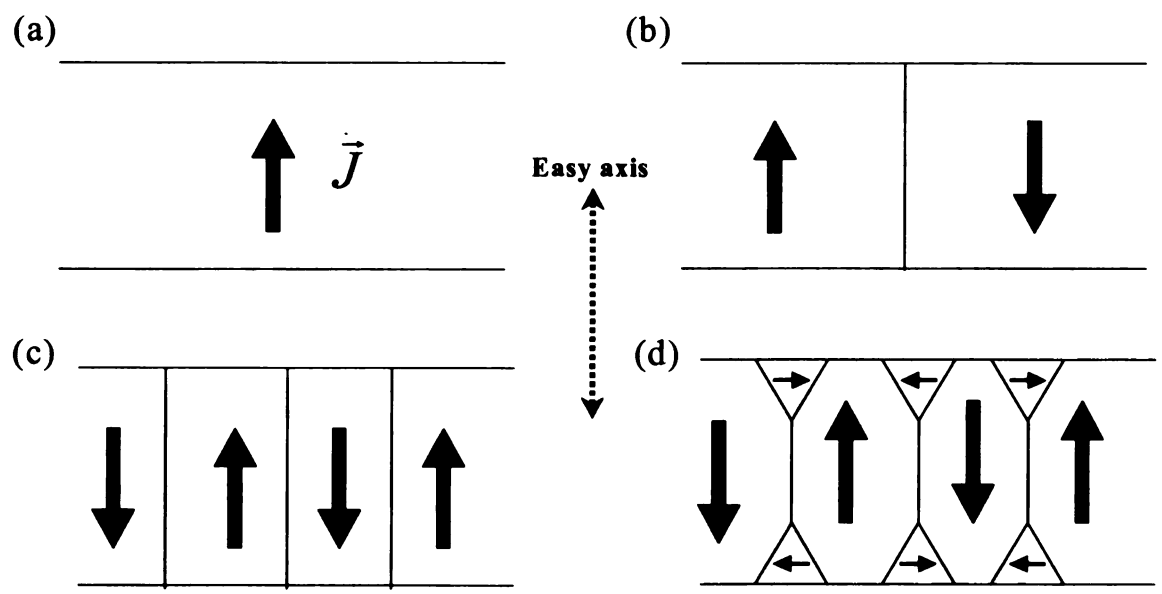

Fig. 1. 8. a) Thin film domain configuration after saturation, with the subsequent reduction to approximately zero field. b) and c) Adding oppositely magnetized domains reduces the magnetostatic energy. d) Formation of triangular closure domains at the edges of the film with magnetization at 90° to the original domains reduces the magnetostatic energy.

When no domains occur at the edges and no wall is present in the film, a wall must first be nucleated somewhere before magnetization change can occur via wall motion. Closure domains at the edges of a film play an important role as nuclei for such walls.

1.3.2 Type of Domain Walls in Unconstrained Thin Films

Shape anisotropy is very pronounced in a thin film due to its extreme thinness compared to the other two linear dimensions. As consequence, the energies and widths of domain walls in thin films are quite different from those in bulk materials. Consider a film of thickness t (along y) and infinite extent in the x-z plane, with easy axis along z, as shown in Fig.1.9. A domain wall of width D, whose plane is perpendicular to x, is placed in this film and magnetizations on either side of the wall are antiparallel and along z. If t > D the sample is essentially three dimensional, and a "Bloch wall" occurs where the magnetization rotates by 180° in the y-z plane within the wall[56]. as shown in Fig1.9 (a). (Bloch walls have no poles inside the wall.) As t $\rightarrow$ D, the Bloch wall will generates significant magnetic pole density on the two opposite surfaces of the film, giving rise to stray fields. Therefore, the magnetostatic energy cannot be a priori neglected. The magnetostatic energy associated with these stray fields plays an important role in the determination of the wall type

Néel demonstrated in an approximate calculation that in a very thin film the energy can be minimized by having the component of the magnetization normal to the surfaces of the film vanish. Thus, the spins within the domain wall rotate in the plane of

the film, x-z in Fig1.9 (b). Because the magnetization along x inside the wall is not zero, magnetic poles are present. These domain walls are called "Néel walls"[57].

There exist other types of domain walls which are intermediate states between these two ideal cases, the well-known Néel and Bloch walls; more information about them can be found elsewhere[58].

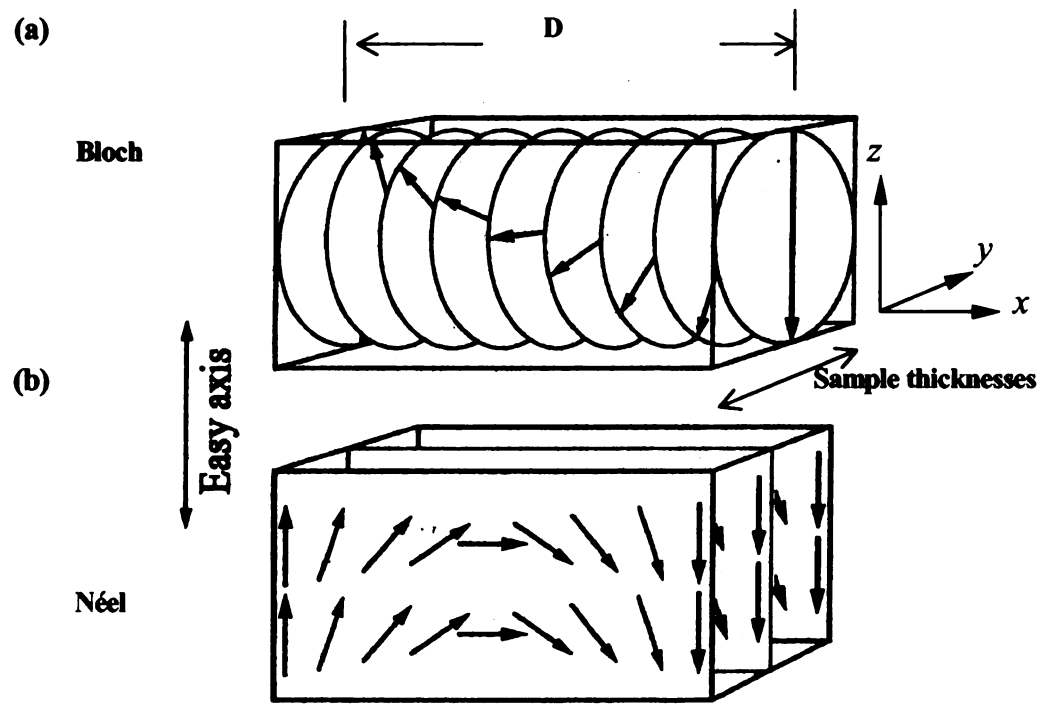

Fig. 1. 9. Two domain wall configurations in a film of thickness t, infinite extent in x-z plane, and easy axis along z: a) Bloch wall b) Néel wall.

As a simple example to establish what parameters define a DW of width, D, consider the determination of a Bloch wall width in an infinite perfect crystal by minimization of DW energy in the semiclassical treatment. The magnetic moments are treated as spins that in turn are considered as classical vectors, whose directions change gradually. The reason for this gradual change is that the exchange energy is lower when

the change is distributed over many atomic planes instead of discontinuously. Of course, the anisotropy energy of the crystal is increased due to the fact that the spins within the wall must by necessity point in directions other than that of the easy axis. A crystal with uniaxial anisotropy, whose axis of easy magnetization is as shown in Fig 1.9 (a), has an exchange Hamiltonian and an anisotropy energy density e_k given by :

$$H_{ex} = -2I\sum_{j>i} S_i \cdot S_j \qquad \text{and} \qquad e_k = \frac{1}{D}\int_{-D/2}^{D/2} K_1 \sin^2\phi dx = \frac{K_1}{2} \qquad (1.18)$$

where I is the exchange integral (which is a constant for this case), S_i corresponds to the i^{th} spin, with i, j = 0 to N, K_1 is the first order anisotropy constant and $\phi=\pi x/D$ is the angle between the spin and the easy direction in the plane of the wall. If the change occurs in N equal steps, the wall thickness is D=Na, where a is the lattice constant, and the total energy per unit wall area becomes:

$$E_w = \frac{\pi^2 I S^2}{Na^2} + \frac{K_1}{2} Na \qquad (1.26)$$

Differentiating E_w with respect to N, the domain wall width is easily found as:

$$D = Na = \left(\frac{2\pi^2 I S^2}{K_1 a}\right)^{1/2} = \pi\left(\frac{A_{ex}}{K_1}\right)^{1/2} \qquad (1.27)$$

where $A_{ex} = 2IS^2/a$. If the exchange interaction is stronger, D gets longer; and alternatively, if the crystal anisotropy is stronger, D shortens[56].

In the previous straightforward example, the magnetostatic energy was not included in the energy balance, but in a more realistic case its consideration is crucial for determining the type of wall present in the system. To exemplify this, let us examine the

results by T. Trunk *et al.*[59], who investigated the Bloch to Néel wall transition in a Py film. They directly integrated the Landau Lifshitz Gilbert equation in a three dimensional cartesian lattice, considering that the dimensions of the sample are infinite in two directions but finite perpendicular to the film plane. They also neglected the crystal anisotropy, and only exchange and magnetostatic energies were included in their calculations.

Fig. 1.10 (a) shows that three regimes can be distinguished based upon the thickness dependence of the magnetostatic energy: "Bloch-type walls" when the film thickness is over 35 nm, a transition from "Bloch to Néel walls" as the thickness of the film is decreased between 35 and 30 nm, and "Néel-type walls" for film a under under 30 nm. Trunk *et al.* provided precise values for this energy balance, as the wall transforms from Bloch to Néel below 35 nm, the energy contribution changes from 76% exchange and 24 % magnetostatic to 70% magnetostatic and 30 % exchange, respectively. This means that, when the dipole interaction gets stronger, Néel walls are more likely to occur.

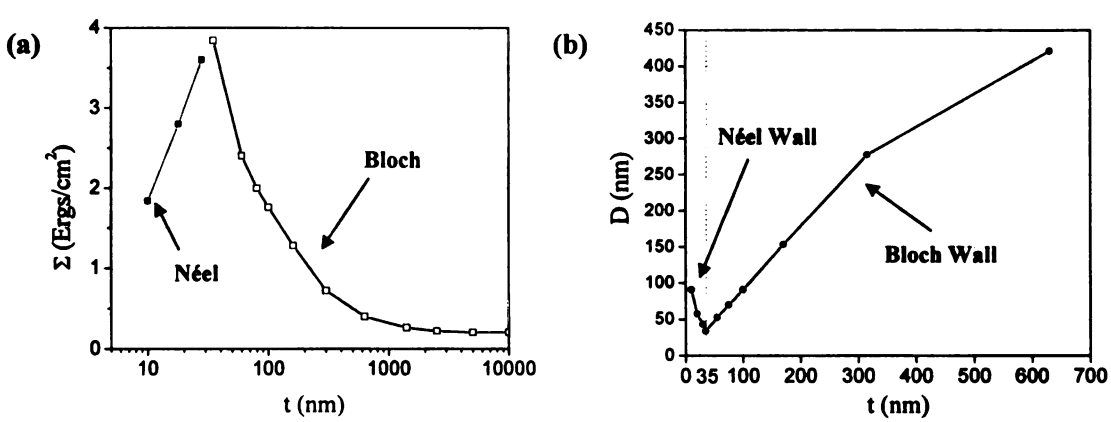

Fig. 1.10. Results presented by Trunk *et. al.*[57] for a Py film. a) Wall energy per unit area as function of film thickness. b) Wall widths in the center of the material, as a function of film thickness.

Fig. 1.10 (b) tell us, that in the center of the material, the Néel wall width increases typically from 35 nm to 100 nm, as the film thickness is reduced. If we define a Py film as thin if its thickness is comparable to the Bloch wall width, Py films under 20 nm can be considered very thin, in which case Néel walls are energetically more likely to occur, with widths up to, at least, 3 times bigger than those of Bloch walls.

1.3.3 Domain Walls in Magnetic Fields and Shape Effects

The previous discussions were based on the influence of the exchange, anisotropy, and magnetostatic energies only. Those DW configurations represent a minimum free energy in the absence of an external field. When an external magnetic field is applied, Zeeman energy also contributes to the energy balance. The angle between the magnetization and the external magnetic field becomes important because the magnetization tends to align along the easy axis. For a perfect single crystal when a field is applied at an angle to the easy axis, the sign of the field component along the easy direction establishes in which direction the walls will move[56]. Analogously, for a polycrystal with strong shape anisotropy, $Q << 1$, see Sect.1.3.1, we can conjecture that the sign of the field component along the shape anisotropy "easy" axis will establish in which direction the walls move.

As just indicated, altering the external shape of a sample can significantly affect the preferred axis of magnetization; and by adjusting these external geometrical parameters, it is possible to trap a DW. In our samples, composed of a long narrow wire as shown in Fig 1.11, the magnetization prefers to align only along the longitudinal axis

of the wire due to the shape anisotropy. A wider area or reservoir at one of the ends allows closure domains to nucleate a DW, a sharp tip on the other end prevents wall nucleation, and a constriction in the middle of the wire ensures wall trapping. After applying a fairly large H along +x, the magnetization of the sample will be pointing to the right in Fig. 1.11. If the field is then lowered until it changes sign (pointing to – x), the DW will first move in the reservoir to accommodate the growth of a favorably oriented domain and then a head-to-head domain wall (see Sect. 1.3.4) will be injected into the narrow wire from the reservoir at the right and eventually will get trapped in the constriction built into the middle of the wire. The presence of the notch creates a potential

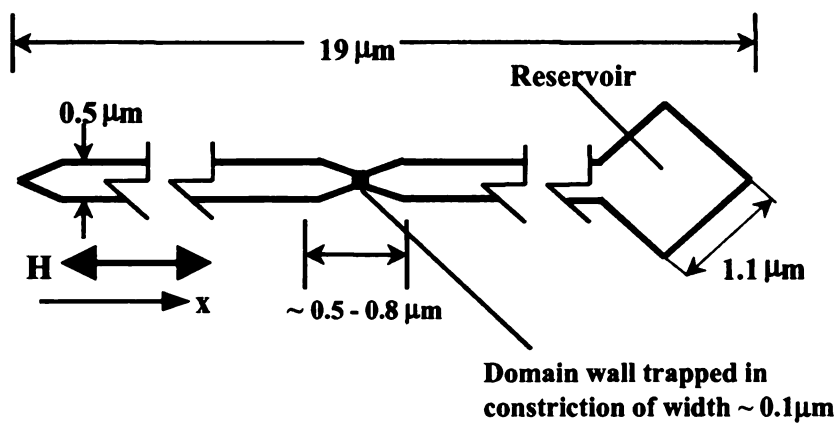

Fig. 1. 11. Top view of a sample used to trap a DW. A constriction placed in the middle traps the wall while it is traveling from one end to the other. A reservoir creates closure domains which nucleate the wall, and a sharp tip on the other side prevents wall nucleation.

barrier that must be overcome for the DW to continue moving. The wall will stay trapped until the applied field lowers the potential barrier sufficiently to drive the wall out of the constriction. The magnetization on the right side of the wall is reversed, and pointing along –x, while the magnetization on the left side is still pointing along +x. As H is lowered further, the wall leaves the notch, and the magnetization of the whole sample will point along –x. If the field is now increased, at low H pointing along +x, a tail-to-tail

domain wall will be injected into the wire from the reservoir and become trapped at the constriction.

1.3.4 Domain Wall Structure in a Ferromagnetic Wire and at a Constriction in Presence of an External Magnetic Field

To interpret the results and understand the mechanisms that rule DW motion in a long nanowire with a central notch, first it is essential to analyze what domain structure can be present in a long narrow F wire without a constriction, and then determine how a constriction alters the dimensions and type of wall present in that geometry.

To understand what kind of DW structure is present in a F thin wire with "no constriction", let us refer to the work done by R. D. Mc Michael *et al.*[60] They presented calculations of head-to-head domain wall structures in magnetic strips of Py, by minimization of the exchange and magnetostatic energies only (and neglecting magnetocrystalline and magnetostrictive anisotropy energies). Two types of head-to-head DW structures can be formed in a long Py strip: "transverse" and "vortex", whose characteristics are illustrated in Fig. 1.12 (a) and (b). A phase diagram was also proposed, which exhibits under what dimensions these two types of structures exist, see Fig. 1.12 (c).

In Fig 1.12 (c), points A and B represent 500-nm-wide Py films of two different thicknesses, $t_A \sim 5$ nm and $t_B \sim 20$ nm. As we will see in details in Chap. 2, these are the dimensions of the Py layers of our samples. We can infer that only a "transverse" wall can be present in our thinner Py films, but a "vortex-type" wall might be present in our

thicker Py layer. However, in the constriction region of the thicker Py layer, the lower effective strip width might cause a transverse wall to form, as inferred from point C in Fig. 1.12 (c).

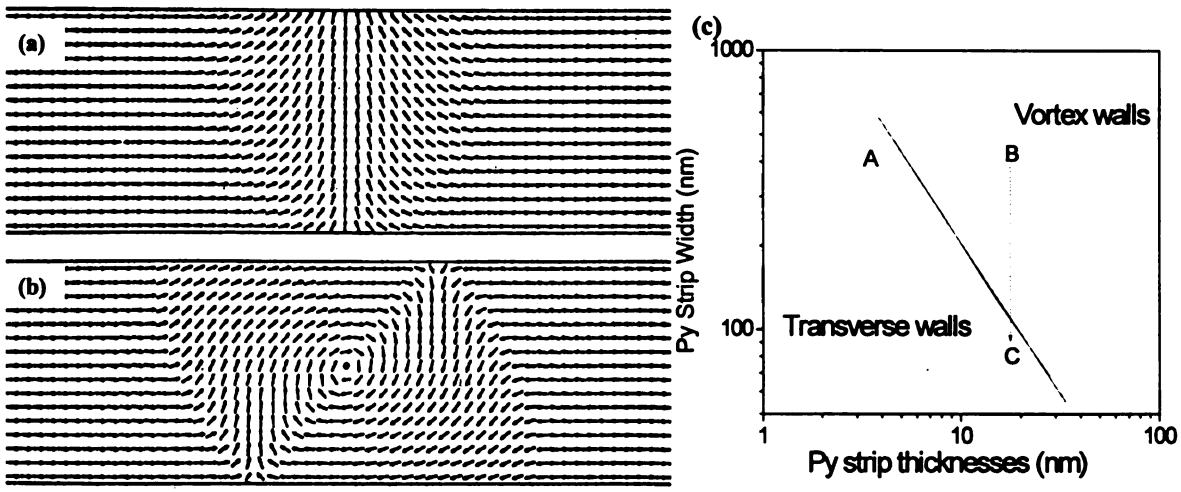

Fig.1.12. Results presented by Mc Michael *et al.* a) "Transverse" domain structure for a head-to-head wall calculated for a 2-nm-thick, 250-nm-wide Py strip. b) "Vortex" domain structure calculated for a 32 nm thick, 250m nm wide Py strip. c) Phase diagram of head-to-head domain structures. A and B points represent our samples, 500-nm-width Py films of two different thicknesses, t_A~5nm and t_B~20 nm. C represents the constriction region, width ~100nm, for the thicker Py layer.

If a constriction is now placed somewhere in these type of wires, the dimensions of the strips will vary locally, and the drastic changes in the shape anisotropy will induce variations of the magnetostatic energy. A treatment for wall characterization in these kinds of geometries was developed by Bruno[61], who theoretically studied a constrained wall in a notch separating two wider ultrathin film regions. In this work the magnetizations of these two regions do not have the same structures as those studied by Mc Michael *et al.* In Bruno's work the magnetizations are antiparallel (at 180°), but they are not aligned as a head-to-head (or tail-to-tail) arrangement. Bruno pointed out that the magnetic wall will tend to localize near the constriction to minimize its energy. When the cross section of the constriction is much smaller than that of the wider region, the

structure becomes almost independent of the material parameters, such as exchange stiffness, and anisotropy constant. Instead the structure is determined by "the geometry of the constriction". The wall energy consists mostly of exchange energy. Thus, he argues that a geometrically constrained magnetic wall constitutes a new kind of magnetic wall, in addition to the well known Bloch and Néel walls. The width of a geometrically constrained magnetic walls is essentially given by the "length of the constriction".

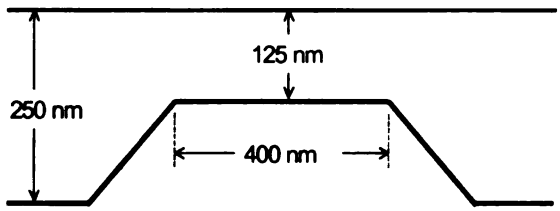

Fig. 1.13. Geometry used by Mc Michael *et al.* to simulate domain wall motion in a 5nm thick Py layer.

The most relevant calculation to the geometry used in this work was done by Mc Michael *et al.*[62] who simulated DW trapping for 5-nm-thick Py wire with a central trapezoidal constriction that opens at 45°, see Fig 1.13. The wire is considered to have semi-infinite ends. Calculations were done using a micromagnetic model, OOMMF, developed at NIST, which is based on the Landau-Lifshitz equation. The model includes effects of the exchange energy (characterized by the exchange stiffness constant), the magnetostatic energy (characterized by the spontaneous magnetization), and applied field energy. The magnetization is assumed to be uniform across the thickness of the film to allow the use of a two-dimensional grid. The spins are free to rotate in three dimensions, but the large magnetostatic energy required to tilt the spins out of the plane results in predominantly in-plane spin configurations. They found that there exist three configurations: one unstable, with the DW in the central region, and two stable, with the DW at either end of the trap, see Fig.1.14. In the unstable configuration the spins along the lower edge of the center region form a 180° wall. For the stable

configurations, when the wall sits at either corner, the magnetization only turns by 135°. This later situation causes a reduction of exchange energy of the domain wall, which stabilizes the wall at the ends of the constriction. Note that for all three configurations the wall has a magnetization that is predominately perpendicular to x ("transverse" DW).

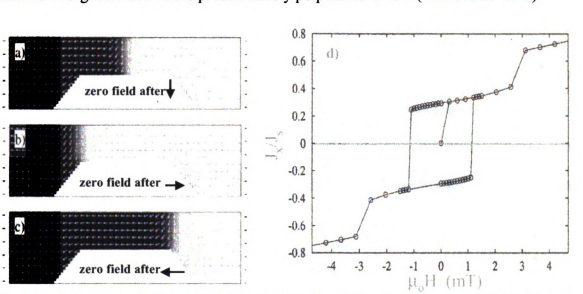

Fig. 1.14. Calculations by Mc Michael *et al.* for spin configurations at zero applied field. a) Unstable state after application of H in the –y direction. b) and c) Stable configurations after application of H in the +x and –x directions, respectively. d) A hysteresis loop for a domain wall trapped in the constriction. The switching field for moving the domain wall from one end of the notch the other is 1.1 mT, and the domain wall is pushed out of the constriction at H = 3.2mT. Note the linear behavior of the magnetization vs. H while the wall is trapped.

Fig. 1.14 (d) shows the hysteresis loop while a wall is trapped in the constriction. The switching field for the domain wall while it is trapped in the notch is 1.1 mT, and the domain wall is pushed out of the constriction at H = 3.2 mT. The magnetization has a linear behavior as a function of the magnetic field while the wall is trapped.

In this simulation DW widths range between ~ 150 nm and ~ 250 nm. This means that the DW width is basically bounded by the wire and constriction widths.

Mc Michael's simulations suggest that only Néel walls are likely to form in constrictions placed in "single" thin Py strips of width t_{Py}. However, when the width of

the constriction $w_{Py} \rightarrow t_{Py}$, we need to be careful because the film might no longer be considered a thin film locally. In this limit, the wall will probably differ from a pure Néel wall. That is in agreement to what is claimed by Bruno, who believes that walls at constrictions are a transitional stage between pure Bloch and Néel walls. This could be the case of the thicker Py layer of our samples.

Combining some of the results by Mc Michael and Bruno, it is possible to estimate the width of the wall present at the constriction of our samples, see Fig. 1.11. A lower DW-width bound would be defined by the width of the constriction ~ 50 nm - 100 nm, and a upper DW-width bound would be determine by some value between the wire width and constriction length ~ 600nm.

Single F-layer systems are easier to analyze than double F-layer systems. As we will see in Sect.1.3.5, extra factors intrinsic to F coupling make the determination of trapped DW structure more complicated in double F-layer systems.

1.3.5 Double F Films

Magnetic double films consist of two F layers separated by a N interlayer. Such sandwich structures must be distinguished from strongly coupled systems, such as F films directly coupled to hard ferromagnetic or antiferromagnetic substrates. When the N interlayer in very thin, typically less than 5 nm, *quantum mechanical exchange* rules the coupling between the F layers. If the N layer is thick enough, a weaker coupling dominates, called *orange peel effect*. This favors the parallel orientation of the two F

layers, and it occurs when the N interlayer is thin compared to the corrugations in the F/N interfaces, see Fig.1.15 (a). If the N layer is free of pinholes and typically much thicker than 10 nm (depending on the type and perfection of the N layer), the F films have no local coupling between the magnetization directions in the two layers. However, if a shape effect makes the thickness and width of the F layers comparable, then the presence of magnetic free poles at the layer edges can alter the stray field and therefore induce coupling between F layers. See Fig. 1.15.(b).

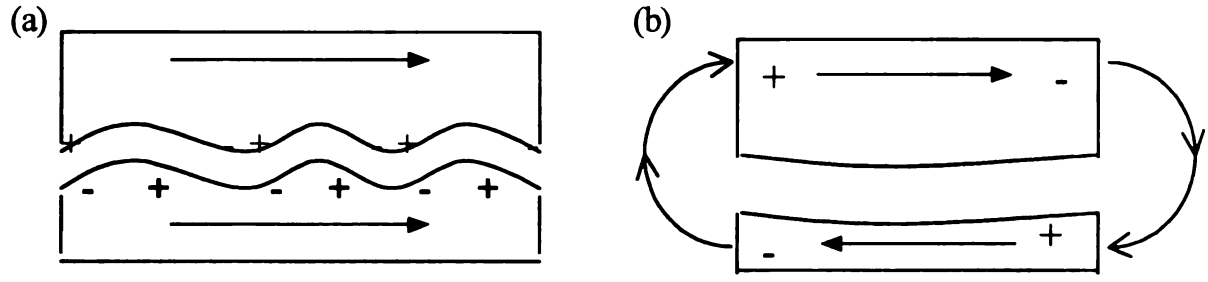

Fig. 1.15. a) Orange peel effect may lead to ferromagnetic coupling. It occurs if the interlayer is thin compared to the corrugations in the magnetic films. b) Free poles at the edge of the F layers may alter the stray field and induce antiferromagnetic coupling between F layers when the thickness of the F layers are comparable to their lateral dimensions.

If the double F layer is in the form of a long wire (with a ~ 10-nm-thick N interlayer), the magnetizations tend to align along the wire axis due to the strong shape anisotropy, and no magnetic poles appear along the edges of the wire, essentially reducing the possible coupling between the F layers to almost zero. However, placing a constriction, as shown in Fig.1.11, introduces a new shape anisotropy which can induce pole formation. These extra magnetic poles affect the magnetostatic energy mainly in their vicinity and, in consequence, induce local coupling between F layers. This local coupling will become stronger as the width of the constriction, w_F, in the F layers is reduced so that $w_F \rightarrow t_F$, where t_F is the thickness of the thicker F layer. In this limit, it is unlikely

that the local magnetizations in the two F layers will be parallel to each other even when no domain wall is present in the constriction. When a wall is trapped in the constriction, this coupling will likely cause the wall to deviate from a pure Néel wall (and this is in addition to the effect produced by $w_F \rightarrow t_F$ on a "single' F layer, described in 1.3.4). For our sample the worst-case scenario is for the thicker Py layer, where $w_{Py} \geq 2.5\ t_{Py}$, and this might imply a relatively small deviation from a pure Néel type wall. However, when no trapped wall is present, the residual coupling may produce observable non-parallel magnetizations in the two F layers.

1.3.6 Wall Displacement Calculation using a Simple Model of a Trapped Head-to-Head Domain Wall

To calculate the wall displacement, Δx, in a notch as H is varied, we have applied a very crude adaptation of Mc Michael *et al.* model[60] to the $F(t_1)/N/F(t_2)$ trilayer system previously presented in Sect. 1.1, where $t_1 < t_2$. The thicker F layer is saturated along +x, and a head-to-head wall, in the thinner F layer, is trapped in a V-shaped constriction, whose geometry is illustrated in Fig. 1.16. Based on the Mc Michael *et al.* calculations shown in Fig 1.12 (a) and 1.14 (a), we approximate the wall as a region of uniform transverse magnetization and width, D, along x . Outside the wall, we assume that the uniform magnetization J is parallel or antiparallel to x, as shown in Fig.1.17.

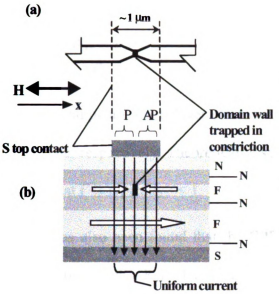

Fig. 1.16. As a wall moves past the top measuring contact, the resistance changes in proportion to the location of the wall. Antiparallel-state resistance > parallel-state resistance.

We consider that after the system is saturated along +x, H is reduced until the wall is trapped. Initially, the wall of width D_o and in-plane area A_W^o, is placed at the center of the constriction, x = 0, within the CPP-current region of area A. The in-plane areas for the parallel state, A_P, and the antiparallel state, A_{AP}, are equal for $\Delta x = 0$. As H is decreased, the wall moves toward the left (along −x), causing A_P to reduce and A_{AP} to increase. At some value of H the DW leaves the notch. The wall displacement Δx was computed for two cases: i) as the wall moves, the DW width is constant, $D = D_o$, and the DW area, A_W, changes; and ii) as the wall moves, D varies and the DW area is constant, $A_W = A_W^o$.

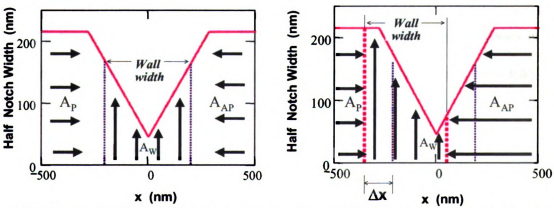

Fig. 1.17. Configuration of our model to calculate the wall displacement, Δx, of a head-to-head wall within a V shaped constriction. Arrows mean magnetization direction. A_{AP}, A_P, and A_W are the areas of the antiparallel region, the parallel region and the wall, respectively, where the CPP current flows.

First let us define the following unitless parameter:

$$\Gamma = \frac{\rho_{AP} - \rho_P}{\rho_P} \tag{1.29}$$

where ρ_{AP} and ρ_P are the trilayer effective total resistivities of the antiparallel state and parallel state, respectively. Theoretically, see Table 1.2, and experimentally, see Chap. 3, we know that Γ is typically << 1.

It has also been found that the CPP resistance of a $F(t_1)/N/F(t_2)$ trilayer system follows $R(\alpha) \cong (R_{AP}-R_p)\ (1-\cos^2(\alpha/2)) + R_P$, where α is the angle between the magnetizations of the F layers.[63] Thus for $\alpha = 90°$ where $\vec{J}_W \perp \vec{J}_P$, we find:

$$\frac{\rho_W - \rho_P}{\rho_P} = \frac{1}{2}\Gamma \tag{1.30}$$

Since the current flows perpendicular to the plane of the sample, the contribution to the total CPP resistance, R_{CPP}, from each part of the notch, as shown in Fig 1.17, is the sum of resistances in parallel, as follows:

$$\frac{t_t}{R_{CPP}} = t_t\left(\frac{1}{R_{AP}} + \frac{1}{R_P} + \frac{1}{R_W}\right) = \frac{A}{\rho_{CPP}} = \frac{A_P}{\rho_P} + \frac{A_{AP}}{\rho_{AP}} + \frac{A_W}{\rho_W} \tag{1.31}$$

where t_t is the total trilayer thickness, R_{AP} and R_P are the resistance contributions of the parallel and antiparallel states within the notch, R_w is the wall resistance contribution, and ρ_{CPP} is the total effective CPP resistivity of the trilayer system.

Using Eqs. 1.29 and 1.30 into 1.31, we obtain:

$$\frac{A}{\rho_{CPP}} = \frac{1}{\rho_P}\left[A_P + \frac{A_{AP}}{(1+\Gamma)} + \frac{A_W}{(1+\frac{1}{2}\Gamma)}\right] \tag{1.32}$$

Using the fact that $\Gamma << 1$ (to neglect second order terms in Γ) and the condition that $A = A_{AP} + A_P + A_W$, Eq. 1.32 can be transform into Eq. 1.33.

$$\rho_{CPP} \equiv \rho_P [1 + \Gamma (1 - \frac{A_P + \frac{A_W}{2}}{A})] \tag{1.33}$$

From Eq. 1.33 we can define R_{norm}, which is a normalized resistance :

$$R_{norm}(\Delta x) = \frac{\rho_{CPP} - \rho_P}{\rho_{AP} - \rho_P} = 1 - \frac{A_P + \frac{A_W}{2}}{A} \tag{1.34}$$

R_{norm} is associated with the wall position in the notch, because each term of Eq. 1.34 is a function of Δx, except for A (and A_W when assumed to be constant). When the wall is centered in the notch, $\Delta x = 0$, and $R_{norm}(\Delta x = 0) = R^{\circ}_{norm}$ is a minimum. When the wall is about to leave the constriction, $\Delta x = \Delta x_{max}$, and $R_{norm}(\Delta x_{max}) = R^{max}_{norm}$ is a maximum. Given the difference between the normalized resistances of these two states:

$$\delta R_{norm} = R^{max}_{norm} - R^{0}_{norm} = \frac{1}{A} [A^{o}_{P} - A^{max}_{P} + \frac{A^{o}_{W} - A^{max}_{W}}{2}] \tag{1.35}$$

and subject to the constraint that δR_{norm} is fixed, we can determine Δx_{max}. We obtain the roots of Eq. 1.35 for different values of the initial D_o (using either of the mentioned constraints: $D = D_o$ and variable A_W, or constant $A_W = A^{\circ}_W$ and variable D).

As an example, let us assume that $\delta R_{norm} \sim 0.1$, which is a representative experimental value, as we will discuss in Chap. 3. A Mathcad program was used to find the roots of Eq 1.35, and the results are presented in Fig. 1.18. The Δx_{max} vs. D_o curves, for the two types of constraints, have similar behaviors. This means that for an initial D_o ~ 50 nm - 100 nm, "both curves" show that the wall must move ~ 150 nm inside the

notch to keep $\delta R_{norm} \sim 0.1$, and for an initial $D_o \sim 600$ nm the wall must shift ~ 70 nm, see Sect. 1.3.4.

A better analysis would be to solve the micromagnetics problem for the V-shaped notch in a finite H using OOMMF and then use the CPP transport analysis to predict δR_{norm}. Such as analysis has not yet been done.

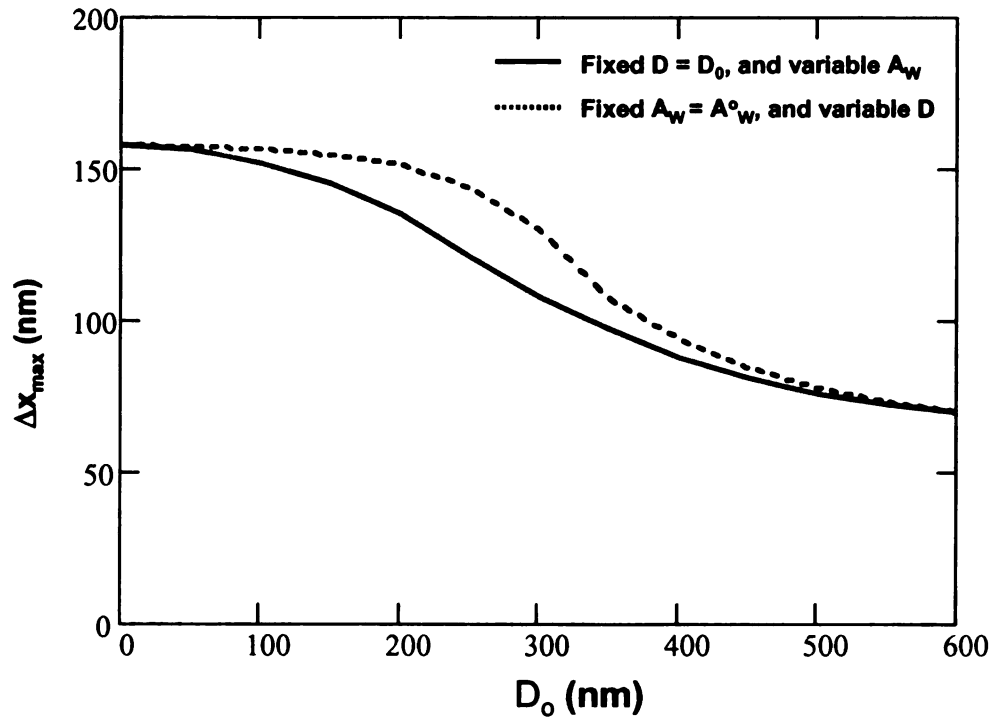

Fig. 1.18 Maximum wall displacement within the constriction as a function of the initial wall width D. Curves for a fixed D and for a fixed wall area A_W do not exhibit large differences.

REFERENCES

[1] Cullity, *Introduction to Magnetic Materials*, **4.1**, 117 Addison Wesley Publishing (1972).

[2] A. Humbert and R. Schäfer, *Magnetic Doman*, **1**, 1, Springer, Berlin and NY (1998).

[3] R. D. Slater, *Perpendicular Giant Magnetoresistance in Thin Films with Microfabricated Superconduting Top Contacts,* Dep. of Phys., MSU (2001).

[4] T. Ono, H. Miyajima, K.Shigeto and T. Shinjo. *Appl. Phy. Lett.* **72**, 1116 (1998).

[5] T. Ono, Y. Ooka, S. Kasai, H. Miyajima, N. Nakatani, N. Hayashi, K.Shigeto, K. Mibu and T. Shinjo. *Mater. Sci. Eng. B* **84**, 126 (2001).

[6] J. Bass, W. P Pratt, and P. A. Schroeder, *Com. Cond. Mat. Phys.* **18**, 223 (1998).

[7] P. M. Levy, Solid State Physics, H. Ehrenreich and Turnbull, Eds., *Academic Press*, NY, **47**, 367 (1994).

[8] M.A.M. Gijs and G.E.W. Bauer, *Adv. in Phys.* **46**, 285 (1997).

[9] J. Bass and W. Pratt Jr., *J. Magn. Magn. Mat.* **200**, 274 (1999).

[10] Shang-Fan Lee, PhD. Dissertation, Michigan State University, (1994).

[11] Qing Yang, PhD. Dissertation, Michigan State University, (1995).

[12] R. Danneau, P. Warin, J. P. Attané, I. Petej, C. Beigné, C. Fermon, O. Klien, A. Marty, F. Ott, Y. Samson, and M. Viret. *Phys Rev. Lett.* **88**, 157201 (1988).

[13] A D. Kent, U. Rüdiger, J. Yu, and S. S. P. Parkin , *J. Phys: Condens. Matter 13*, R 461-R 488, (2001).

[14] U. Rüdiger, J. Yu, L. Thomas, S. S. P. Parkin, and A. D. Kent, *Phys Rev. **B** **59**,* 11914 (1988).

[15] M.N. Baibich et al., *Phys Rev. Lett.* **61**, 2472 (1988).

[16] G. Binash et al., *Phys Rev. B* **39**, 4828 (1989).

[17] J. Ph. Anserment, *J. Phys. ,Condens. Mat.* **10**, 223 (1998).

[18] Gary A Prinz, *Phys. Today* **48**, 58 (1995).

[19] Gary A Prinz, *Science* **282**, 1660 (1998).

[20] P. Grunberg, R. Schreiber, Y. Pang, M. B. Brodsky, and H. Sowers, *Phys. Rev. Lett.* **57**, 2442 (1986).

[21] D. H. Mosca, F. Petroff, A. Fert, P. A. Schroeder, W. P. Pratt Jr., R. Loloee, and S. Lequien, *J. Magn. Magn. Mat.* **4**, L1 (1991).

[22] S.S Parkin, N. More, and K.P. Roche, *Phys. Rev. Lett.* **64**, 2304 (1990).

[23] S.S Parkin, R. Bhadra, and K.P. Roche, *Phys. Rev. Lett.* **66**, 2152 (1991).

[24] M.D. Stiles, *J. Magn. Magn. Mat.* **200**, 322 (1999).

[25] S. Urazhdin, N.O. Birge , W.P. Pratt, J. Bass, *Phys. Rev. Lett* **91**, 146803 (2003).

[26] J. Slonczewski, *J. Magn. Magn. Mat.* **159**, L1 (1996).

[27] L. Berger, *Phys. Rev. B* **54**, 9353 (1996).

[28] M. Tsoi, A. G. M. Jansen, J. Bass, W. -C. Chiang, M Seck, V. Tsoi, and P. Wyder, *Phys. Rev. Letter.* **80**, 4281 (1998).

[29] M. Tsoi *et al.*, *Nature* (London) **406**, 6791 (2000).

[30] E. B. Myers, D. C. Ralph, J. A. Katine, R. N. Louie, and R. A. Buhrman, *Science* **285**, 867 (1999).

[31] J. Grollier, V. Cros, A. Hamzic, J. M. George, H. Jaffres, A. Fert, G. Faini, J. Ben Youssef, and H. Le Gall, *Appl. Phys. Lett.* **78**, 3663 (2001).

[32] K. Bussman, G. A. Prinz, R. Bass, J. -G Zhu, *Appl. Phys. Lett.* **78**, 2029 (2001).

[33] W.P.Pratt Jr.,S.F. Lee, J.M Slaughter, R. Loloee, P.A. Schroeder, and J. Bass, *Phys. Rev. Lett.* **66**, 3060 (1991).

[34] S. Zhang, and P. M. Levy, *J. Appl. Phys.* **69**, 4786 (1991).

[35] S. F. Lee et al., *J. Magn. Magn. Mat.* **118**, L1 (1993).

[36] K. Xia, P. J. Kelle, G. E. W. Bauer, I. Turkek, J. Kudrnovsky, and V. Drchal, *Phys. Rev. B* **63**, 64407 (2001).

[37] K. Eid, *Studies of Current Perpendicular to Plane Magnetoresistance,* **3**, Dept. of Phys. MSU (2002).

[38] T. Valet and A. Fert, *Phys. Rev. B* **48**, 7099 (1993).

[39] P.C. van Son, H. van Kempen, and P. Wyder, *Phy Rev. Lett.* **58**, 2271 (1987).

[40] M. Jhonson and R. H. Silsbee, *Phys. Rev. B* **37**, 5312 (1988).

[41] Q. Yang, P Holoday, S. –F. Lee, L.L. Henry, R. Loloee, P. A. Schroeder, W. P. Pratt Jr., and J. Bass, *Phys. Rev. Lett.* **72**, 3274 (1994).

[42] A. Fert and S. F. Lee, *Phys. Rev. B* **53**, 6554 (1996).

[43] W. P. Pratt Jr., S. -F. Lee,Q. Yang, P. Holody, R. Loloee, P. A. Schroeder and J. Bass, *J. Appl. Phys* **73**, 5326 (1993).

[44] S. F. Lee, W. P. Pratt Jr., Q. Yang, P. Holody, R. Loloee, P. A. Schroeder and J. Bass, *J. Magn. Magn. Mat.* **118**, L1 (1993).

[45] J. Nougues and I. K. Schuller, *J. Magn. Magn. Mat.* **192**, 203 (1999).

[46] B. Dieny, V. Sperious, S. Metin, S.S.P. Parkin, B. A. Gurney, P. Baumgart, and D. R. Wilhoit, *J. Appl. Phys.* **69**, 4774 (1991).

[47] K. Eid, H. Kurt, W. P. Pratt Jr., and J. Bass, *submitted to Phys. Rev. Lett.*

[48] W.P. Pratt Jr, S. D. Steenwyk, S. Y. Hsu, W. –C. Chiang, A. C. Schaefer, R. Loloee, and J. Bass, *IEEE Tran. Magn.* **5**, 3505 (1997).

[49] K. Eid, *Studies of Current Perpendicular to Plane Magnetoresistance,* Dept. of Phys. MSU (2002).

[50] Personal communication.

[51] A. Humbert and R. Schäfer, *Magnetic Domanin*, **3.2** ,108, Springer, Berlin and NY (1998).

[52] Hong Geng. *Structural Studies of GMR Magnetic Multilayers and Spin-Valves grown by DC Sputtering*, 85-95, Dep. of Chem. Eng. and Mat Sci. MSU (2002).

[53] R. Loloee, W. P. Pratt Jr., and M.A. Crimp, *Phil Mag A* **81**, 261 (2001).

[54] R. Loloee, and M.A. Crimp, *J. App. Phy.* **92**, 4541, (2002).

[55] R. Loloee, S. Urazhdin,W. P. Pratt Jr., H. Geng and M.A. Crimp, *Appl. Phys. Lett.* **84**, 2364 (2004).

[56] A. Humbert and R. Schäfer, *Magnetic Domanin*, **3.6**, 215, Springer, Berlin and NY (1998).

[57] R.F Soohoo, *Magnetic thin Films*, **4.1**, 39, Harper &Row, NY (1965).

[58] R.F Soohoo, *Magnetic thin Films*, **4**, 37, Harper &Row, NY (1965).

[59] T. Trunk, M. Redjdal,A. Kákay, M. F. Ruane and F. B. Humphrey, *J. Appl. Phys.* **89**, 7606 (2001).

[60] R. D. Mc Michael and M. J. Donahue, *IEEE Tran. Magn.* **33**, 4167 (1997).

[61] P. Bruno, *Phy. Rev. Lett.* **83**, 2425 (1999).

[62] R.D. Mc Michael, J.Eicke, M.J. Donahue, and D.G. Porter, *J. Appl. Phys.* **87**, 7058 (2000).

[63] Personal communication.

CHAPTER 2

Experimental Methods

2.1 Introduction

Studying the behavior of a domain wall in a localized region of a ferromagnetic layer requires high resolution measurements, which can only be provided by sensitive techniques. Given its enhanced response to small motions of the wall, our current perpendicular to plane, CPP, giant magnetoresistance, GMR, technique is an effective method for detecting the presence and motion of a trapped wall. However, high quality samples are needed, requiring very precise fabrication processes. In this chapter the work done to optimize this new method, along with a summary of procedures to make and measure good quality nano-fabricated spin-valve, SV, samples, are presented.

2.2 Sample Preparation

The overall sample fabrication can be summarized as follows: first, Au leads were deposited onto a Si substrate and shaped using lithography. The dimensions of the Au leads were gradually increased in the transition from the microscopic contacts of the

nanowires, to the macroscopic contact pads, that are used for external connections. After that, a Nb/Cu/Py/Cu/Py/Cu/Au multilayer was sputter deposited onto the substrate and patterned via lift off into ~30 μm × ~60 μm rectangles that make contact with some of the Au leads. (Py = "Permalloy" = $Ni_{84}Fe_{16}$.) Next e-beam lithography, evaporation of a 300-nm-thick Al layer, and lift-off were used to define Al masks for subsequent ion milling to form the 'wire' and its notch. After ion milling through the thick Py layer, a planar layer of SiO was evaporated to insulate the top and bottom contacts. To remove possible backscattered particle wall formation on both side of the Al masks, ion milling at small angle was also done before the Al was removed by a chemical etch. Finally, e-beam lithography, sputter deposition and lift-off were used to produce a Nb or Au top contact. The procedure was mainly accomplished in a class 1000-100 clean room, and its result is summarized in Fig. 2.1.

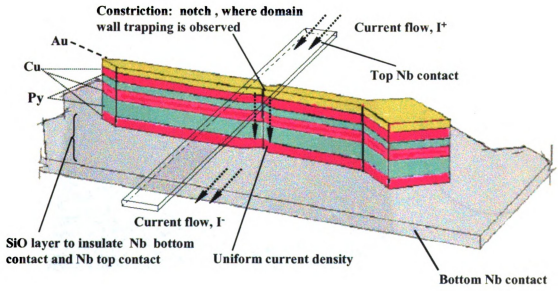

Fig. 2. 1. Perspective view of a sample, illustrating the actual geometry. The superconducting top and bottom Nb contacts, at 4.2 K, ensure a uniform CPP current density through the sample. For some samples Au top contacts were used instead. Note that the vertical is exaggerated.

2.2.1 Design of a Mask for Photolithographic Patterning of Au Electrical Leads

Sample preparation began by cleaning the Si (100) wafers. The wafers were first submerged in Alconox®, and placed in an ultrasonic cleaner for 15 minutes. After rinsing in deionized water, the substrates were immersed in acetone, and placed again in an ultrasonic cleaner for 15 minutes. A final bath of isopropanol alcohol, IPA, was used to accelerate and improve the drying process. The wafers were visually inspected using a *Olympus BX60* optical microscope between 20 X and 100X. If non removable defects, such scratches, were present, the wafer was discarded. Wafers, which passed inspection, were placed in IPA and the preparation procedure was continued.

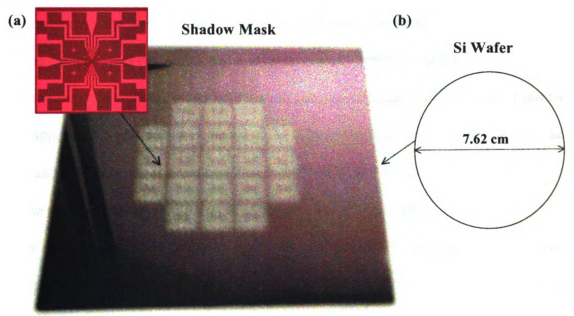

Fig. 2. 2. a) Picture of the shadow mask used to make the Au leads prior to the deposition of the multilayer onto the Si substrates. This shadow mask provided 24 (1.27 cm x 1.27 cm) individual substrates from each Si wafer. b) Sketch of a Si wafer, which is positioned under the shadow mask during exposure to ultraviolet light.

The photolithographic process was performed using a shadow mask to pattern a photoresist layer before deposition of the Au electrical leads onto the Si wafers. A picture of the design of the shadow mask is shown in Fig 2.2 (a). This mask allows one to obtain up to 24 (1.27 cm x 1.27 cm) substrates from each wafer. The majority of the mask is transparent to ultraviolet light, and the dark chrome regions form features on the substrate by projecting a shadow. In general, a positive radiation-sensitive resist, i.e. photoresists or e-beam resists, has strong chemical bonds (also called cross linked bonds), and when exposed to ultraviolet light or an electron beam, these bonds break down, making the exposed area soluble in developers (acid based chemicals). The portion of resists underneath the mask is still cross-linked and insoluble in developers.

To produce Au leads with smooth edges, a large enough undercut in the resist was required to separate the evaporated (or sputtered) material lying on the top of the photoresist from the portion of the material deposited directly on Si.

The optimum process, which had a success rate of ~ 100 %, is as follows:

1. The sample is positioned and held via vacuum on a Spinner. A large drop of positive Shippley 1805 photoresist is placed using a pipette on the surface of the substrate and spun for 45 seconds at a rate of 4500 r.p.m. Thickness ~ 0.5 μm.
2. The sample is baked for 45 min at 95°C to harden the photoresist.
3. By using a previously designed photo mask fabricated by Photronics, the sample is exposed to ultraviolet radiation of wavelength between 365 nm to 400 nm in selected areas. Exposure of the sample was accomplished utilizing mask aligner from *AMB, Inc.*

4. The sample is submerged in Chlorobenzene for 30 second to harden the surface of the non-exposed areas to achieve the desired undercut.
5. The remaining Chlorobenzene is removed from the sample surface by rinsing the samples in deionized running water for 20 seconds.
6. Each sample is immersed in a bath of *Shippley 452* developer to remove the exposed photoresist and then rinsed in deionized water for 20 seconds.

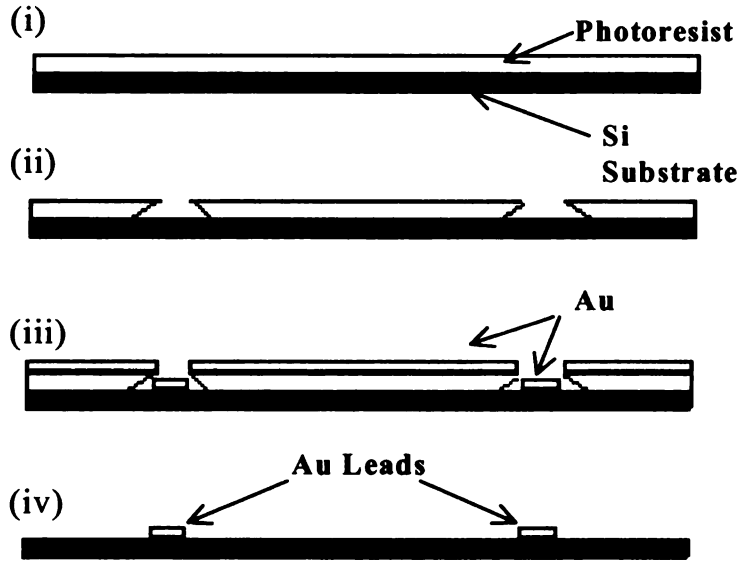

Fig. 2.3. Cartoon of the Au leads deposition procedure. This technique can be used for any process involving evaporation or sputtering. i) Photoresist over a Si substrate. ii) Developed patterned photoresist after exposure to light. iii) Evaporated Au on a Si substrate and on the photoresist. iv) Au leads on a Si substrate after lifting-off.

Once the photoresist mask was created, 150 nm thick Au leads were evaporated onto the Si wafers after a previous deposition of 3 nm of Ti to improve the binding of the Au to the substrate. Au has strong bond to Ti, and Ti adheres well on the surface of the Si wafer due to the chemical bond to the naturally-occuring SiO_2. The Ti evaporation rate was ~ 0.04 nm/sec for a current of 3.6 A. The evaporation of Ti and Au took place in an

Edwards-Auto 306 evaporator at approximately 3 x 10^{-7} Torr. Au evaporation rate was 0.3 nm/sec for a current of 2.6 A. To lift-off, each wafer was submerged in acetone at 80 °C for 20 minutes and rinsed with IPA. Fig. 2.3 illustrates the different phases of the Au deposition method. The final geometry of the Au electrical leads is shown Fig 2.4. Note that the central area, surrounded by the ends of the Au leads, is empty for subsequent deposition of the multilayer, and that the Au contact pads are shorted via a Au bridge, to prevent the nano samples from burning out due to static discharge during handling.

On the Au leads another layer of positive Shippley 1805 photoresist was spun for 45 seconds at a rate of 4500 r.p.m., to protect the surface of the wafers, and to keep them clean during cutting. Si wafers were cut using a *Micro Automation Dicing Saw model 1006*, into 24 individual square substrates of 1.27 cm by 1.27 cm, see Fig. 2.4 (a).

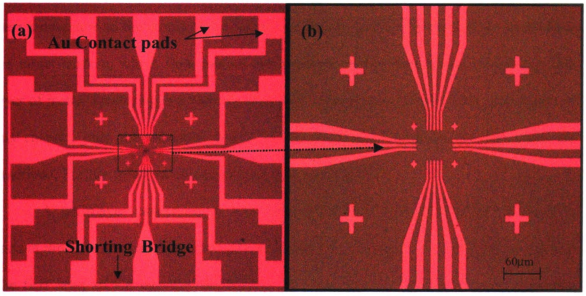

Fig. 2. 4. a) Top view of the patterned Au leads on a single Si substrate of 1.27 cm by 1.27 cm. Note that the Au contact pads are shorted to prohibit burning out of the samples due to static charges. b) Magnification of the central region of the Si substrates; there is an empty area of size 40 μm by 60 μm, surrounded by the Au leads.

With the Au electrical leads in place, the substrates were ready for deposition of the multilayer.

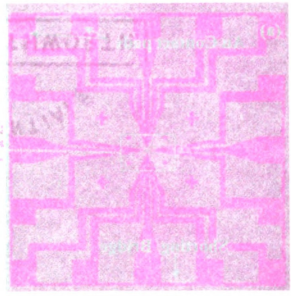

2.2.2 Multilayer Thin Film Preparation via Sputtering

The basic sputtering process involves a large vacuum chamber and a low pressure inert gas atmosphere. Upon applying a high current to a filament (cathode), the heated filament emits electrons that accelerate toward an anode. These accelerating electrons ionize the Ar gas molecules in their paths creating positive ions. The target is located between the anode and cathode, and the whole assembly is coupled to a pair of parallel magnets, that produce a magnetic field that is parallel to the target surface and perpendicular to the cathode-to-anode direction, which localizes the electrons to the region above the target. Applying a negative voltage to the target causes the ions to accelerate toward the target (ion bombardment). During bombardment, the ions transfer their momentum to the atoms of the target and thereby physically eject these atoms from the target surface, which flow toward the substrate where they adhere, creating a thin layer of metal. Sputtering is a versatile process for making multilayer films. In this part of this chapter, only the essential details of the sputtering technique for this work are described. Further information can be obtained elsewhere[1-4].

A multilayer consisting of Nb(100)/Cu(10)/Py(20)/Cu(10)/Py(5)/Cu(5)/Au(15), units in nm, was sputtered onto the central part of the substrates, as illustrated in Fig. 2.5. The first layer of Cu between the bottom Nb layer and the thicker Py layer acts as a buffer layer between the fcc Py and the bcc superconducting Nb. The intermediate layer of Cu is used as a spacer to reduce coupling between Py layers, see Sect. 1.3.5. The last Cu layer provides identical interfaces on both sides of the thin Py layer. The Au layer on the top is to protect the multilayer from oxidation and provides good electrical contact.

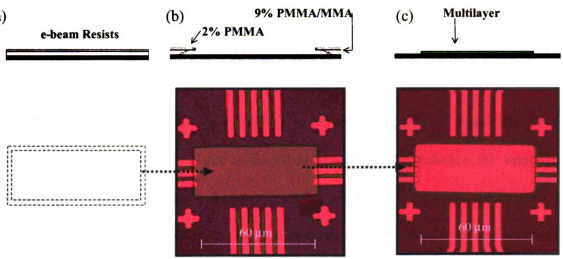

Fig. 2.5. Sputtered multilayer. a) Sketch of the exposed area with different e-beam doses (different size rectangles), to create a bigger undercut. b) Top view of patterned e-beam resist. c) Top view of the actual sputtered multilayer. The upper cartoons show side views of the lithographic process.

Before sputtering the multilayer, positive resist was spun on each Si substrate, and an e-beam resist mask was lithographically built. To obtain each of the e-beam lithographic features, the samples went through the same technique:

1) To create the mask, a layer of 9% Copolymer in Chlorobenzene (Copolymer is Polymethyl methacrylate (PMMA), 495k molecular weight, and 85% methacrylic acid (MAA)) is spun at 3000 r.p.m. onto the sample and baked for 5 min at 160 °C.
2) A second layer of 2% PMMA (in Chlorobenzene) is spun at 4600 r.p.m. and again baked at 160 °C for 30 minutes.

These two layers of resist are used to broaden the undercut in the resists mask after developing as shown in Fig. 2.5 (b). The first layer of 9% Copolymer is more sensitive to secondary electrons coming from the substrate than the 2% PMMA.

3) The features are drawn by exposing the samples to an e-beam in a *JOEL* 840 scanning electron microscope, SEM, at a magnification of 850X, and at a working distance of 25 mm.

4) The samples are developed in a 1:3 methyl isobutyl ketone (MIBK) to IPA mixture, then rinsed in IPA for 10 seconds and dried with N_2 gas.

A rectangular area of 28 μm by 65 μm, as shown in Fig. 2.5 (a) was drawn by e-beam lithography following the above-described technique. To enhance the undercut generated by the bilayer of resist, the samples were subjected to an exposure only on a bigger rectangle (29μm by 66μm) with a dose of approximately 50 $\mu C/cm^2$ and a current of 50 pA. A second exposure of 180 $\mu C/cm^2$ with 50 pA (smaller rectangle) created the actual area for deposition of the multilayer. The center-to-center distance, together with the line spacing of the e-beam, were set to 193.5 Å. The latter parameters are not relevant at this point of the sample preparation, and they were chosen to maximize efficiency. Finally the samples were developed for 40 seconds.

Deposition of the multilayer via sputtering was done following the standard procedures described elsewhere[1-4]. Do note that quartz-crystal film-thickness monitors were used to determine the layer thicknesses. Typical deposition rates were: Au ~ 4.5 Å/s, Py ~ 5.5 Å/s, Cu ~ 9 Å/s, and Nb ~ 6 Å/s at an Ar pressure of 3×10^{-3} Torr. To lift-off, each Si substrate was immersed in acetone at 80 °C for 20 minutes, rinsed with IPA and dried with N_2.

2.2.3 E-beam Lithography to Define the Required Geometry (i.e., Wire with Central Notch) for Domain Wall Trapping

To make the wires for domain wall trapping, a portion of the multilayer is etched by ion milling. An Al mask with the shape of the nanowire is used to shield the portion of the multilayer which will constitute the sample and delimit the region of the multilayer to be etched away. To control the shape of the notch properly, the e-beam lithography used to create the Al mask must be carefully done because the smallest transverse dimension of the constrictions is close to the resolution of the method, which is given by a spot size of ~ 25 nm diameter.

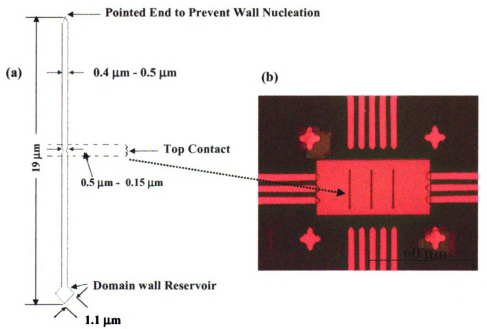

Fig. 2.6. a) Sketch of a multilayer nanowire showing its typical shape and dimensions. The reservoir helps nucleate the domain wall. b) Top view of the center of a substrate, showing the wires drawn in the e-beam resist.

The shape and dimensions of the nanowires, see Fig. 2.6 (a), were based on the Japanese group's work[5-8], where trapping of a domain wall in a notch was shown using current in plane MR geometry. They showed that attaching a reservoir pad at the end of the nanowire causes a drastic decrease of the switching field associated with the injection of a domain wall from the reservoir pad into the nanowire. They also found that the wire with a diamond-shaped reservoir pad, in comparison to other pad geometries, shows the lowest switching magnetic field at any temperature.

To trap the wall, two types of notch geometries were designed: a well-defined V-shaped notch, and a more elongated U-shaped notch. Fig. 2.7 shows scanning electron microscope, SEM, images of the Al masks used to build these two different constrictions. Their basic difference is given by their shape and dimensions: a V-shaped notch is typically ~ 500 nm long by ~ 50 nm to 100 nm wide in the narrowest region, and a U-shaped notch is ~ 800 nm long by ~ 50 to150 nm wide in the narrowest region.

The e-beam lithographic procedure utilized to make the Al masks followed the technique described in Sect. 2.2.2, see also Fig. 2.8 (a) i-v. The samples were exposed to a single dose for a current of ~12 pA. The center to center distance together with the line spacing of the e-beam were set to 48.5 Å. In this manner, this combination of parameters produced the optimum pattern. One of the main concerns during this process was the control of the developing time, which can vary significantly depending on various factors such as the SEM calibration (the most crucial one). Small variations of the working conditions, i.e., a new SEM filament or temperature oscillations, can alter the final result considerably (even when the rest of the SEM parameters are not changed). To reduce these undesired effects, we increased the exposure dose to 500 $\mu C/cm^2$ so that only a 3-

sec developing time was necessary to obtain quality samples. After developing was done in an ultrasonic bath, a 300 nm layer of Al was evaporated in the *Edwards-Auto306* evaporator at a deposition rate of 0.5 nm/sec, 2.2 A current. When the deposition was finished, the samples were placed in acetone at 80 °C to lift-off the Al not in contact with the multilayer. The remaining Al wires were used as a shield, selecting the areas where ion milling should not occur. Al has a lower ion-milling rate than the rest of the materials of the multilayer, and, in principle, it can be easily removed with a photo developer.

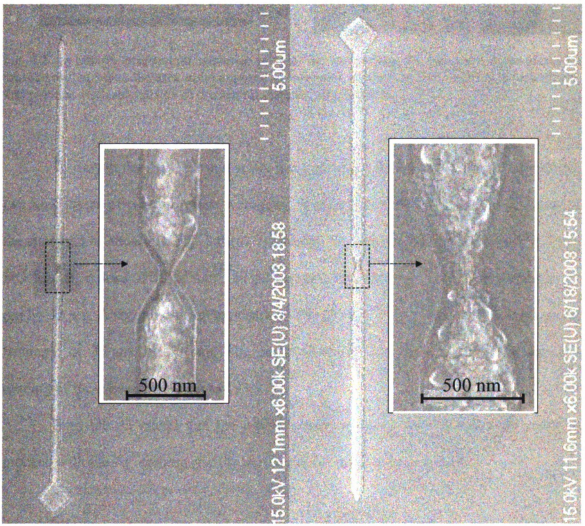

Fig. 2.7. SEM pictures showing 300 nm thick nanowire Al masks on the multilayer. The two typical geometries of the notch are displayed: a) V-shaped notch, and c) U-shaped notch. b) and d) are magnified views of the constriction regions.

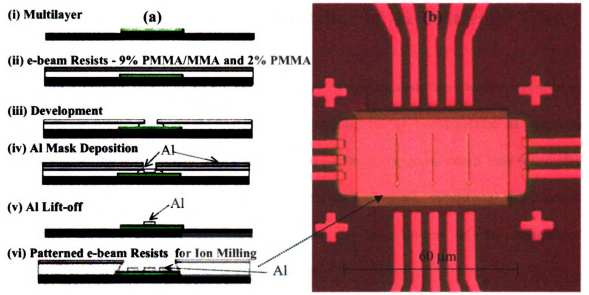

Fig. 2.8. a) Sample preparation sequence prior to Ar^+ ion etching. b) Top view of Al masks on multilayer that select the area to be exposed to ion-beam etching, and of the e-beam resist layer, that protects Au leads outside of the central open rectangular area.

To protect the Au leads and select the area where the insulating layer is deposited, two new layers of e-beam resists were spun to create an open rectangle in the center of the substrate as shown in Fig. 2.8 (a) vi and (b). To enhance the undercut and facilitate SiO lift-off, a dose of 50 $\mu C/cm^2$, 50 pA current, was applied on a bigger rectangle, 37 μm by 52 μm. A second e-beam exposure of 180 $\mu C/cm^2$, 50 pA current, forms the actual rectangle of 35 μm by 50 μm. The center-to-center distance, together with the line spacing of the e-beam, were set to 193.5 Å.

With the Al masks and the e-beam resist in place, the substrates are ready to proceed with the Ar^+ etching and the deposition of SiO planar insulation.

2.2.4 Ion Milling and Planar Insulation of the Patterned Wire

In ion beam etching, an ion beam is directed against a surface, with the objective of removing material from the surface. The etching is the consequence of physical sputtering, which is the result of the momentum exchange between beam ions (normally formed from an inert gas) and the target atoms or molecules. Additional information about ion milling techniques, including particular descriptions of the equipment employed in this work can be obtained elsewhere[3, 9-10].

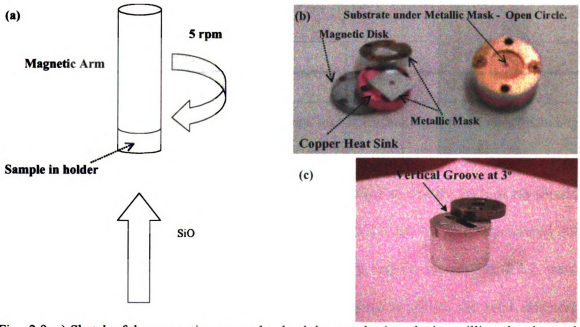

Fig. 2.9. a) Sketch of the magnetic arm used to load the samples into the ion milling chamber and to hold and rotate them during SiO deposition. b) Holders for top ion milling. The sample is localized under a metallic mask with a hole in its center to select the area to be ion milled. c) Cylindrical holders for side ion milling.

Samples to be ion milled were placed in holders consisting of a metallic mask, a copper heat sink, and a magnetic disk, see Fig. 2.9 (b). With the help of a magnetic arm, the holders with the attached samples could be situated in a vacuum chamber either above an evaporation boat for SiO or a 3-cm ion Ar^+ source made by *Commonwealth Scientific*

Corporation[9]. As shown in Fig. 2.9 (a), the holder is inserted into the chamber directly above the SiO boat. For ion milling, the holder is detached in-situ from the magnetic arm and located on a wheel that can rotate so that the holder is placed above the ion gun.

The system was continuously pumped down to 1 x 10^{-7} Torr. Etching was done by ion milling at an Ar pressure of 1 x 10^{-4} Torr, ~ 7 mA current and at 300 V accelerating voltage. Ar gas was bled into the chamber at 3 to 6 sccm. A shutter shielded the samples while the ion gun was started. When the system was ready, the chosen sample was rotated via a wheel over the ion mill, and the shutter was opened. Ion milling rates were obtained from Refs. 3 and 9 and related to the Au ion milling rate provided by the same references, as shown in Table 2.1.

Nb	Cu	Py
0.26	0.65	0.38

Table 2.1. Ratio ion milling rate / Au ion milling rate for Nb, Cu, and Py. Ion mill rates (including Au) were obtained from Refs. 3 and 9.

Each sample was ion milled for a long enough time so that the bottom Nb should be uncovered. With the help of the parameters in Table 2.1 and the in-situ measured Au ion milling rate, ~ 0.85 nm/s, the thicknesses of Nb, Py, and Cu layers, Sec. 2.2.2, were converted into effective Au thicknesses and summed up to obtain the total effective thickness of Au (~ 130 nm) used to calculate the etching time ~ 153 s. Approximately 141 s of ion milling was usually sufficient to remove all the Cu and Py; this additional ~ 12 s of etching was done to ensure Nb exposure, during which only ~2.6 nm of Nb was removed. To control the ion milling rates for these films, the vacuum chamber contained a quartz-crystal film-thickness monitor, FTM, which was utilized to measure the Au ion

milling rate in-situ. Au was sputtered at ~ 0.6 nm/s onto the FTM quartz wafer and etched away each time ion milling was performed. Profiles of the samples, acquired with an Atomic Force Microscope, AFM, *NanoScope Digital Instruments D 3100 SPM* were used to check thicknesses; and a SEM, *Hitachi S-4700 II FESEM*, allowed each step of the sample fabrication to be inspected.

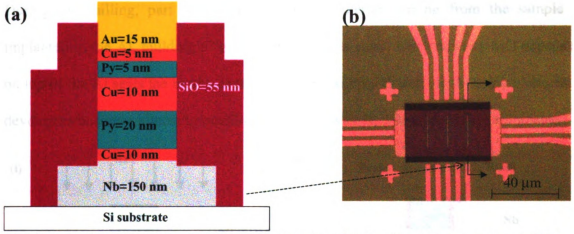

Fig. 2.10. a) Typical profile of a multilayer nanowire after the Al mask was removed. SiO was evaporated leaving a ~13 nm high protrusion of Au. b) Top view of the patterned and planar insulation of SiO.

Right after the samples were ion milled, and without taking the samples out of the vacuum chamber (to prevent oxidation), a layer of SiO was evaporated to planarize and insulate part of the micro-fabricated features from the top Nb or Au strip. Ar supply was interrupted, and deposition took place at pressures of the order of 2 x 10^{-7} Torr. A Tantalum boat containing SiO was heated up at a rate of ~13 A per 5 seconds, using a secondary current from a Variac. When the secondary current trough the boat was ~ 222 A, the boat was hot enough to evaporate SiO. The deposition rate was between 0.2 to 0.6 nm/s. Details of the SiO setup can be found in Ref. 3. However, note that the FTM could be used to check the SiO deposition rate. A 55 nm thick layer of SiO was evaporated leaving a ~13 nm high protrusion of Au, after the Al mask removal, see Fig 2.10 (a). The

samples were held by the magnetic arm and the evaporation was performed while rotating the sample half of the total time clockwise and half anticlockwise at 0.5 r.p.s., see Fig 2.9 (a). In this way a uniform SiO deposition is attained, reducing the chance of pinhole formation.

The final pattern shown in Fig. 2.10 is only obtained when Al masks are removed. During ion milling, part of the backscattered material coming from the sample is implanted in the Al, building a "particle wall" on its sides. Unfortunately SiO deposited on top of the Al seals the masks completely. Thus simply dissolving Al using photoresist developers becomes almost impossible, unless the wall is, at least partially, eliminated

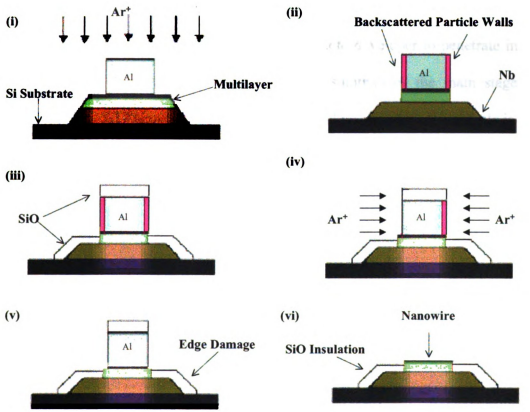

Fig. 2. 11. Cartoon showing the sequence followed to ion mill the substrates and deposit a planar SiO insulation. i) Etching from the top. ii) Particle wall build up on the sides of the Al mask. iii) SiO deposition. iv) and v) Ion milling from the sides to remove build up. vi) SiO lift off via Al removal.

To start "particle wall" removal, the samples were first submerged in Acetone for 20 minutes at 80 °C to remove the resist and clean away the unnecessary SiO deposited on the resist. Next, they were inserted into two grooves constructed in metallic cylindrical holders, see Fig. 2.9 (c), that positioned the substrates in a almost vertical orientation. The ion beam was perpendicular to the longitudinal axes of the wires and at 3° with respect to the plane of the sample substrate. One of the sides of the nanowires was then ion milled for ~ 2.5 min, affecting the "particle wall" only. Ion milling was performed under the conditions described in Sect. 2.2.4. Next, the substrates were rotated 180 ° and placed in holders to ion mill the other size of the nanowire for the same time. Later, the samples were placed in a bath of photoresist developer for 10 minutes. Removal or at least cracking of the "particle wall" allows the photo developer to penetrate into the Al and dissolve it. A cartoon shown in Fig. 2.11 summarizes the main stages of this procedure. Fig. 2.12 shows SEM images of the final result, where the sample is ready for deposition of the final top contact strip.

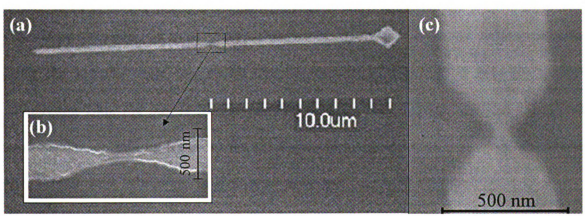

Fig. 2. 12. a) SEM image of a nanowire after SiO deposition and Al removal was finalized. b) Magnification of a U-shaped notch. c) Magnification of a V-shaped notch.

2.2.5 E-beam Lithography and Sputtering to Obtain the Final Top Contact Strip

Following the usual e-beam lithographic step, as described in Sect. 2.2.2, a final 0.9 μm width Nb or Au strip was fabricated to make contact between the multilayer nanowire and the Au electrical leads. Initially two resist layers were deposited, followed by e-beam microscopy. The shapes of the strip were designed to avoid contact with possibly damaged SiO on the bottom Nb layer edges, i.e., with pinholes produced during ion milling from the sides, see Figs 2.11 (v) and 2.13 (a). Two basic strip shapes were fabricated: S and U types. The latter allows tracking of wall motion in two different regions along the wire. As we see in Fig. 2.13, along with the final 150 nm thick Nb strip, two extra 150 nm thick Nb rectangles were built on the ends of the of external Au leads to optimize contacts with the central bottom Nb rectangle. Standard sputtering techniques were utilized to deposit Nb, the sputtering rate was ~ 3 Å/s at an Ar pressure of ~ 6×10^{-3} Torr (base pressure ~ 5×10^{-8} Torr). Deposition took place in the ion milling chamber after the samples were ion milled for 10 seconds to eliminate a possible poorly-conducting film, *the purple plague,* formed between the Al mask and the Au surface underneath. Ion milling followed the conditions described in Sect. 2.2.4. For Nb lift-off, the samples were submerged in an acetone bath at 80 °C for 20 minutes.

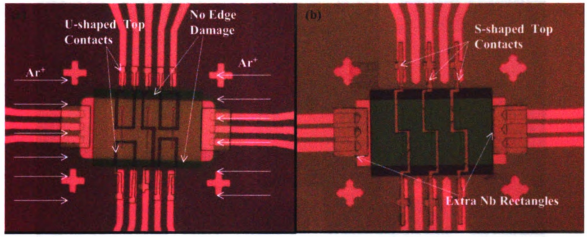

Fig. 2.13. a) Top view of patterned resist mask to create the final top strip. The strips are designed to avoid contact with the SiO-coated edges of the bottom Nb layer that could be damaged by Ar^+ milling. U type strips allow tracking of wall motion in two different regions of the wire. b) Top view of final top Nb S-shaped strips. Extra Nb rectangles assure good connection between the bottom Nb layer and the Au leads.

Because Au has better conductivity than Nb at 295 K, the CPP current-density distribution with Au should be more uniform. In some cases 200 nm thick Au was used instead of 150 nm thick Nb to build the final contact strip, see Fig. 2.14. Very similar procedures to those used for top contact Nb strip fabrication were employed to make the Au top contacts; Au deposition is described in Sect. 2.2.4.

For H = 0, our "dirty" sputtered Nb, deposited in the ion-milling chamber, had a critical temperature, T_c, of ~ 7.2 K, below which the Nb contacts become superconducting equipotential surfaces which produce a uniform CPP current density. Au is normal at all temperatures, and the CPP current density will be non-uniform. However, if we expect good data from Au top contact samples at 295 K, we can also anticipate high quality data from the same samples at 4.2 K because the resistivity of Au will be lower (but not superconducting). To understand this situation of non-superconducting contacts, in the Appendix we present a simple Ohmic model given by Lenczowski *et al.*[11]; who

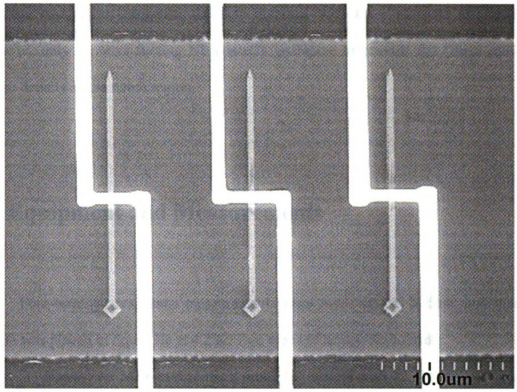

Fig. 2.14. SEM image of three nanowires (V-shaped notch) on the central area of a substrate and S-shaped Au top contacts deposited over the SiO insulating layer. Au top contacts were used for 295-K-measurements mainly.

calculated the current distribution in small pillar like structures for CPP magnetoresistance experiments. Application of this model to our systems shows, as expected, that at 4.2 K the Nb top contact produces totally uniform distribution of thecurrent. At 4.2 K the CPP current density in Au-top contacts is reasonably close to uniform, ~27 % average change between edges of the constriction, and at 295 K its uniformity is worse, ~ 45 % average change between edges. Very similar behavior is shown by the current density distribution of Nb top contacts at 295 K. This is an indication that at 295 K (because of the presence of the non-superconducting bottom Nb contact) changing the top contact does not affect the current-density distribution significantly. These non-uniformities of the CPP current densities for Au top contact samples at 4.2 K and 295 K, and for Nb top contact samples at 295 K, are significant, but

not large enough to categorize the data obtained with these contacts as unreliable. However, only superconducting Nb contacts guarantee to provide the "most uniform" current density in the notch region.

2.3 Equipment and Measurements

Four-terminal resistance measurements were made at 295 K first, and then the sample was placed in liquid He at 4.2 K. Two types of setups were used :

(1) **Nano-Volt Measurements**: a multiplex system with 12 channels, six current channels and six voltage channels, was used to measure samples with resistances bigger than 100 μΩ. This setup uses a DC current source and a DC nanovoltmeter to measure samples .

(2) **Lock-in Amplifier (LA):** this system was used to detect and measure very small AC signals (a few nano-volts), allowing comparable signal-to-noise ratios for currents smaller than in (1). Due to this advantages of the LA over (1), most of the data were obtained with it. The probe system is similar to (1) with 12 channels, 6 voltage channels and 6 current channels. This system was also used to measure samples with resistances bigger than 100 μΩ. LA has the particular advantage that a DC current can be added to the AC currents, allowing current dependence measurements. The LA filters the DC current component, and only the AC component of the current is utilized to measure the resistance of the sample.

2.3.1 Nanovolt Measurements

A *Keithley 2400* current source supplied current and a *Keithly 2182* nanovolmeter measured the voltage. With the help of a *Keithly 7001* multiplexer, the system was designed to allow different samples to be measured on an single substrate without removing the sample probe from the liquid He dewar.

The probe, which can be used at room temperature and at 4.2 K, consisted of six current and six voltage Cu leads that were connected to the external measuring equipment. Each connection included shorting and grounding switches for each individual lead; it was possible to ground directly or ground through a 1 MΩ resistor. These switches prevent the small features of the e-beam samples from burning out due to static charges effects. The current leads are connected to the probe via a Fisher seven-pin connector, while three Cu Omega-Engineering thermocouple connectors are used to connect the voltage leads. Each thermocouple connector has two leads plus a ground connection. This kind of all-Cu wire system minimizes voltage offsets and drifts due to the thermoelectric effects at room temperature. More information about this set up, including construction details of the probe, can be found in Ref. 3.

2.3.2 Lock-in Amplifier

Both an AC voltage signal, at a specific reference frequency (8 KHz), and a DC voltage signal were supplied by a *SR844 Stanford Research Systems* Lock–in Amplifier.

The voltages were added and converted to a current sent to the sample, (I^+ and I^-) via an adapter. The AC voltage signals coming from the sample, (V^+ and V^-), were subtracted and pre-amplified by a *Stanford Research* preamplifier *SR552* and sent back to the Lock-in Amplifier, which uses a phase sensitive detection technique to extract the component of the signal at the reference frequency and phase. A diagram of the measuring system is presented in Fig. 2.15.

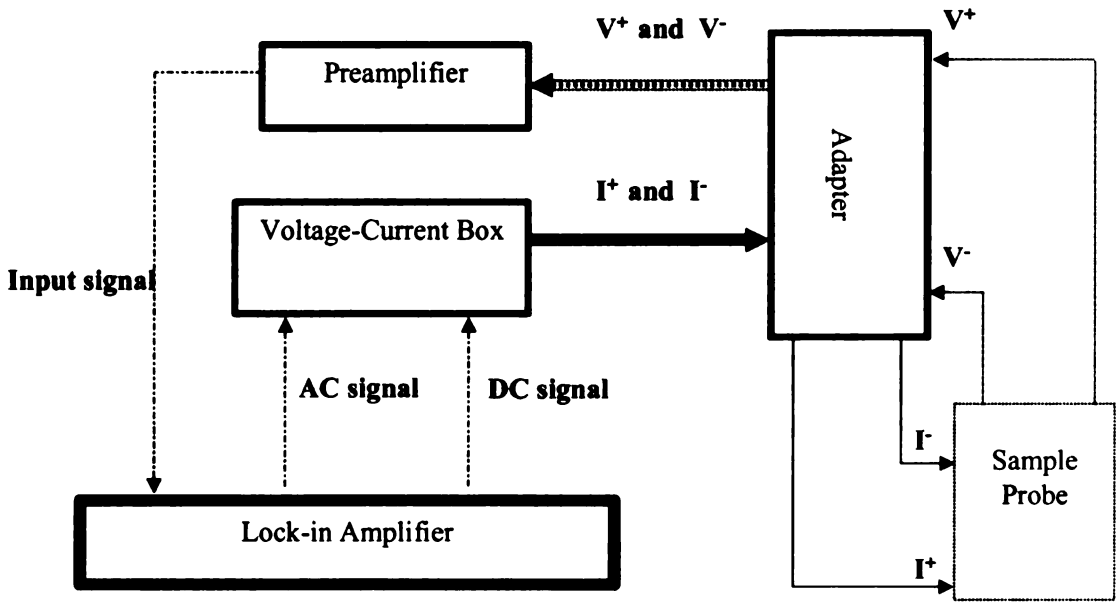

Fig. 2.15. Diagram of the measuring system. The Lock-in amplifier is connected to the Voltage-Current Box via two co-axial cables and from there a triaxal cable goes to an adapter. The adapter is used to change the current triaxal cable into a Fisher seven-pin connector, which goes to the sample probe. The adaptor is also used to change the Cu Omega-Engineering thermocouple connectors into a triaxal cable which brings back the voltage to the preamplifier. The adapter selects the channels to be used as well. The preamplifier is connected via a coaxial cable to the Lock-in amplifier.

The sample probe can be used with either the lock-in system or the Nanovolt system. The probe allows contact to all three nanowires on the same substrate, but only one nanowire is measured at a time. Each substrate was placed at one end of the long probe, as shown in Fig 2.16 (a) and (b), in such a way that the nanowires were aligned parallel to the longitudinal axis of the probe and the external magnetic field. To protect

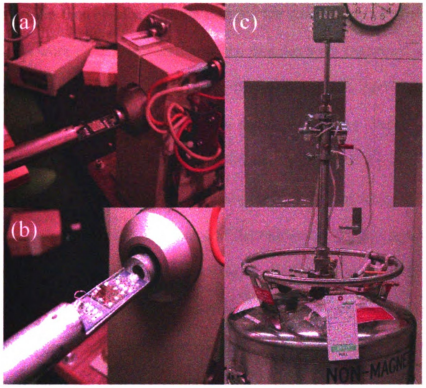

Fig. 2.16. a) Photo of the room temperature magnet with the probe not yet inserted. b) The substrate is placed at one end of the long probe, and the samples are connected via indium contacts to the probe Cu wires. c) The probe is inserted into the sheath that contains a superconducting solenoid, and the whole system is dipped into a He dewar.

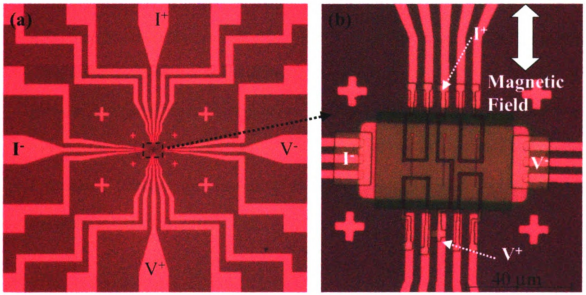

Fig. 2.17. Sample connections. a) The external Cu leads are connected with indium to the sample via the external contacts at the outer edges of the substrate. V and I external contacts are shown for connection to the central nanowire. b) Magnification of the central part of the substrate.

the sample from blowing due to static charges, the shorting switches of the voltage and current leads were closed; and then after the samples were connected according to Fig. 2.17, the external shorting Au bridges on the substrate were cut. For low temperature measurements, the measuring probe fits inside a separate sheath that contains a superconducting solenoid of coil constant 506.6 Gauss/A, see Fig 2.16 (c). This coil has a persistence switch[3] across it that produces a constant flow of current through the coil, thereby reducing the noise in the magnetic field produced by the magnet current supply. In the case of the LA system, this switch was kept open because each point was taken in less than 4 seconds, comparable to the time necessary to open and close the persistence switch. For room temperature measurements, the probe was separated from the sheath and inserted into a standard electromagnet of coil constant 821 Gauss/A as shown in Fig. 2.16 (a) and (b). Two power supplies can control either magnet, one of 8 A range and another of 2 A range. The external magnetic field resolution was increased by changing the original 12-bit GIPB card to control the magnet power supplies to a analog 16-bit A/D card, *National Instruments: PCI-6731*. The external magnetic field was applied along the longitudinal axis of the probe and mainly swept between –500 Oe and 500 Oe. Between data points the H sweep rate was ~200 Oe/s, and the time for each measurement was usually 1 to 3 s. A Lab-View program automated the measurements and calculated R. Studies of standard resistors indicate that the long-term drift of electronics were ≤ 0.02 mΩ at 4.2 K and ≤ 0.2 mΩ at 295 K.

REFERENCES

[1] J.M. Slaughter, W. P. Pratt Jr., and P.A. Schroeder, *Review of Scientific Instruments* **60**, 127 (1989).

[2] Shang-Fan Lee, Ph.D. Dissertation, Michigan State University (1994).

[3] *Perpendicular Giant Magnetoresitance in thin Films with Microfabricated Superconducting Top Contacts*, R. D. Slater Dissertation (2001).

[4] Qing Yang, Ph.D. Dissertation, Michigan State University (1995).

[5] T. Ono, H. Miyajima, K.Shigeto and T. Shinjo, *Appl. Phy. Lett.*. **72,** 1116 (1998).

[6] Y. Yokoyama, Y. Suzuki, S. Yuasa, K. Ando, K. Shigeto, T. Shinjo, P. Gogol, J. Miltat, A. Thiaville, T. Ono, and T. Kawagoe, *J. Appl. Phys.* **87**, 5618 (2000).

[7] K. Shigeto, T. Okuno, T.Shinjo, Y.Suzuki, and T. Ono, *J. Appl. Phys.* **88**, 6636 (2000).

[8] K. Shigeto, T. Shinjo, and T. Ono, *J. Appl. Phys.* **75**, 2815 (1999).

[9] *Commonwealth Scientific Corporation* One-CM Ion source manual.

[10] Characteristics , Capabilities and Applications of Broad-Beam Sources, H R Kaufman, R. S. Robinson and W. E. Hughes, *Commonwealth Scientific Corporation* (1987).

[11] S.K.J. Lenczowski, R. J. M. van de Veerdonk, M.A.M., J. B. Giesbers , and H.H. J. M. Janssen, *J. Appl. Phys.* **75,** 5154 (1994).

CHAPTER 3

Results and Discussion

3.1 Introduction

As indicated earlier in this thesis, several current-in-plane magnetoresistance, CIP MR, experiments have been performed to measure the localization and motion of geometrically confined domain walls in nanostructures. Since the pioneering work by T. Ono *et al.*[1-2], showing trapping of a domain wall in a notch placed in a long wire without a reservoir, subsequent work has shifted to using high CIP current densities to manipulate the wall motion in such narrow structures[3-5]. A significant contribution to this field was made by Kläui *et al.*[3], who used a narrow single layer ferromagnetic ring with notches where head-to-head walls could be manipulated by the orientation of an in-plane magnetic field and by high current densities circulating around the ring.

In this chapter, we present the results of our various works done to study domain wall trapping and motion using CPP MR as an alternative to CIP MR utilized until now. As our data will show, the utilization of a localized CPP current enhances the sensitivity for detecting the presence and motion of a trapped domain wall, and allows us to choose the measuring region almost independently of the sample geometry. The results presented

in this chapter principally consist of CPP resistance, R, vs. sweeping magnetic field, H, curves; but also studies of domain wall stability, time dependence of wall motion inside a constriction and effects of high-density CPP currents are included.

3.2 CPP Resistance Data

The development of this work can be divided into three periods. In the first one, no electron-microscope characterization, "NC", of the notch geometry was done because the CPP resistance measurements needed to be perfected first, and only "proof of wall trapping" from the CPP MR was required. In the second period, the design of the U-shaped constrictions was well characterized with a *Hitachi S-4700 II FESEM.* In the third period the constrictions were changed into V-shapes, which were also properly characterized by means of the *SEM.*

Table 3.1 presents the CPP resistance data of all the samples which successfully showed trapping of a domain wall. R_{AP}, and R_P are resistances of the antiparallel, P, and parallel, AP, states respectively, and GMR = $R_{AP} - R_P$ / R_P. Sample identification numbers provide information about the sputtering run number, substrate number and nanowire employed. A single asterisk, *, indicates that the sample was measured using a Au top contact first, and then it was remeasured with a Nb top contact deposited on top of the original Au contact. A double asterisk, **, indicates that the width of the top contacts was increased by a factor of 1.5. Table 3.2 shows the average values of the data presented in Table 3.1. These averages were calculated for eight groups of samples defined by their

notch shapes, top contact types and measuring temperatures. Uncertainties were estimated by $\sigma/(n)^{1/2}$, where σ is the data standard deviation and n the number of measurements.

Sample	Notch Type	Top contact	Temperature (K)	$\Delta R=R_{AP}-R_P$ (mΩ)	R_{AP} (mΩ)	GMR (%)
1470-1B-a	U	Au	4.2	3.0	24.8	13.79
1470-1B-b *	U	Nb	4.2	5.0	62.5	8.70
1470-2A-b	U	Nb	4.2	5.0	152.0	3.40
1470-5B-a	U	Nb	4.2	1.9	47.3	4.19
1470-5B-b	U	Nb	4.2	4.0	188.0	2.17
1470-5B-c	U	Nb	4.2	3.5	120.0	3.00
1492-1A-b	U	Nb	4.2	4.5	140.0	3.32
1492-1A-a	U	Nb	4.2	3.4	62.5	5.75
1470-6B-a	V	Nb	4.2	3.6	143.6	2.53
1563-7B-a	V	Nb	4.2	5.0	90.5**	5.85
1459-7B-a	NC	Au	295	3.2	760.0	0.42
1470-1A-a	NC	Au	295	16.0	1242.0	1.31
1470-1A-b	NC	Au	295	17.0	1330.0	1.29
1470-1A-c	NC	Au	295	29.0	1440.0	2.06
1470-1B-a	U	Au	295	1.5	653.0	0.23
1470-1B-b	U	Au	295	2.3	760.6	0.30
1470-1B-b*	U	Nb	295	2.5	818.0	0.30
1470-2A-a	U	Nb	295	3.0	820.0	0.37
1470-2A-b	U	Nb	295	4.0	480.0	0.84
1470-3B-c	U	Nb	295	3.2	989.5	0.32
1470-5A-c	U	Nb	295	0.8	290.0	0.28
1563-7A-b	V	Nb	295	1.3	655.0**	0.20
1563-7B-b	V	Nb	295	2.0	946.0**	0.21
1563-7B-a	V	Nb	295	2.5	907.0**	0.27
1563-8B-a	V	Au	295	1.8	623.0**	0.29
1563-8A-b	V	Au	295	1.2	391.0**	0.30

Table 3.1. Experimental data of samples showing trapping. R_{AP} and R_P are resistances of the antiparallel and parallel states, respectively. GMR = $R_{AP} - R_P / R_P$. * means samples remeasured with extra Nb strip over the original Au top contact strip. ** indicates that the width of the top contacts was increased by a factor of 1.5.

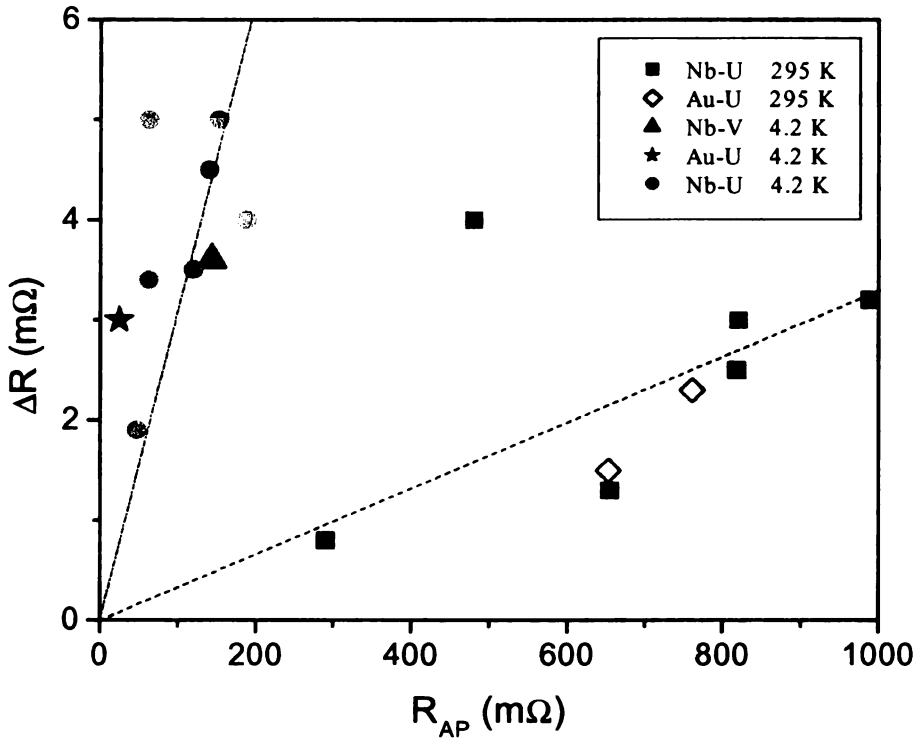

Fig. 3.1. $\Delta R = (R_{AP}-Rp)$ vs. R_{AP}. Two least-squares fits were performed: at 295 K (all the points were considered); and at 4.2 K (Au-U and Nb-V were excluded). Lines were forced to go through the origin.

Fig. 3.1 shows $\Delta R = (R_{AP}-R_p)$ vs. R_{AP} at 295 K and 4.2 K. Two least-squares fits were performed: at 295 K, in which all the points were considered, and at 4.2 K, in which Au-U and Nb-V were excluded. These linear fits were forced to go through the origin. In the ideal case of a perfect sample with one value of CPP area, these data should coalesce into one point for each temperature. This clearly not the case in Fig. 3.1. If the variations in CPP area were the only source of R_{AP} and ΔR fluctuations, the data should follow the two best-fit lines in Fig. 3.1, where (0,0) correspond to an infinite CPP area. At 295 K, with the exception of the point at R_{AP} = 480 mΩ (1470-2A-b), these data do seem, to follow this trend, but with large fluctuations. At 4.2 K, the fit appears to be worse. We speculate that the contact region between the top and Au layer of the sample and the Nb top contact may be "dirty", introducing both a variable effective contact area and a

contact resistance that will cause R_{AP} and ΔR to fluctuate. Thus it may be important to explore ways of making more reliable contacts between the upper surface of the sample and the top contact.

	4.2 °K	4.2 °K	4.2 °K	295 °K	295 °K	295 °K
	$R_{AP\text{-}Av}$ (m Ω)	ΔR_{AV} (mΩ)	GMR_{AV} (%)	$R_{AP\text{-}AV}$ (mΩ)	ΔR_{AV} (mΩ)	GMR_{Av} (%)
Nb-U	110 ± 20	3.9 ± 0.4	4.3 ± 0.8	680 ± 128	2.7 ± 0.5	0.42 ± 0.11
Au-U	~ 25	~ 3	~ 13.8	507 ± 116	1.5 ± 0.3	0.3 0 ± 0.01
Nb-V	~ 143***	~ 3.6	4.2 ± 2.7	717 ± 92	1.8 ± 0.3	0.25 ± 0.02
Au-V				707 ± 54	1.9 ± 0.4	0.27 ± 0.03
Au-NC				1193 ± 113	16.3 ± 4.0	1.27 ± 0.25

Table 3.2. Average values of the experimental data presented in Table 3.1. The uncertainties were estimated by $\sigma/(n)^{1/2}$, where σ is the data standard deviation and *n* the number of measurements. *** sample 1563-7B-a was not considered in the average.

In spite of the data fluctuation seem in Fig. 3.1, it is still worthwhile to compare the calculated values of R_{AP} , ΔR, and GMR using the 2CSR model, Sect. 1.2.3, with the 4.2-K experimental values of the same quantities. Surprisingly, the average experimental value of $R_{AP} \sim 110$ mΩ for Nb-U samples, shown in Table 3.2, is reasonable close to the calculated value, shown in Table 1.2, $R_{AP\text{-}calc} \cong 77$ mΩ. However, $\Delta R_{calc} \cong 7.2$ mΩ and $GMR_{calc} \cong 10\%$ are ~ 80% higher than the corresponding experimental values, see Table 3.2. The inclusion of a contribution from the dirty Au/Nb interface in our calculations could increase $R_{AP\text{-}calc}$ and reduce ΔR_{calc} and GMR_{calc}.

For Au-U samples at 4.2 K, comparing experimental, Table 3.2, and calculated values, Table 1.2, is more suspect because there is only one experimental point. Nevertheless, there are indications that our calculations match one aspect of the experimental data: $GMR_{calc} \cong 17\%$ and the experimental GMR ≅ 14% are rather close. Unfortunately, experimental $R_{AP} \sim 25$ mΩ < $R_{calc} \cong 75$ mΩ; and experimental $\Delta R \cong 3$

$m\Omega < \Delta R_{calc} \cong 11\ m\Omega$. Thus, the experimental and calculated values of R_{AP} and ΔR differ by about a factor of three. This discrepancy is not understood at present.

3.3 CPP Resistance vs. Magnetic Field

Fig. 3.2 shows the CPP R as a function of the sweeping field, H, for a V-shaped notch. Near + 500 Oe, the cartoon shows that the magnetization of the thin and thick Py layers are in the parallel state and pointing to the right (filled arrows along +x). This is the low resistance, R_P, state. The field is then lowered until a head to head domain wall is injected into the thin Py layer of the wire from the reservoir at the right at –10 Oe and becomes trapped at the notch. Such low injection fields agree with earlier work by Ono *et al.*[1] For the thin Py layer, magnetization, J, on the right side of the wall is reversed, as shown (open arrow along –x). As H is lowered further, the CPP MR detects an average motion of the trapped wall to the left. At H = –100 Oe, the wall leaves the notch, and the two magnetizations are now in the AP, high R state, R_{AP}. Further reduction of H causes a head-to-head wall to be injected and trapped in the thick Py layer at H = –230 Oe. Finally, by –400 Oe, the wall in the thick Py layer has left the notch, and the magnetizations are now in the P state. Starting at –500 Oe and increasing the field gives very similar trapping behavior in R for the thin and thick Py layer, but with tail-to-tail walls.

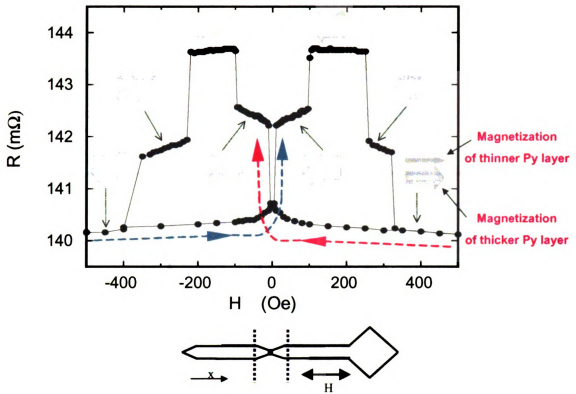

Fig. 3.2. CPP resistance R vs. magnetic field, H, at 4.2 K for a V-shaped notch. Curved dashed arrows indicate change in H. Sample1470-6B-a, Nb top contact.

In Fig. 3.3 we present $\Delta R(=R-R_P)$ vs. H for a U-shaped notch with a Au top contact, which has a very respectable GMR of $(R_{AP} - R_P)/R_P \equiv 14\%$. In contrast to the V notch of Fig. 3.2 where one trapping step occurs in the thin Py layer, here we see several intermediate trapping steps that commence once the wall is injected into the wire at $|H| \sim$ 10 Oe. The direction of field sweep affects these steps. We also see no trapping of the wall at the notch in the thick Py layer. As opposed to the V notch case where the wall pinning site is better defined, the more elongated U notch can have wire edge roughness and other defects which seem to act like multiple similar-strength pinning sites where trapping of the DW can occur. This is somewhat similar to what was observed by Grollier at *et al.*[5], who detected domain wall pinning in defects of a Py stripe with no notch, and

by Giordano *et al.*[6-7], who showed that magnetization reversal in very narrow Ni nanowires (with no constriction) appears to be dominated by pinning of the domain wall on defects. Studies of standard resistors at 4.2 K indicated that long term drifts of the electronics were ≤ 0.02 mΩ, significantly less than the substeps seen in Fig.3.3.

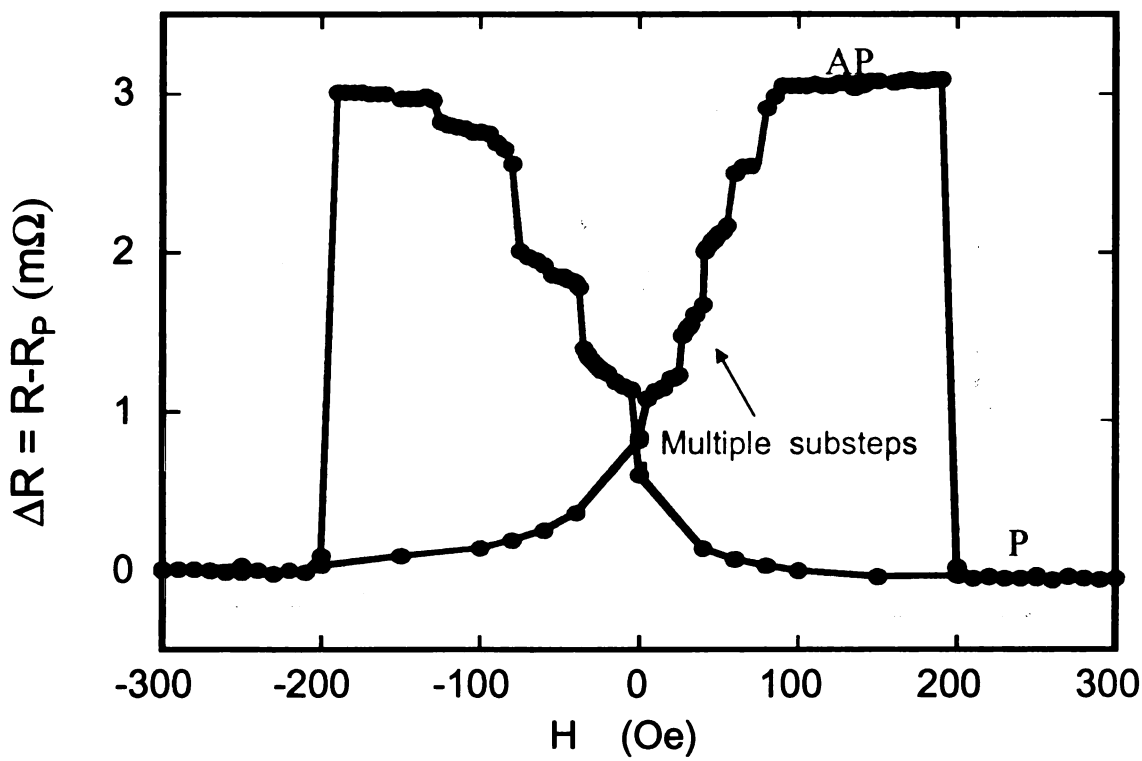

Fig. 3.3. ΔR (=R-R_P) vs. magnetic field, H, for a U shaped notch. R is resistance, AP means antiparallel state and P means parallel state. Arrows indicate different H sweeps. Sample 1470-1B-a, at 4.2 K, Au top contact.

In Fig. 3.4 a ΔR vs. H curve at 295 K for a NC sample type is shown. Here we observe two wall-trapping substeps in the thin Py layer that are not affected by the field direction. We also see a single trapping step in the notch area of the thicker Py layer, which is affected by the sweep field, making the characteristic resistance value of the step and its length differ between sweeps. The data also show that CPP detection of domain

wall motion can be measured at 295 K, even with non uniform CPP currents. See Appendix.

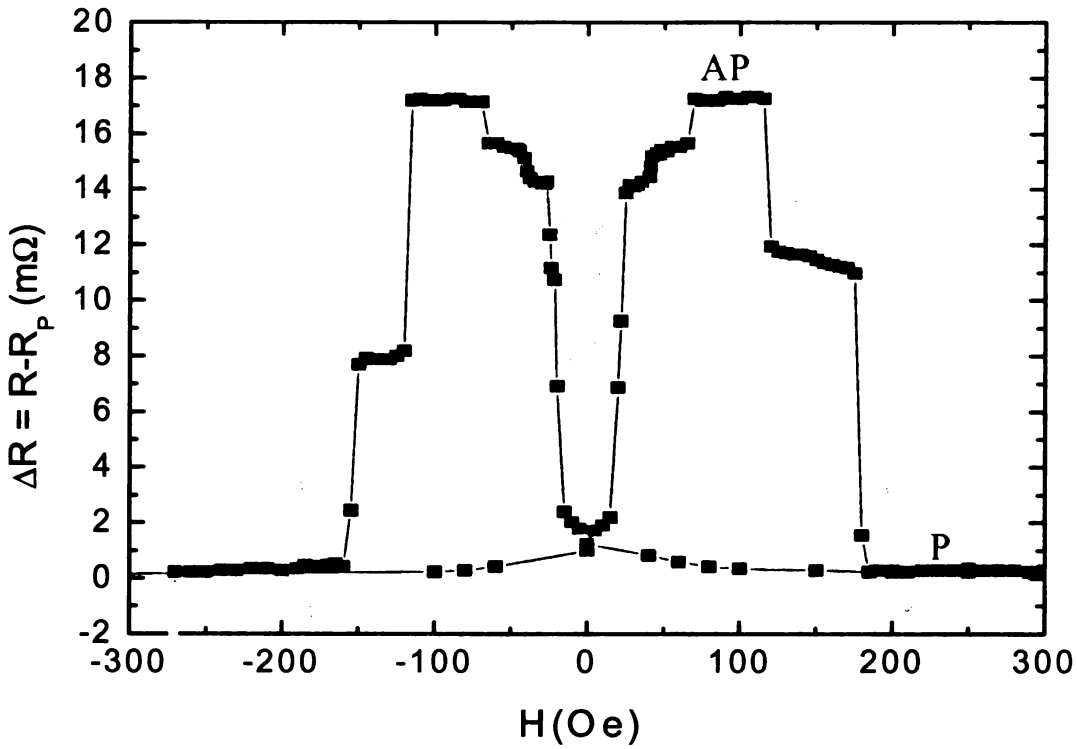

Fig. 3.4. $\Delta R(=R-R_P)$ vs. magnetic field, H, for a NC notch. R is resistance, AP means antiparallel state and P means parallel state. This curve has two reproducible wall-trapping substeps for the thin Py layer. Arrows indicate different H sweep. Sample 1470-1A-a at 295 K, Au top contact.

Assuming that the top contact is perfectly centered on the constriction, R values of the wall-trapping steps tell us what the position of a wall in the notch is. For instance, in Fig. 3.2, having R values of the wall-trapping steps that are almost halfway between P and AP resistances means that walls are trapped near the middle of the constriction in the thin Py layer. In Fig. 3.3, the resistance shows multiple jumps between the P and AP states, and this means that the wall gets pinned at many different sites along the "entire" U-shaped notch. If R shows reproducible pinning points, like in Fig. 3.4, we can determine the position of these sites in the notch and with this information characterize an unknown notch shape. In Fig. 3.4 only two wall-trapping substeps appear for the thinner

Py layer, which indicates that this NC constriction is close to a V-notch shape. The main trapping seems to occur just before the wall leaves the constriction, which implies that the notch is asymmetric.

3.4 Multiple Runs

Fig. 3.5 shows two characteristic groups of R vs. H curves. The first group is shown in Figures (a) and (b) that correspond to U and V shaped notches with well defined geometry. These reasonably reproducible curves indicate that walls almost follow the same path through stable pinning sites in the thin Py layer. In spite of this stability, wall-trapping steps in the thicker Py layer are less reproducible in the thinner Py layer. Constrictions with roughness and probable lack of symmetry belong to the second group, inherent to U shape notches only. Figs.3.5 (c) and (d) show no wall path reproducibility, not only in the number of substeps but also in their resistance values. Even when these different sweep curves do not exhibit the same behavior, they do show signs of some periodicity. For instance, in Fig. 3.5 (c) we observe that wall-trapping in the thinner Py layer always takes place between ~ 10 Oe $\leq |H| \leq$ ~100 Oe, and many runs present two clear R jumps at ~$|30|$ Oe and $|60|$ Oe. In Figs. 3.5 (c) and (d) we also see that wall trapping in the thicker Py layer is rare.

It is important to note that for the thinner Py layer in Fig.3.5: (1) the injection field from the reservoir has a reasonable stable value of $|H|$ ~10 Oe which is independent

of the notch type (since this injection field depends mainly on the properties of the reservoir and its connection to the nanowire, this notch-shape independence is expected), and (2) the escape field from the notch, is more variable from sample to sample but mostly occurs for 50 Oe $\leq |H| \leq$ 150 Oe. Also note that in all these curves for $|H| \leq 100$ Oe and no trapping, MR readily detects a subtle readjustment of the magnetizations away from the P state for the two Py layers (this is shown in an increase of R as |H| decreases).

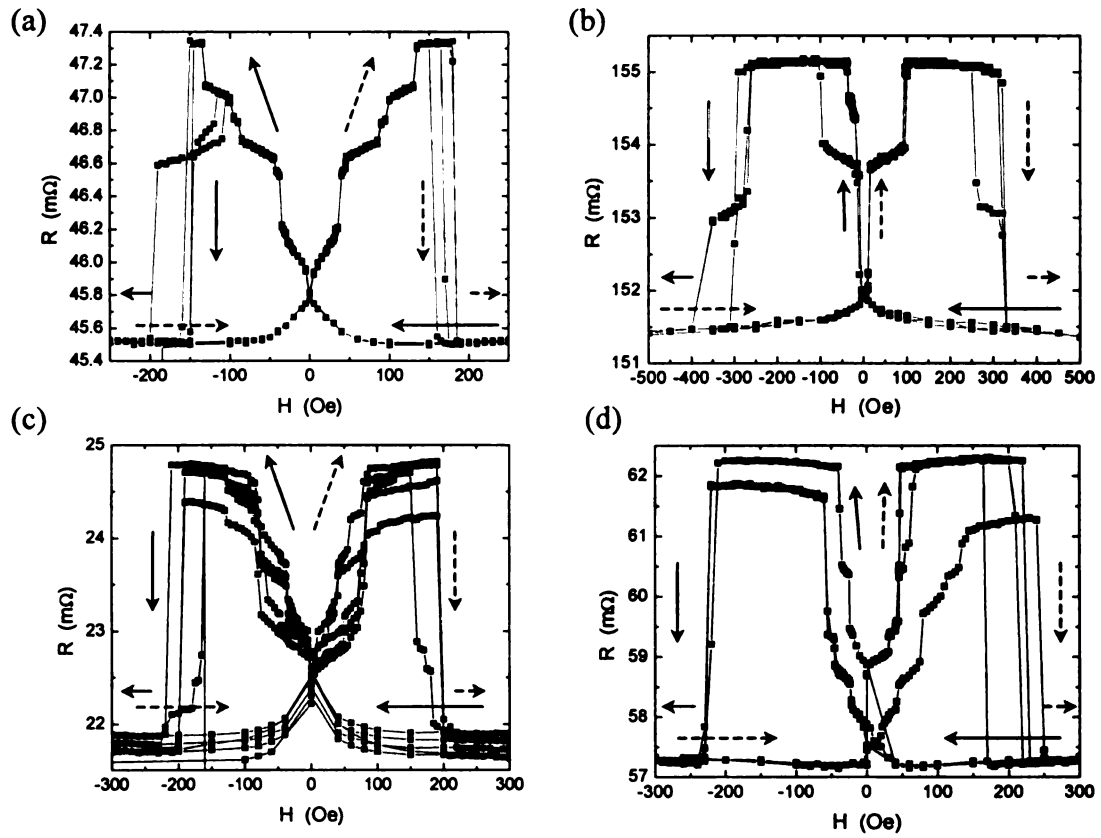

Fig. 3.5. Multiple CPP resistance, R vs. magnetic field, H, curves. H sweeps move back and forward between –500 Oe and 500 Oe. Samples a) 1470-5B-a at 4.2 K, U-shaped notch, Nb top contact, and b) 1470-6B-a at 4.2 K, V- shaped notch, Nb top contact. Stable and reproducible configurations. U-shaped notches only: samples c) 1470-1B-a at 4.2 K, Au top contact, and d) 1470-1B-b at 295 K Nb top contact. More unstable configurations.

In Fig. 3.5, injection fields for a wall in the thicker Py layer typically vary between $|H| \sim$ 150 Oe and ~ 300 Oe, which are up to 30 times larger than those for a wall

in the thinner Py layer, $|H| \sim 10$ Oe. One would have expected injection fields to scale with thickness, 20nm/5nm = 4.[8] Perhaps dipole coupling between Py layers in the reservoir (see Sect. 1.3.5) causes these "low" injection fields for walls in the thinner Py layer, and variable high injection fields for walls in the thicker Py layer. Note that the injection fields of the wall in the thinner Py layer are ~10 times smaller than their escape fields, $|H| \sim 100$ Oe. In the thicker Py layer this ratio of escape field to injection field is much smaller (< 2). High injection fields means that the barrier is already lower in the notch region, and this might explain why it is more difficult to trap walls in the thick Py layer. This, plus the variability of the wall-injection fields in the thicker Py, would also explain why the AP→P state transition field can fluctuate from run to run.

3.5 Sample with CPP Current outside Constriction

As we already mentioned in Sect. 3.4, in Figs. 3.2 to 3.5 for $|H| \leq 100$ Oe and no trapping, the MR detects a slight alteration of the magnetizations away from the P state for the two Py layers. This is likely due to residual dipolar coupling between these two layers in the notch region. See Sect. 1.3.5. To confirm that this behavior was only associated with inside the notch region, we placed an extra Nb top contact well to the left of a U-shaped constriction, as shown in the inserts of Figs. 3.6 and 3.7.

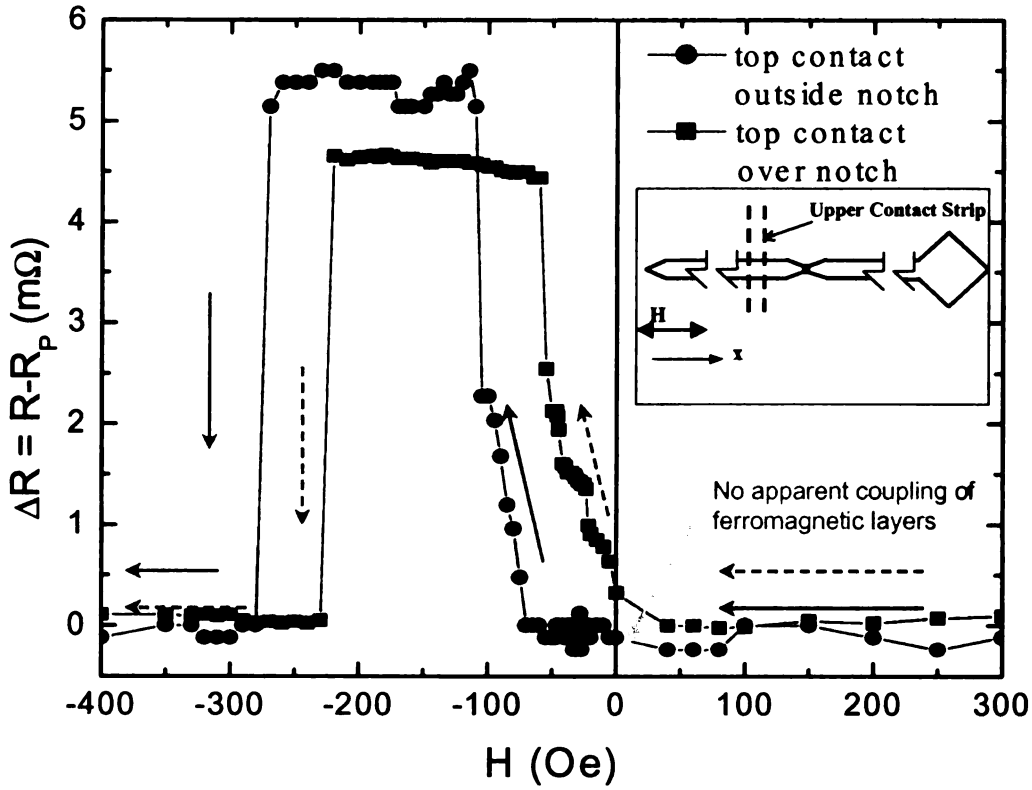

Fig. 3.6. ΔR (= R – R_P) vs. H for a sample with one Nb top contact placed to the left of a U-shaped notch and the other contact over the notch. Solid and dashed arrows show direction of field sweep at 4.2 K. Sample 1470-1B-b*, Nb top contact.

Fig. 3.6 shows for the top-contact-outside-notch, TCO, data that, for -70 Oe ≤ H ≤ +300 Oe, $\Delta R = (R - R_P) = 0$, indicating a lack of residual dipole coupling in the notch free part of the wire, as expected, see Sect. 1.3.5. A similar behavior is observed at 295 K for -40 Oe ≤ H ≤ +300 Oe, see Fig. 3.7. Fig. 3.6 also shows that at H ~ -70 Oe, the wall leaves the CPP current region of the U notch and begins entering the CPP current region of the TCO. This situation is repeated in Fig. 3.7, but at a lower value of H ~ -50 Oe, as expected (because of thermal effects). In Fig. 3.6, for -110 Oe ≤ H ≤ -70 Oe, there is some evidence of trapping in the TCO curve before the AP state is attained, presumably due to stress introduced during cooling of the sample. During material deposition, interface stresses are generated between layers; and these stresses can increase during

cooling of the sample at 4.2 K due to differential thermal contraction. Seemingly the main contribution to stress in the Py layer comes from the top contact Nb. These non magnetic stresses can act like wall-pinning defects along the Py nanowire, see Sect.1.3.1. In Fig. 3.7 we also observed that, at 295 K, the expected lower stress and higher thermal activation allow a cleaner transition to the AP state. In Fig. 3.6 the AP→ P state transition is at H~-270 Oe for the TCO data and at H~-225 Oe for the top-contact-over-notch curve. This is explained, as we saw in Sect. 3.4, by the fluctuation, from run to run, of the injection field of a wall in the thicker Py layer (recall that the injection field of the thinner Py layer is more stable). This would also explain the difference in AP→ P state transition fields observed in Fig 3.7.

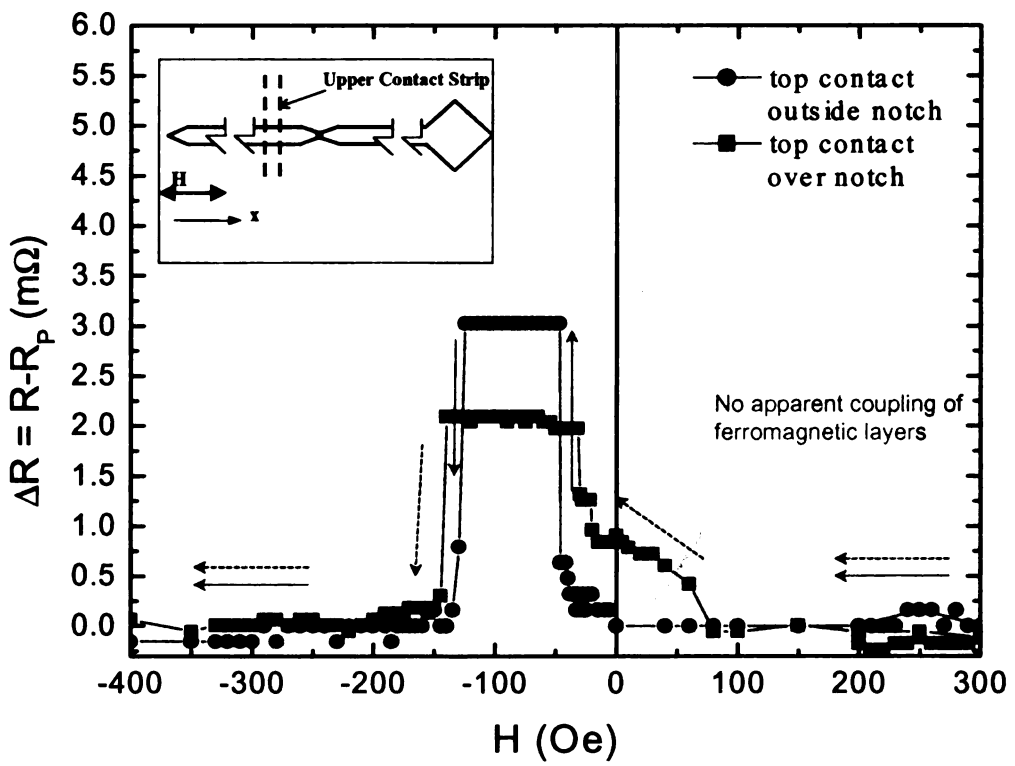

Fig. 3.7. ΔR (= R – R_P) vs. H for a sample with one Nb top contact placed to the left of a U-shaped notch and the other contact over the notch. Solid and dashed arrows show direction of field sweep at 295 K. Sample 1470-1B-b*, Nb top contact.

The localized CPP current studies presented here clearly demonstrated the power of this technique. We have confirmed our assumption that the wall is injected from the reservoir on the right and moves to the left, passing through the notch region first and then sweeping under the top contact outside the notch (located to the left).

3.6 Estimation of the Displacement of a Domain Wall within the Constriction

The response of the trapped wall to H in the thinner Py layer produces an approximate linear variation of R that has a maximum value $\delta R \sim \Theta \times (R_{AP} - R_P)$, where Θ is determined by the "strength" of the pinning site. This is clear consequence of the enhanced sensitivity for domain wall motions given by CPP MR, which cannot be obtained by using CIP MR instead. Earlier CIP results showed no linear variation of R with field for trapped walls.[1]

As we saw in Sect. 1.3.5, Mc Michael *et al.*[9] have done macromagnetic simulations for a head-to-head wall of transverse magnetization ($\perp$ x) that is trapped in a trapezoidal notch cut into one side of a narrow wire in a very thin Py layer. Such simulations indicate that the average magnetization J_x varies linearly with H during trapping. Since the CPP MR varies approximately as the average J_x for the thin Py layer within the area defined by the top Nb contact (while J of the thick layer remains fixed), the simulations would predict the linear response in R that we see.

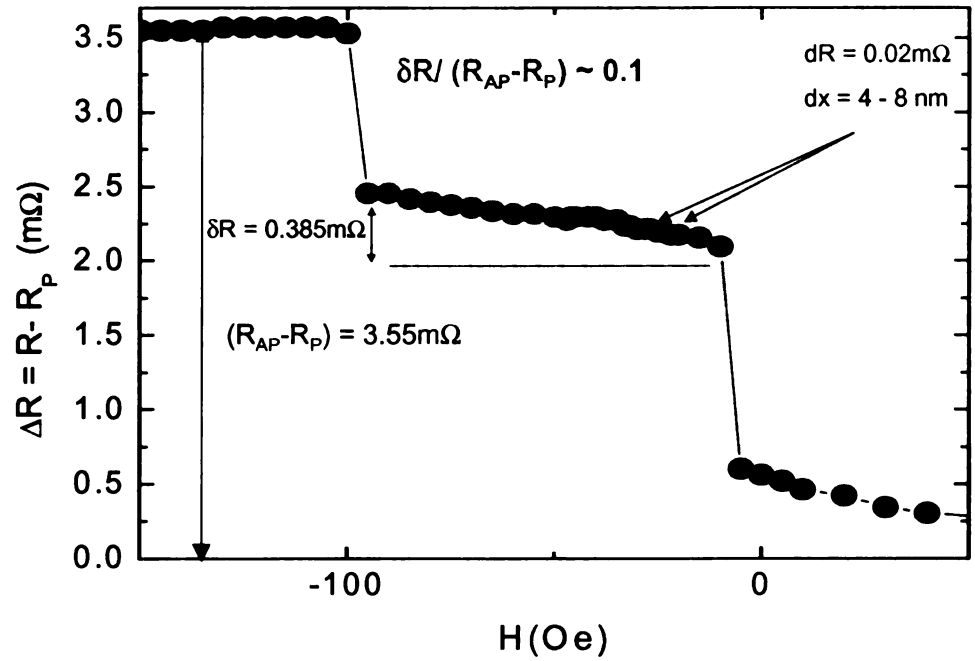

Fig. 3.8. $\Delta R = (R-R_P)$ vs. magnetic field, H, data showing the displacement of the wall trapped in the thin Py layer within the constriction. δR value from the V shaped notch puts a constraint on the relationship between the width of the domain wall and the distance the trapped wall moves as the field changes. Sample1470-6B-a, Nb top contact, Fig. 3.1.

Such simulations also indicate that the width (along x) of this transverse region for the head-to-head wall is approximately equal to the width ($\perp$ to x) of the notch region. One can use the δR value from a V shaped notch to put a constraint on the relationship between the width of this transverse region and the distance the trapped wall moves (along x) as the field changes. As seen in Sect. 1.3.6, we adopt a very crude model where the head-to-head wall (of fixed width D or fixed wall area, A_w) is uniformly magnetized transverse to x and elsewhere the uniform J is either parallel or antiparallel to x. For instance, for the V-shaped notch of Fig. 3.2, we have $\Theta \cong 10\%$, see Fig 3.8. Therefore, this simple model predicts that, if the initial domain width, D_o, is ~100 nm (~ the width

of the notch ⊥ to x), then the δR corresponds to a ~ 150 nm displacement of the wall. However, if $D_o \cong 600$ nm (comparable to the length of the notch along x or to the width of the wire), then the displacement is ~ 70 nm.

Note that at 4.2 K the long term drifts of the electronics were ≤ 0.02 mΩ. This means that, based on the correspondence between δR and the wall displacement discussed above, we can detect with the CPP-MR subtle average wall motions of ~ 4-8 nm.

3.7 Stability of a Wall within the Constriction

Fig. 3.9 shows motions of a wall trapped in a U-shaped notch at 295 K, Au top contact sample. H is first increased to 500 Oe to attain the P state, point 1, and then is sweept back until a head-to-head wall in the thinner Py layer gets trapped in the constriction, H~-20 Oe. A further decrease in H causes the wall to jump significantly, ending up at point 2, H~-40 Oe. After that, the sweeping field is increased gradually, and R indicates that the wall varies its position within the constriction but stays trapped until the sweeping field rises above 10 Oe, point 3 in Fig. 3.9 (b). When H is progressively swept back to -50 Oe, the wall gets trapped in the notch again, and then leaves it, achieving the AP state at point 4 in Fig 3.9 (b). Even when H is swept between –50 Oe and 20 Oe, points 4 and 5 in Fig 3.9 (b), $\Delta R(= R-R_p)$ maintains a constant value. Thus

once the wall has left the notch, the AP state is quite stable over this range of fields because the wall does not return.

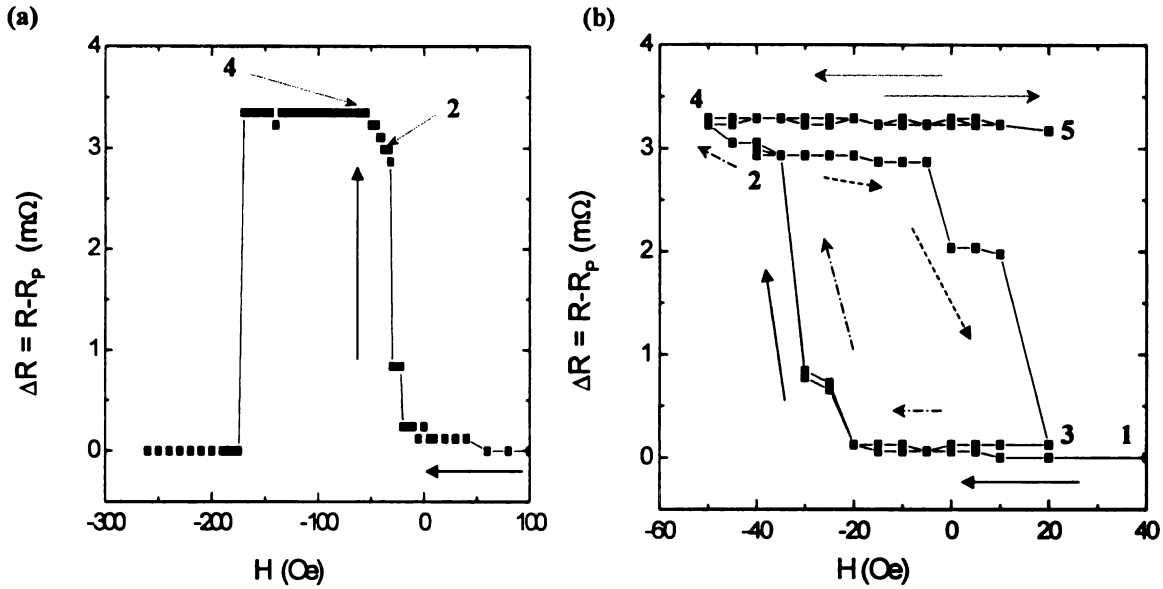

Fig. 3.9. ΔR (= R – R_P) vs. magnetic field, H. Head-to-head wall motion in a U-shaped notch of a Au top contact sample at 295 K. a) Overall major field sweep. b) Detail of minor field sweep. Sample 1470-3B-c at 295 K, Nb top contact.

Fig. 3.10 exhibits wall motion in a NC notch of a Au top contact sample at 295 K. After achieving the P state at –500 Oe, the field is swept back to various values to: get the wall trapped in the thin Py layer, Fig. 3.10 (a); attain the AP state, Fig. 3.10 (b); and get the wall trapped in the thicker Py, Fig. 3.10 (c). Fig. 3.10 (a) shows totally reproducible cycles of ΔR vs. the sweeping field between 0 Oe and 40 Oe. The wall moves back and forth inside the constriction following the same path. In Fig. 3.10 (b), ΔR depicts stability of the AP state for 0 Oe ≤ H ≤ 180 Oe after the wall left the constriction. Fig. 3.10(c) indicates that the wall in the thicker Py layer is trapped in the constriction for H sweeps between 50Oe and 180 Oe; and even when H is reduced to 0 Oe after the sweeps, the wall remains trapped inside the notch.

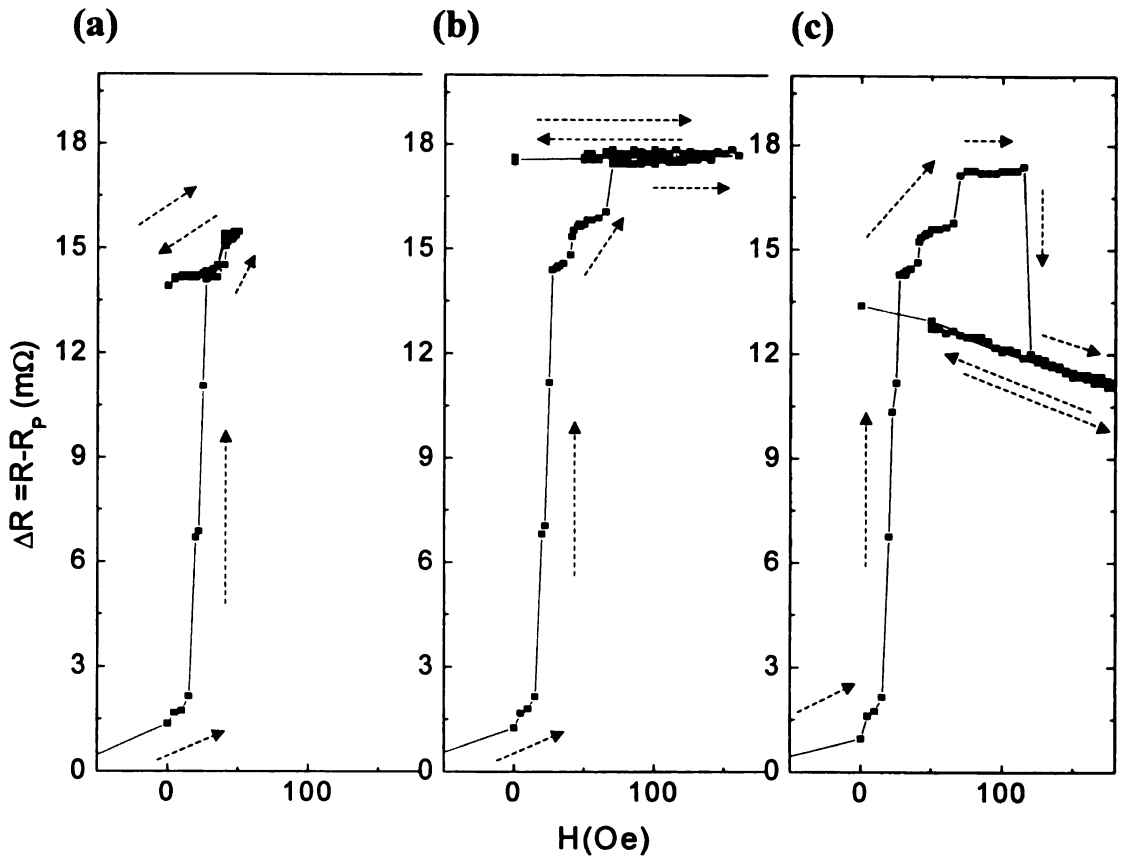

Fig. 3.10. ΔR (= R-R_p) vs. H, a head-to-head wall motion in a NC-shaped notch of a Au top contact sample at 295 K. a) Reproducible cycles of ΔR vs. H between 0 Oe and 40 Oe occurs, after wall-trapping. The wall moves back and forth inside the constriction following the same path. b) ΔR depicts stability of the AP state, once the wall has left the notch. c) A wall in the thicker Py layer is trapped in the constriction, and even when H is reduced to 0 Oe, the wall has not left the notch. Sample 1470-1A-a.

In Fig. 3.11 we see the response of a wall trapped in the thin Py layer to field variations for a U-shaped-notch sample with Nb top contact at 4.2 K. After setting H = -500 Oe (P state), a wall moves in the notch region for 10 Oe ≤ H ≤ 150 Oe. At 150 Oe the wall is very close to leaving the notch. Sweeping the field back and forth between 150 Oe and 0 Oe reproducibly shifts the wall between the same two pinning sites within the constriction and with hysteretic motion. These observations suggest that the constriction is elongated and rough having at least two pinning sites between which the wall can

move with hysteresis. In contrast, in Fig 3.10 (a), the motion of a wall between the two pinning sites does not exhibit hysteresis, which is probably due to the higher thermal activation at 295K .

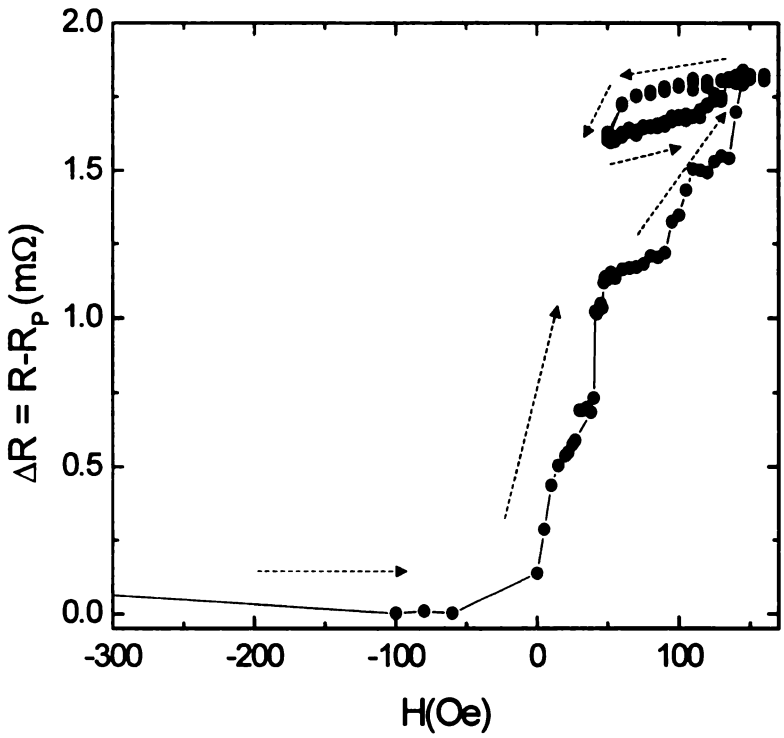

Fig. 3.11. ΔR (= R – R_P) vs. magnetic field, H. Sweeping H back and forth between 150 Oe and 0 Oe shifts the wall between the same two points within the notch. Back and forward motions follow different paths. Sample 1470-5B-a at 4.2 K, U-shaped notch and Nb top contact.

These observations along with those of other samples imply that, in general, when any system "with a trapped wall" is relaxed by changing H to 0 Oe, the wall continues in the notch region. Without the wall irreversibly leaving the constriction, it can move to a different point in the notch which gives a lower energy state.

3.8 Time Studies

Figs. 3.12 and 3.13 show the time dependence of R after the field sweep was stopped at the values of H indicated in Fig. 3.12 (a) as A-C and in Fig. 3.13 (a) as A-F. Letter A indicates the first value at which a positive field sweep was interrupted, and then R was monitored for long periods of time to assess the stability of wall trapping. Next the field sweep was started again at −500 Oe (or 500 Oe) and stopped at another value of H, points B-C in Fig. 3.12 and points B-F in Fig. 3.13.

In Fig 3.12 the stability of the trapped wall in a V notch of both Py layers was of interest. In Fig. 3.12 (b) curves A-C clearly show no change of $\Delta R(= R - R_P)$ in time. This means that the wall does not move out of its original pinning site when H is fixed. This system is very stable, as expected.

In Fig. 3.13 (a) we see the overall curve of a U notch sample; but after repeated field sweeps from −500 Oe to +500 Oe, ΔR became more stable. The open circles represent one of these more stable sweeps that happens to exhibit wall trapping in the thick Py layer. In Fig. 3.13 (b) curves A-F exhibit significant changes in R with time, this implies that the wall is unstable moving or jumping between weak pinning sites inside the U-shaped notch. These changes are significantly larger than the electronics drifts of ≤ 0.02 mΩ.

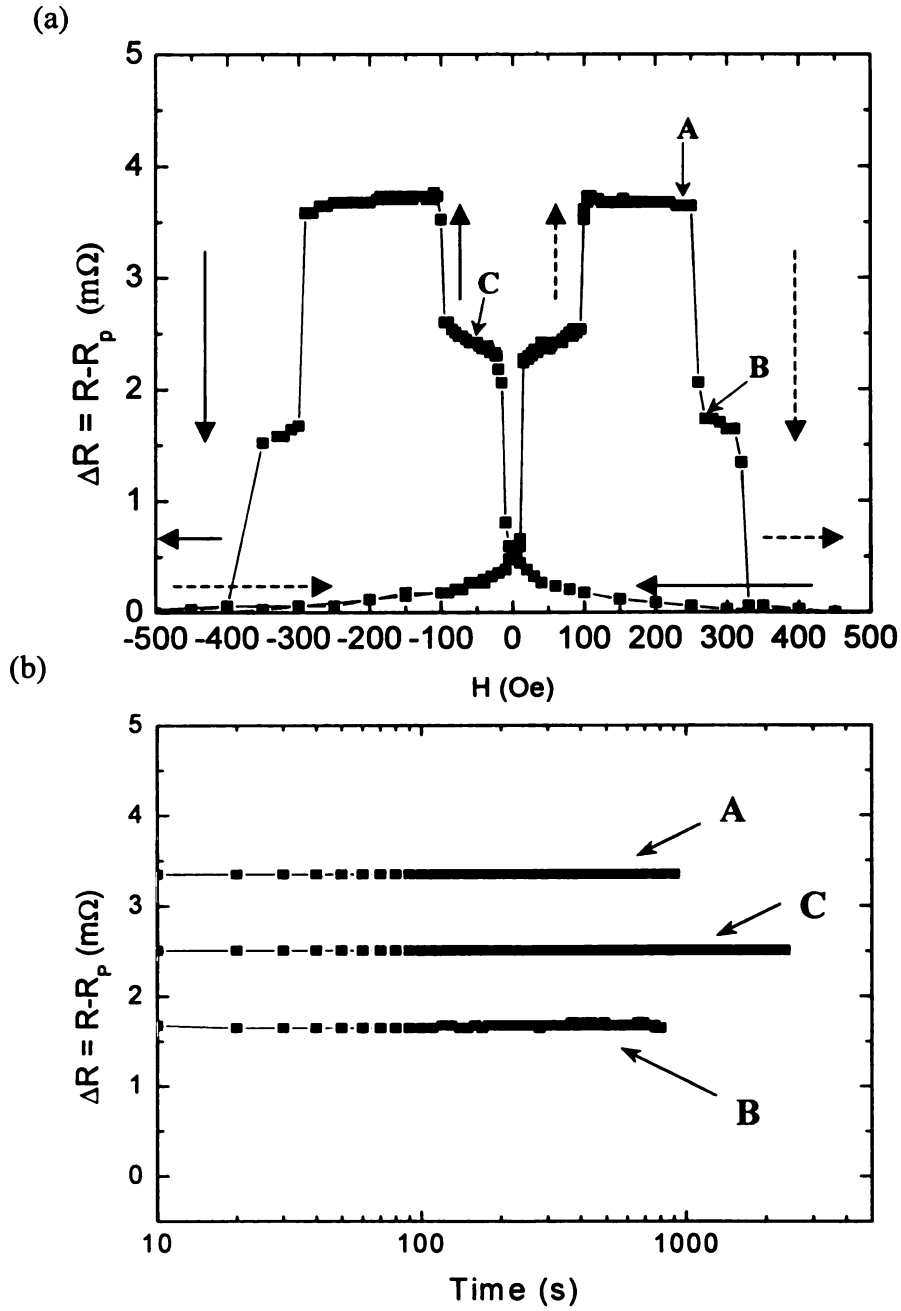

Fig. 3.12. a) $\Delta R(= R - R_P)$ vs. magnetic field, H, at 4.2 K for a sample with a V-shaped notch. H sweeps start at –500 Oe and then stopped for about 1000 s at a given H represented by A and B. Then the field sweep is started again at 500 Oe and then stopped for about 1000 s at a given H represented by C. b) Resistance, R, vs. time, commencing 10 s after magnetic field sweep is stopped at A-C. Sample 1470-6B-a, Nb top contact.

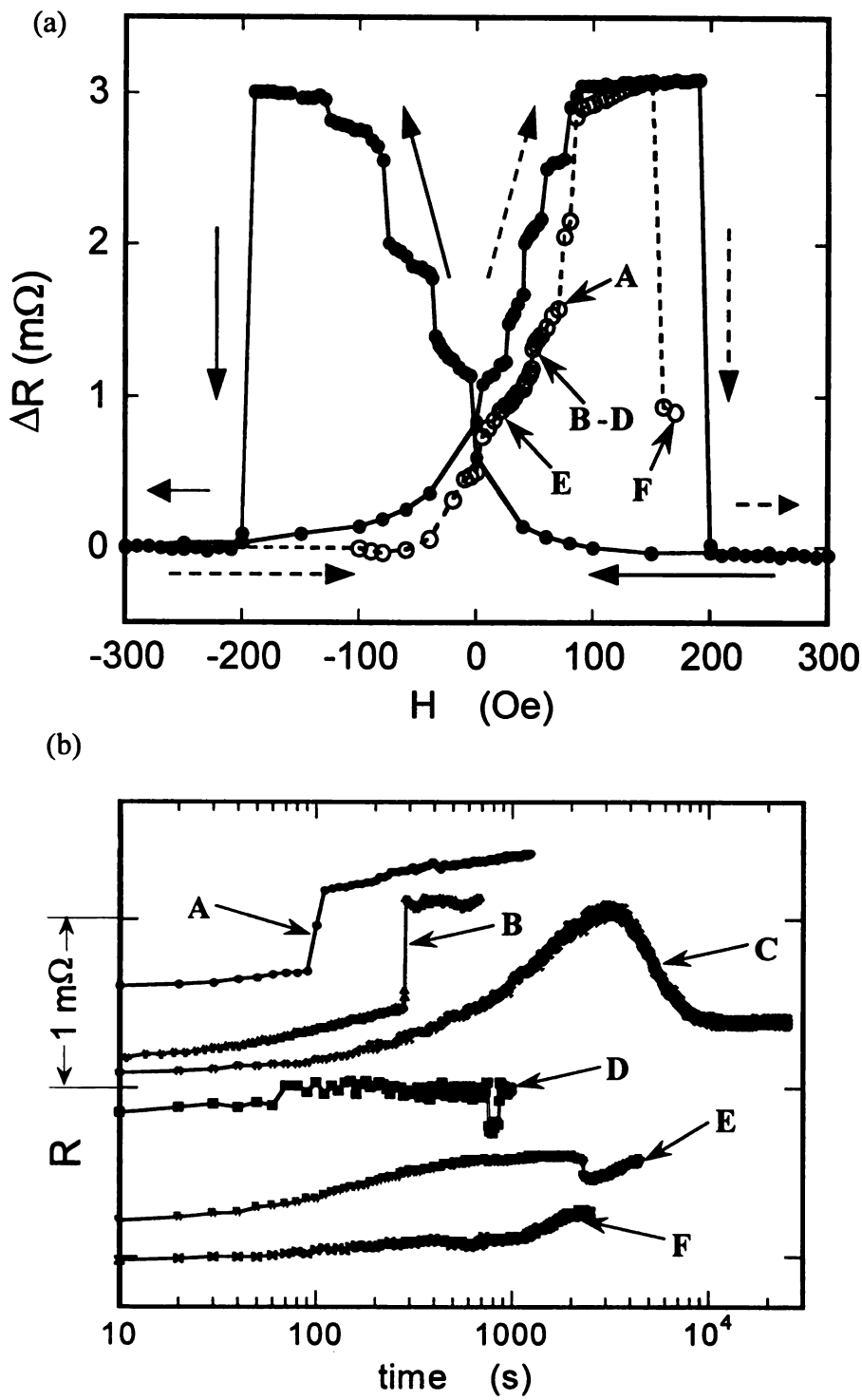

Fig. 3.13. a) ΔR (= $R - R_P$) vs. H, at 4.2 K for a sample with a U-shaped notch. Open circles: H sweeps start at –500 Oe and then stop for over 1000 s at a given H represented by A–F. Then the field sweep is started again at –500 Oe. b) ΔR vs. time, commencing 10 s after magnetic field sweep is stopped. A–F correspond to values of H shown in (a). The ordinate values of these curves have been shifted somewhat for clarity, but they share the same incremental resistance scale. Sample 1470-1B-a, Au top contact.

These domain wall motions inside the U notch are somewhat similar to what was observed by Giordano *et al.*[6-7], who proposed that domain wall depinning in very narrow Ni nanowires (with no constriction) occurs by thermal activation over a barrier above 2 K, as opposed to tunneling through a barrier. This idea is also sustained by a theoretical study of quantum domain wall depinning of by Chudnovsky *et al.*[10], who established that for a ferromagnetic layer with uniaxial anisotropy the crossover temperature between thermal activation and quantum tunneling regimens is typically 0.1-1 K. Due to the geometrical similarities of these works and our system, we presume that at 4.2 K when H is fixed and a wall moves between pinning sites of a notch, as shown in Fig. 3.13 (b), thermal activation takes placed over time scales > 80 s. However, during a rapid field sweep and 3-sec R measurement, the time scale to thermally activate a wall to escape from a particular pinning site must be within ~ 3s. As H increases, the potential barrier lowers until this thermally-activated escape can occur. Thus, the change in H associated with each trapping step is a measure of the original barrier height just after the wall got trapped at that step.

3.9 Current Driven Studies

As mentioned earlier, many of the recent domain wall trapping studies emphasized the use of high "in plane" current densities to manipulate the wall motion in narrow structures. [3-5] Analogously, we are interested in knowing if, by applying a CPP density current, we would be able to control, or at least perturb, the position of a wall.

Fig. 3.14 (a) shows an example of R vs. H data for a U-shaped-notch sample at 4.2 K. After starting in the P state at H = -500 Oe, the sweeping field is gradually increased to ~125 Oe, point A, where the wall in the thinner Py layer is trapped in the constriction. H is then set to 0 Oe, the system relaxes but the wall remains trapped, as seen in Sec 3.7. The resistance is then monitored for progressive DC current increments, in cycles between 0 mA → 4 mA → -4 mA → 0 mA. This CPP DC current is added to the AC current used to read sample resistances. The resistance drop seen in Fig 3.14 (b) (circular red symbols) indicates that the wall has shifted from position A to position B, which is another pinning point within the notch.

Note that the DC current scale in Fig. 3.14 (b) does not display high values of current. This is because R shows drastic changes when the DC current in the Nb contact exceeds the critical superconducting current density, see Appendix. Only the states before and after the DC-current application are of interest.

In Fig. 3.14 (a), the system is similarly carried from the P state at H =- 500 Oe to H~ 50 Oe, point B, which is also in the trapping region of the wall in the thinner Py layer. H is set to zero and R is then measured following the same DC cycles described above, but no motion of the wall is observed, see square black symbols in Fig. 3.14 (b). This is an indication that point B is a lower-energy pinning site, since the wall relocates from another place in the notch to this point but once it is there it does not move.

Point C in Fig. 3.14 (a) corresponds to trapping of the wall in the constriction of the thicker Py layer. This second step did not occur in the particular overall run of Fig. 3.14 (a). The system is taken through the P and AP states to trap the wall at H ~ 200 Oe,

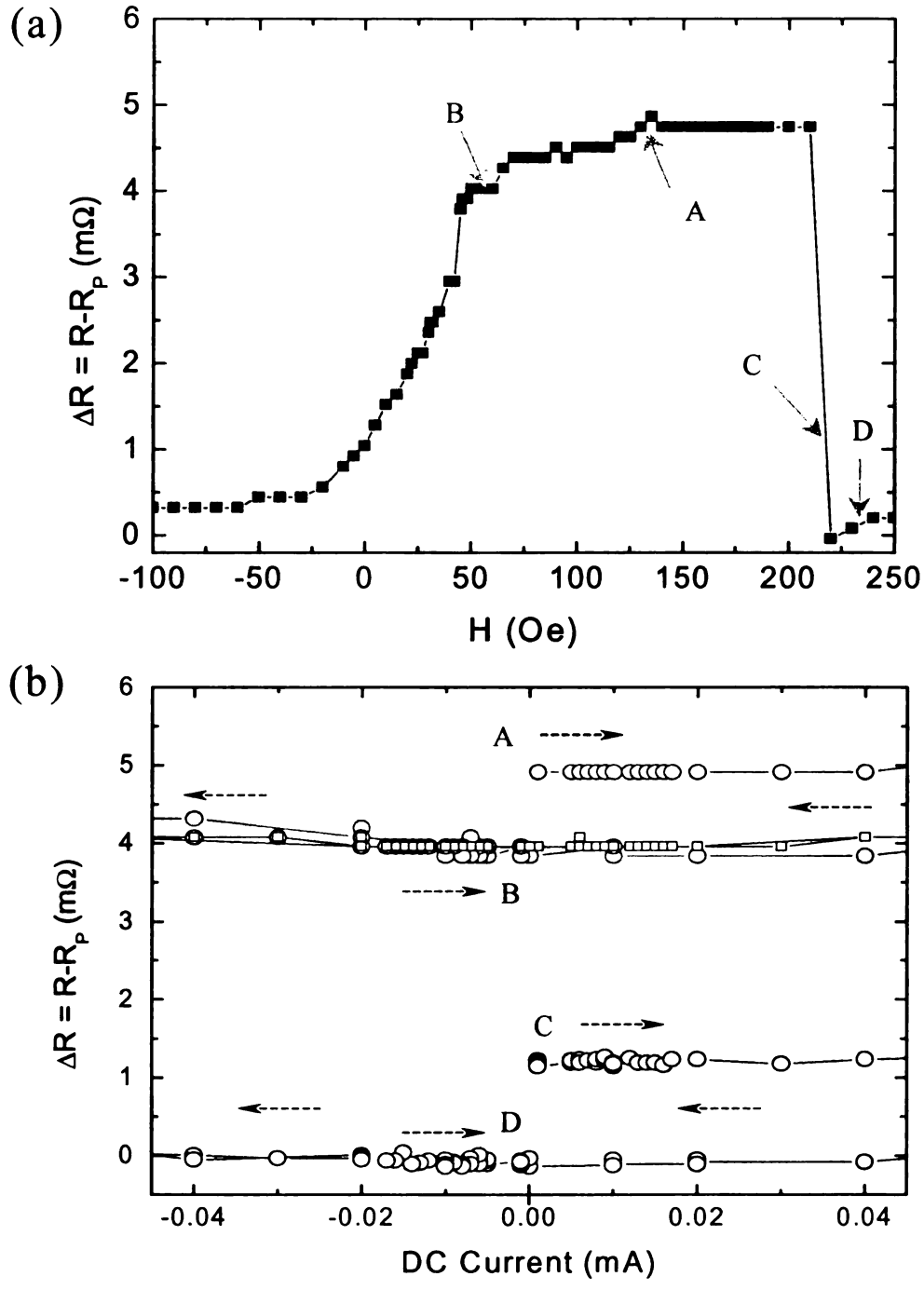

Fig. 3.14. Wall motion by applying a CPP DC current density of 3 x 10^{10} A/m^2. a) $\Delta R(= R - R_P)$ vs. magnetic field, H. H sweeps start at –500 Oe, stop at a given H represented by A and C, and finally go to 0 Oe. A and C indicate wall trapping in the thinner and thicker Py layers, respectively. B represents relocation of wall trapped in the notch of thinner Py layer. D represents P state after the wall has left the notch in the thicker Py layer. b) ΔR vs. DC current. Sample1492-1A-b at 4.2 K, Nb top contact and U-shaped notch.

and then H is set to 0. R is measured while a DC current is applied as explained before. R, in Fig 3.14 (b), shows that the wall moves off the constriction to point D, P state.

These preliminary DC-current investigations showed that only 2 out of 5 U-shaped-notch samples studied in this way exhibited indications of a wall being driven by a DC current. In Figs. 3.14 there is no indication of preferred wall motion direction (along x) other than to lower energy points.

The mechanisms of wall motion due to a CPP DC current density is not yet understood. The maximum applied DC current density, ~ 3 x 10^{10} A/m^2, is an order of magnitude lower than the characteristic spin torque mechanism current densities, ~10^{11} A/m^2 [11]. This suggests that perhaps other mechanisms are responsible for this wall motion. For example, if one were to consider the field generated by the DC current as a possible cause, one must know the actual non uniform current density distribution. Remember that the critical current of the top Nb contact was exceeded in these studies, which additionally complicates the analysis. In spite of this, for an "initial" analysis, simple numerical calculations, for a uniform current flow through the contacts and the sample, indicate that this field is non-uniform and could be locally important, ~ 25 Oe. However, further studies must be done to understand better CPP-current-driven wall motion.

REFERENCES

[1] T. Ono, H. Miyajima, K.Shigeto and T. Shinjo. *Appl. Phy. Lett.* **72**, 1116 (1998).

[2] T. Ono, Y. Ooka, S. Kasai, H. Miyajima, N, Nakatani, N. Hayashi, K. Shigeto, K. Mibu and T. Shinjo, *Mater. Sci. Eng. B* **84**, 126 (2001).

[3] M. Kläui, C. A. F. Vaz, J. A. C. Bland, W. Wernsdorfer, G. Faini, E. Cambril and L. J. Heyderman, *Appl. Phys. Lett.* **83**, 105 (2003).

[4] M. Tsoi, R. E. Fontana and S. S. P. Parkin, *Appl. Phys. Lett.* **83**, 2617 (2003).

[5] J. Grollier, P. Boulenc, V. Cros, A. Hamzić, A. Vaurès, A Fert and G. Faini, Appl. *Phys. Lett.* **83**, 509 (2003).

[6] N. Giordano and J. D. Monnier, *Physica B* **194-196**, 1009 (1994).

[7] K. Hong and N. Giordano, J. *Magn. Magn. Mater.* **151**, 396 (1995).

[8] J.Z. Sun, L. Chen Y. Suzuki, S.S. Parkin, R. H. Koch, *J .Magn. Magn. Mater.* **247**, L237-L241 (2002) and references therein.

[9] R.D. Mc Michael, J.Eicke, M.J. Donahue, and D.G. Porter, *J. Appl. Phys.* **87**, 7058 (2000).

[10] E. M . Chudnovsky, O. Iglesias, P. C. E. Stamp, *Phys. Rev. B* **46**, 5392 (1992).

[11] Katine J.A., Albert F.J., Buhrman R.A., Myers EB, Ralph D.C., *Phys. Rev. Lett.* **84**, 3149-3152 (2000).

CHAPTER 4

Summary and Conclusions

We have successfully adapted the Ono *et al.* method for trapping domain walls[1-2] to current perpendicular to plane, CPP, giant magneto resistance, GMR, measurements. The multilayer sequence was Nb(100)/Cu(10)/Py(20)/Cu(10)/Py(5)/Cu(5)/Au(15), where Py = $Ni_{84}Fe_{16}$ and the thickness are in nm. We shaped the Py/Cu/Py/Au part of the multilayer into a long 500-nm-wide long wire with a U-shaped or V-shaped constriction near its middle, acting as a wall-trapping site. A sweeping magnetic field, H, was applied along + x and parallel, P, to the axis of the wire. After saturation, this H direction was inverted (along –x), and magnetization reversal started by nucleation of a magnetic (head-to-head) domain wall in the thinner Py layer at low values of H while the magnetization of the thicker Py layer remained fixed. Closure domains initially nucleated the wall in a diamond-shaped reservoir placed at the +x end of the nanowire, and then the wall was injected in the –x direction from there into the thinner Py layer of the nanowire. At this very low field, we could very-effectively observe wall trapping because the CPP current is confined to the notch region by a 900-nm-wide top contact made of 200-nm-thick Au or 150-nm-thick Nb. At 4.2 K, the latter provided a more uniform CPP current density because the bottom and top Nb layers became superconductors, but measurements at 295K have also been successful with non-uniform CPP currents. The notch geometry affected the wall motion, which we were able to detect by subtle GMR changes between P and antiparallel, AP, relative orientations of the magnetizations of the two Py layers. The response of a trapped

wall to H in the thinner Py layer produced an approximate linear variation of R in each trapping step. This was consequence of the enhanced sensitivity for domain wall motions given by CPP GMR, which cannot be obtained by using the current-in-plane technique of Ono *et al.* Resistance changes with H showed that in V-notches one trapping site occurred. In contrast, for U-notches several pinning sites were seen while the wall remained trapped in the constriction. This behavior depended upon the wire edge roughness and other defects, which acted like similar-strength pinning sites where trapping of the wall could occur. Using the change in R associated with the position of the wall in the notch region, unknown constriction geometries could be characterized. The flexibility provided by this new method allows the CPP current region to be chosen independently of the long dimension of the wire. This helped us detect the presence of the wall even outside the notch region, right after the wall had escaped from the notch, and also verify that the subtle readjustments of the MR associated with coupling between the Py layers are clearly sensed in the constriction region only. This detection scheme allowed us to confirm the expected -x direction of the wall propagation after the wall was injected from the reservoir into the nanowire. As the magnetic field continued increasing along -x, a second wall in the thicker Py layer was injected from the reservoir into the nanowire, and it sometimes got trapped in the notch. Finally, if the magnetic field was raised further, the wall in the thicker Py layer escaped from the notch and the P state was attained. Successful pinning of a wall at the constriction in the thicker Py layer was less likely because this wall was injected at a higher field, meaning that the energy barrier for escape was already lower in the notch.

In all cases, when a system with wall trapped in its constriction was relaxed by sweeping the field to 0 Oe, the wall did not have to leave the constriction, but instead it

moved to a different point in the notch seeking a lower energy state. Many of these changes were reversible. In a stationary regime, when the magnetic field is kept fixed, the time dependence of the wall position within the constriction could be determined with high precision using our CPP GMR technique. We believe such wall motions at 4.2 K are driven by thermal activation.

We observed in some samples motion of domain wall driven by high-density CPP currents of ~ 3 x 10^{10} A/m^2. Since the current density is one order of magnitude less than the typical current density,~10^{11} A/m^2, reported for spin torque mechanism[3], the particular mechanisms of DW motion driven by a DC CPP current is not yet understood.

In conclusion, we have used localized CPP GMR to detect the occurrence and small motions of a trapped domain wall in a narrow ferromagnetic wire. This different wall-detection scheme that we developed provides enhanced sensitivity to small wall motions. It will also facilitate the study of a wide range of interesting wall-trapping geometries. For example, (1) we could investigate the motion of a magnetic vortex, in a disk-shaped thin ferromagnetic film of diameter < 1 μm, due to the application of an in-plane magnetic field. (2) We could examine wall motion in a major constriction with two trapping sites, producing a double potential well, that can be modified by changing H and / or exciting with a high-frequency H. This system would also allow us to inspect motion, between the two pinning sites, of a wall driven by high-density CPP current. (3) By lowering the temperature, we will be able to study quantum tunneling as a possible mechanism of wall motion at fixed H.

REFERENCES

[1] T. Ono, H. Miyajima, K.Shigeto and T. Shinjo, *Appl. Phy. Lett.* **72**, 1116 (1998).

[2] T. Ono, Y. Ooka, S. Kasai, H. Miyajima, N, Nakatani, N. Hayashi, K. Shigeto, K. Mibu and T. Shinjo, *Mater. Sci. Eng. B* **84**, 126 (2001).

[3] Katine J.A., Albert F.J., Buhrman R.A., Myers EB, Ralph D.C., *Phys. Rev. Lett.* **84**, 3149-3152 (2000).

APPENDIX

Uniformity of the CCP Current Density

The distribution of the current density is expected to differ considerably between Au and Nb top contacts samples. At 4.2 K the Nb top contact becomes a superconducting equipotential which produces a uniform current density. Since Au remains normal, the CPP current density will be non uniform. To understand this latter case, let us make use of a simple Ohmic model presented by Lenczowski et al.[1], who calculated a current distribution in a small pillar-like structure for CPP magnetoresistance experiments. Fig A.1 shows one of the square pillar geometries studied by Lenczowski that is similar to the geometry used in this work .

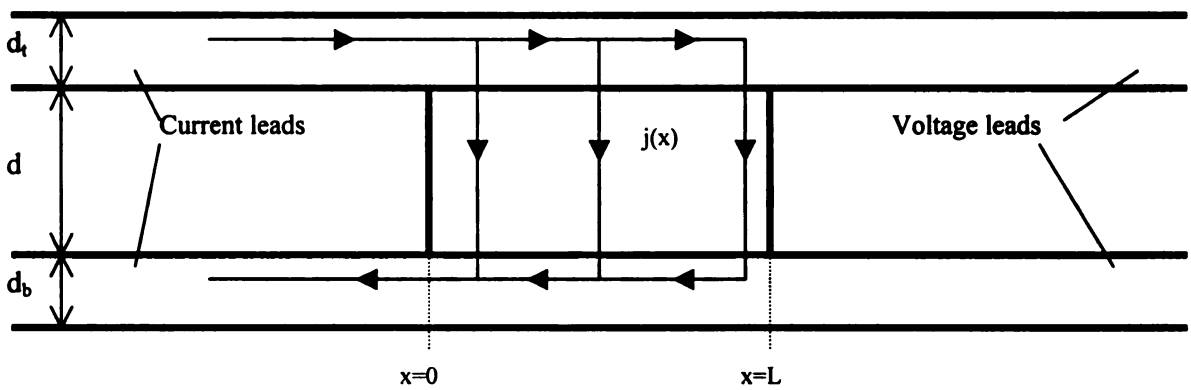

Fig A.1. Sketch of the current density in the nanopillar Ohmic model studied by Lenczowski.

This one-dimensional model assumes that in the current leads the current density decreases monotonically from a certain value at one of the edges of the pillar, x=0, to zero at the other edge, x=L, see Fig. A.1.

The current density in the pillar, j(x), is given by the following expression:

$$j(x) = \frac{1}{Lk}\frac{I}{\sinh(L/k)}\cosh\left(\frac{L-x}{k}\right) \qquad \text{(A. 1)}$$

where x represents position along the axis perpendicular to the current in the pillar, and L is the width of the square pillar. k is defined as:

$$k = C^{1/2}\left(\frac{\rho_t}{d_t} + \frac{\rho_b}{d_b}\right)^{-1/2} \qquad \text{(A. 2)}$$

$$C = \frac{1}{2}(\rho_t d_t + \rho_b d_b) + AR_{AP} \qquad \text{(A. 3)}$$

where ρ_t and ρ_b are the resistivities of the materials of the top and bottom contacts respectively, and d_t and d_b are the thicknesses of the top and bottom contacts. AR_{AP} is the specific resistance of the multilayer pillar in the antiparallel state of U-shaped notches of area 1.5 x 10^{-13} m^2. AR_{AP} were calculated following the 2CSR model at 4.2 K, Au-AR_{AP} ~11.2 fΩm^2 and Nb-AR_{AP} ~11.6 fΩm^2, see Table 1.2, and estimated from the experimental data at 295 K, Au-AR_{AP} ~76 fΩm^2 and Nb-AR_{AP} ~105 fΩm^2, see Table 3.2. The following contact resistivities were used: at 4.2 K ρ_{Nb} = 0 $\mu\Omega$m and ρ_{Au}= 0.02 $\mu\Omega$m, and at 295 K, ρ_{Nb} = 0.145 $\mu\Omega$m and ρ_{Au}= 0.04 $\mu\Omega m$.[2] L was taken to be equal to 0.1 μm, in the center of the notch, and 0.5 μm in both ends of the CPP current flow, where the width of the notch is a maximum and the worst-case scenario for the current density distribution.

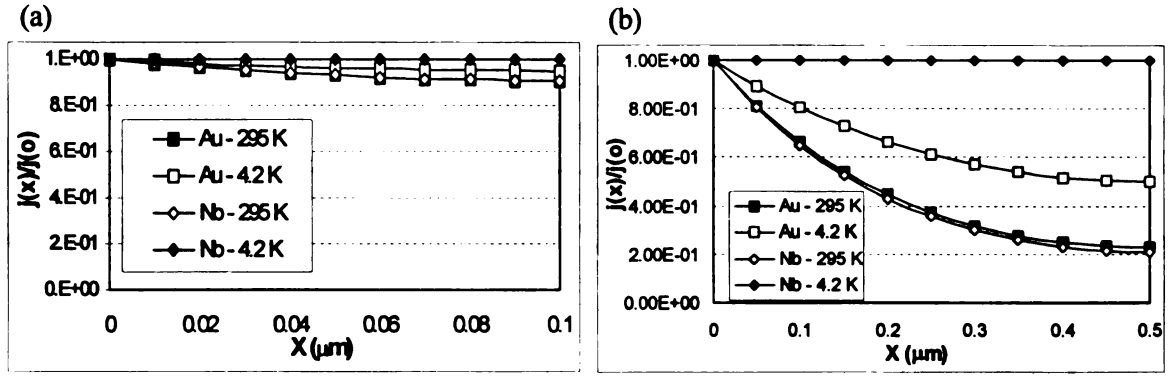

Fig A.2. Simulation of the current density through a multilayer pillar using Lenczowski and *et al.* method.[1] a) L was taken to be equal to notch width at the center ~ 0.1 μm. b) L was taken to be equal to 0.5 μm, the maximum width of the notch area, which is the worst-case scenario.

Fig. A.2 shows, as expected, that at 4.2 K, the Nb-top contact produces totally uniform distribution of the current. On the contrary, for Au-top contacts at 4.2 K the change in current-density is ~ 50 % at the at both extremes of the CPP current flow see Fig. A.2 (b). However, it is ~ 5 % in the center of the constriction, see Fig. A.2 (a). Thus, the "average change" of the current-density distribution over the whole notch is ~ 27 %. This suggests that R is rather-uniformly sensed over the entire CPP current flow region and therefore the data obtained with Au-top contacts can be considered reliable at 4.2 K. At 295K, Nb contact current-density changes are ~ 80 % at the ends of the constrictions, see Fig. A.2 (b), and ~ 10 % in the center of the constriction, see Fig. A.2 (a). Thus, the "average change" in the current-distribution over the whole notch is ~ 45%. Comparable behavior is observed for the Au-top-contact current-distribution at 295 K. We should expect the least-uniform current-density for the any contact to occur at 295. However the observed non uniformities in the average current-density-distributions are not "drastic enough" to lead one to conclude that R is not representative of the whole constriction and that these contacts are unreliable.

Even though Nb is the best material for the top contacts at 4.2 K, we need to be aware that there are limits to the current density that the superconducting contacts can support while maintaining an equipotential. If this critical current density is exceeded, causing these contacts to become "normal", the CPP current density will become non uniform as shown in Fig. A.2. The critical in-plane current of our "dirty" Nb top strip was measured to be ~ 1.6 mA at 4.2 K, for the Nb sputtered in the ion-milling chamber. For a superconductor the current flows close to the surface in a region approximately equal to penetration depth, λ. At 4.2 K, λ is ~100 nm,[3] for our Nb. Since the thickness of the Nb strips is ~ 150 nm, the in-plane current will be close to uniform over the cross-section of the strip. This gives a critical current density of ~ 1.2×10^{6} A/cm^2 for our Nb strips, a reasonable value for our sputtered Nb.

REFERENCES

[1] S.K.J.Lenczowski, R. J. M. van de Veerdonk, M.A.M., J. B. Giesbers , and H.H. J. M. Janssen, *J. Appl. Phys.* **75,** 5154 (1994).

[2] Kittel, *Introduction to Solid State Physics, 7th Ed.*, and personal communication.

[3] T. P. Orlando and K. A. Delin, *Foundation of Applied Supeconductivity*, Addison-Wesley, **6**, 259 (1991).